Characterization of the Valve Extracellular Matrix in Relation to Risk Factors for Calcific Aortic Valve Disease

By

Heather Nicole Hutson

A dissertation submitted in partial fulfillment of

the requirements for the degree of

Doctor of Philosophy

(Biomedical Engineering)

at the

UNIVERSITY OF WISCONSIN-MADISON

2018

Date of final oral examination: 07/23/2018

The dissertation is approved by the following members of the Final Oral Committee:
Kristyn S. Masters, Professor, Biomedical Engineering
Paul Campagnola, Professor, Biomedical Engineering
Kevin W. Eliceiri, Senior Scientist, Molecular Biology
Amish Raval, Associate Professor, Medicine
Rozalyn M. Anderson, Associate Professor, Medicine

ABSTRACT

Extracellular matrix (ECM) disarray is a hallmark of calcific aortic valve disease (CAVD). However, the relationship between aortic valve ECM dysfunction and several CAVD risk factors is not fully understood. This thesis aims to investigate the role of aging and sex, two major risk factors for CAVD, in disease-related dysfunction of the valve ECM. CAVD-related alterations in the microarchitecture of collagen, a major component of the valve ECM, were examined utilizing second harmonic generation microscopy (SHG) on human valve specimens. While many studies have focused on general ECM alterations in CAVD, microarchitectural changes have not previously been characterized, but have the potential to influence the phenotype of cells that inhabit the valve. Our investigations revealed an increase in collagen fiber width during CAVD, along with an increase in expression of the collagen crosslinking enzyme lysyl-oxidase (LOX) in the fibrosa, a collagen-rich layer of the valve. Investigation into age-related changes in the collagen fiber microarchitecture of the valve revealed a decrease in collagen fiber width and an increase in fiber alignment in the fibrosa with increasing age in the absence of changes in collagen content. These changes in collagen microarchitecture were also independent of changes in expression of LOX, indicating a distinction between the aging valve and disease pathology. In addition, analysis of the content of proteoglycans and glycosaminoglycans in the valve illustrated no alteration with aging of the valve. Sex-related differences in CAVD pathology were investigated at the cellular level using an *in vitro* model consisting of sex-separated porcine valve interstitial cells (VICs) treated with varying doses of the pro-fibrotic stimulus, transforming growth factor-beta 1

(TGF-β1). These studies revealed a sex-dependent response to TGF-β1, with males demonstrating markers of phenotypic changes including increased ECM deposition, proliferation, and expression of *ACTA2* at lower doses of TGF-β1 compared to females. These findings support previous studies indicating males are at higher risk for CAVD and suggest that future studies into CAVD pathology should account for sex-differences. The results presented here also provide the basis for the creation of future *in vitro* models of the valve that mimic the native collagen microarchitecture to investigate the influence of the ECM structure on VICs.

ACKNOWLEDGEMENTS

With grateful appreciation, I wish to express my gratitude for the contributions and support of all the persons and groups that have enabled me to reach this goal in my academic and life journey. I could not have reached this achievement without the tireless assistance of each and every one of you.

Foremost, I am deeply grateful for the motivation and patience of my Ph.D, advisor, Professor Kristyn Masters. Your mentoring and patience has been invaluable on this journey. Thank you to all my committee members Dr. Kevin Eliceiri, Professor Paul Campagnola, Amish Raval, and Rozalyn Anderson. Your encouragement, time, and expertise was instrumental in the completion of this work. I would particularly like to thank the collaboration with Professor Campagnola and his lab along with Dr. Eliceiri, and the Laboratory for Optical and Computational Instrumentation without which much of the work presented here would not have been possible. I wish to acknowledge and thank all the Master lab members, from undergraduates to post-docs that have assisted and encouraged though out my time here. I cannot thank my family enough for their love and support. They are forever my sounding board and kept motivated. They have believed in me and my dreams and have always been there for me.

I also want to acknowledge the financial support I have received from the Nation Science Foundation, the Cardiovascular Research Center, and the National Institute of Health (T32 HL007936, R01 HL093281, R21 EB019508) without whose support I could not have completed this this thesis.

For My Mom

TABLE OF CONTENTS

LIST OF FIGURES

LIST OF TABLES

CHAPTER 1: INTRODUCTION

Calcific aortic valve disease (CAVD) is a highly prevalent valve disease characterized by thickening of the aortic heart valve in early stages (sclerosis) and valve stiffening and calcification in later stages (stenosis) [9]. Aortic valve stenosis, which affects a quarter of the individuals in the US over the age of 65, is associated with a 50% increase in the risk of other potentially fatal cardiovascular events within 5 years of diagnosis [10-12]. While the late stage of CAVD (severe stenosis) has been well characterized, further exploration is needed to fully understand the molecular and cellular processes that occur during disease initiation and development [13-15]. Similarly, the connection between major risk factors and underlying mechanisms for CAVD has not been fully identified [9, 11, 16]. Our limited knowledge of CAVD progression and the contribution of risk factors to disease pathology has resulted in a limited number of available treatments for CAVD.

The work in this thesis aims to characterize changes in the extracellular matrix, namely the collagen structure, that occur at late stages of CAVD and with age to provide more detail into microarchitectural changes of the ECM that occur as a result of disease and risk factors associated with CAVD. To help further our understanding of CAVD initiation and development, the work in this thesis also aims to investigate the role of two major risk factors for CAVD, aging and male sex, in disease-related alterations in the valve extracellular matrix (ECM).

1.1 The Aortic Valve

The aortic heart valve is one of four valves in the human heart (Figure 1.1A-B). Unlike the mitral and tricuspid valves, which regulate the flow of blood through different chambers in the heart, or the pulmonary valve, which controls the flow of blood to the lungs, the aortic valve is responsible for regulating the flow of blood from the heart throughout the entire body (Figure 1.1B) [17]. During each of the 40 million cardiac cycles experienced by the heart during an average year, the aortic valve opens and closes to allow oxygenated blood from the left ventricle to flow through the aorta to tissues throughout the body [18]. The opening and closing of the aortic valve is determined by a pressure changes created by contracting and relaxing of the left

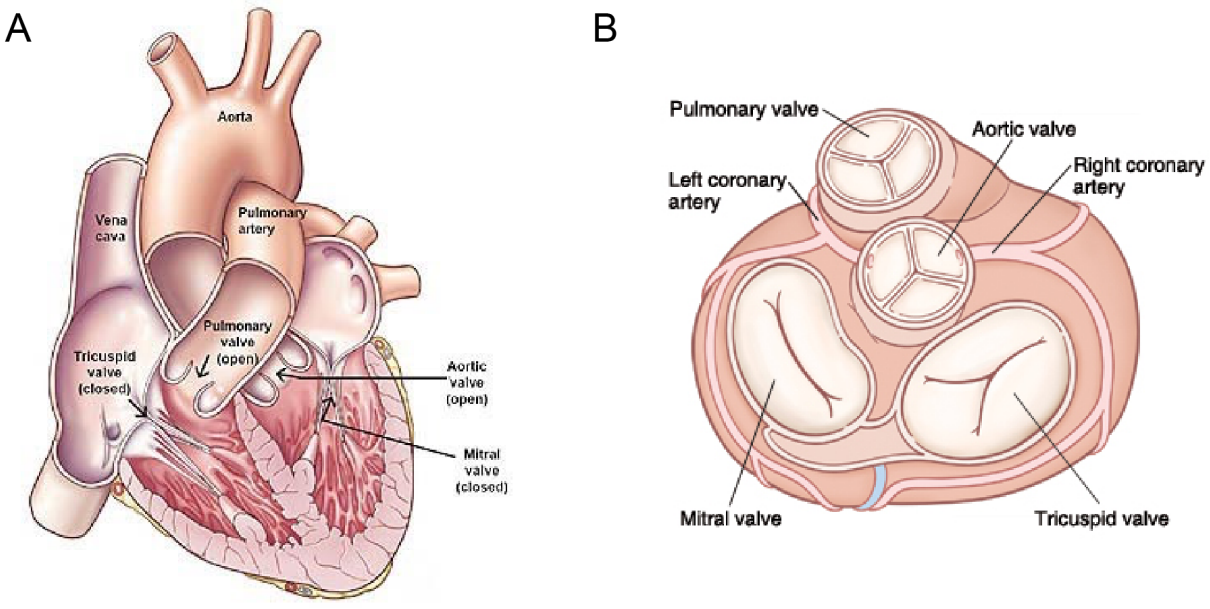

Figure 1.1 Anatomy of the heart. (A) Cross-section of heart (side view). [adapted from https://my.clevelandclinic.org/health/diseases/17600-valve-disease-types] (B) Heart valves (top view) [adapted from https://www.pinnaclehealth.org/wellness-library/blog-and-staywell/health-resources/article/20804]

ventricle. During systole (Figure 1.2A) the aortic valve opens in response to a pressure increase created by the contracting of the left ventricle, allowing blood to flow to the

aorta. Once this pressure begins to decrease leading to diastole, the aortic valve is able to completely close off the left ventricle from the aorta by coaptation of its three leaflets (Figure 1.2A) [19]. As the left ventricle must create enough pressure to move blood throughout the body, the aortic valve must withstand the largest pressure differential in the cardiovascular system during each of these cycles, causing it to experience severe shearing, flexion, and tension [15].

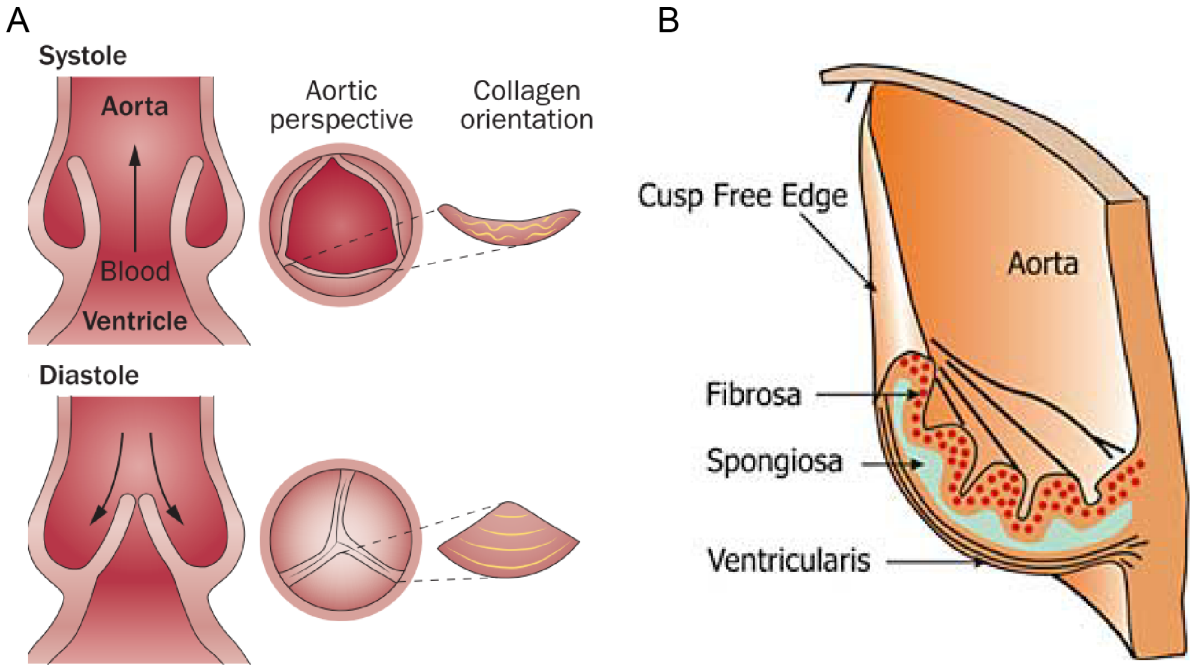

Figure 1.2 (A) Function of aortic valve during systole and diastole [adapted from Hutcheson et al. [1]] (B) Cross-section of aortic valve [adapted from Rock et al.[6]]

The aortic valve possesses the unique mechanical properties required to respond to these pressure changes due to the structure of each of its leaflets (Figure 1.2B) [15, 18]. The aortic valve is composed of three leaflets capable of closing off the left ventricle from the aorta, where each leaflet is a thin, intricate tissue comprised of a trilaminar

structure [7]. The trilaminar structure of the leaflet is comprised of the fibrosa (aorta-facing layer), the spongiosa (intermediate layer), and the ventricularis (ventricle-facing layer). The fibrosa is largely responsible for bearing the bulk of the mechanical stress experienced by the valve during diastole (Figure 1.2A). The ventricularis, on the other hand, is responsible for the elastic recoil of the leaflet during systole required to open the valve [15, 20]. The spongiosa, as the internal layer between the fibrosa and ventricularis, was previously hypothesized to play an important role in absorbing the compressive stresses that leaflets experience and enabling sliding between the fibrosa and ventricularis. However, recent investigation into the mechanics of the spongiosa suggests that it contributes to a dampening effect during valve deformation. This suggests that the spongiosa plays a minimal mechanical role in the valve [21-23].

The aortic valve is encased in a layer of valvular endothelial cells (VECs) which form a barrier between the extracellular matrix (ECM) components of the aortic valve and circulating blood [14]. A secondary population of cells called valvular interstitial cells (VICs) inhabit the three internal layers of the valve. VICs are involved in maintaining valve integrity and are thought to be the key cell population involved in valve dysfunction [14, 24].

1.2 Calcific Aortic Valve Disease Pathology

CAVD is a condition ranging from a mild thickening of the aortic valve leaflets (aortic valve sclerosis) to loss of function of the valve due to stiffening and calcification (aortic valve stenosis) (Figure 1.3) [9, 25]. Despite the high prevalence of this disease, the only treatments available are targeted at the late stages of the disease and include surgical aortic valve replacement (SAR) and transcatheter aortic valve replacement (TAVR) [1, 26].

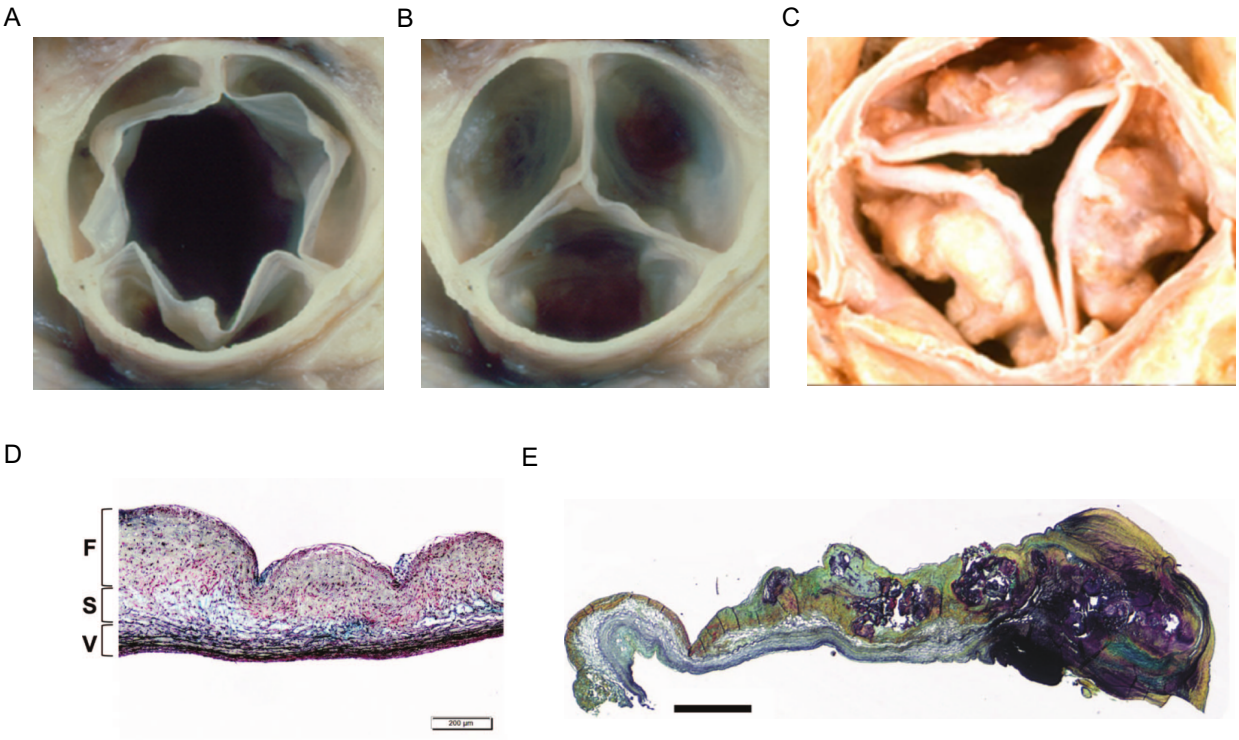

Figure 1.3 Calcific aortic valve disease. Healthy valve top view when open (A) and closed (B) Diseased valve (C) [adapted from Schoen FJ [3]] Cross section of healthy [adapted from Chen et al. [7] (D) and diseased (E) aortic valves stained with Movat's pentachrome [adapted from Stephens et al. [8]].

The limited availability of treatments is due in part to the fact that for many years this disease progression was originally attributed to a passive degenerative process resulting from the repetitive stresses endured by the valve [27]. However, current understanding of the ability of VICs to alter the valve ECM have shown that valve thickening and calcification is an active process [13, 15]. While this revelation concerning the progression of CAVD offers hope for new avenues of treatment, there is still much to discover about the initiation and progression of CAVD.

1.2.1 Valvular Interstitial Cells

Valve interstitial cells (VICs), a major cell type involved in regulation of the ECM, are a heterogeneous cell population with the ability to transdifferentiate into different phenotypes [28]. These cells reside in all three layers of the valve and work to maintain homeostasis of the valve through their ability to undergo phenotypic changes in response to various stimuli [29]. Healthy aortic valves are primarily populated by quiescent VICs (qVICs), which are characterized by the lack of cell markers associated with other VIC phenotypes [24]. While qVICs indicate a healthy valve, the full function of qVICs is not understood. In the event of injury to the aortic valve or changes in stress, qVICs can become stimulated to transdifferentiate into a secondary, myofibroblastic phenotype referred to as activated VICs (aVICs) [29]. In a healthy valve, aVICs typically account for only 1-5% of total VICs [28]. This low level is due to the elimination of aVICs through regulated apoptosis, or programmed cell death, following completion of valve repair or remodeling [28]. aVICs actively participate in the manipulation of their

surrounding ECM environment through production of extracellular matrix proteins such as collagen, laminin, and fibronectin along with expression of ECM degrading enzymes such as matrix metalloproteinases (MMPs). aVICs are also characterized by their increased expression of proteins such as alpha smooth muscle actin (αSMA), increased contractile potential, and increased proliferation, which are all necessary for effective response to valve injury and repair of the valve ECM.

While aVICs are necessary for proper maintenance of the valve, the transition of qVICs into aVICs occurs during CAVD progression without the apoptosis-driven removal of aVICs indicative of normal repair processes [24]. This results in an atypical level of aVICs (~30%) throughout the aortic valve [29, 30] with the ability to alter the ECM, leading to ECM disarray. Investigations have revealed the role of pathological stimuli such as lipids, lipoproteins, and pro-inflammatory factors in promoting VIC transdifferentiation [31, 32]. Infiltration of the valve by immune cells such as T-cells, macrophages, and monocytes has also been observed during CAVD [9]. Investigations into the role of several pro-inflammatory factors [33] have revealed increases in cytokines such as transforming growth factor-beta (TGF-β), tumor necrosis factor alpha (TNF-α), and interleukin-6, with CAVD [1, 9, 34]. TGF-β, which is reported to drive fibrosis in a variety of tissues [35], is present at increased levels in the stenotic aortic valve [36]. Investigations into the influence of TGF-β on VICs have revealed the ability of TGF-β to promote an aVIC phenotype (Figure 1.4) [37], resulting in increased contractility, deposition of ECM proteins, and expression of MMP2 and MMP9 [28]. As aVICs are involved in remodeling and repair of the valve ECM, an increase in TGF-β

such as that observed in diseased valves could suggest a mechanism by which disarray of the valve ECM occurs.

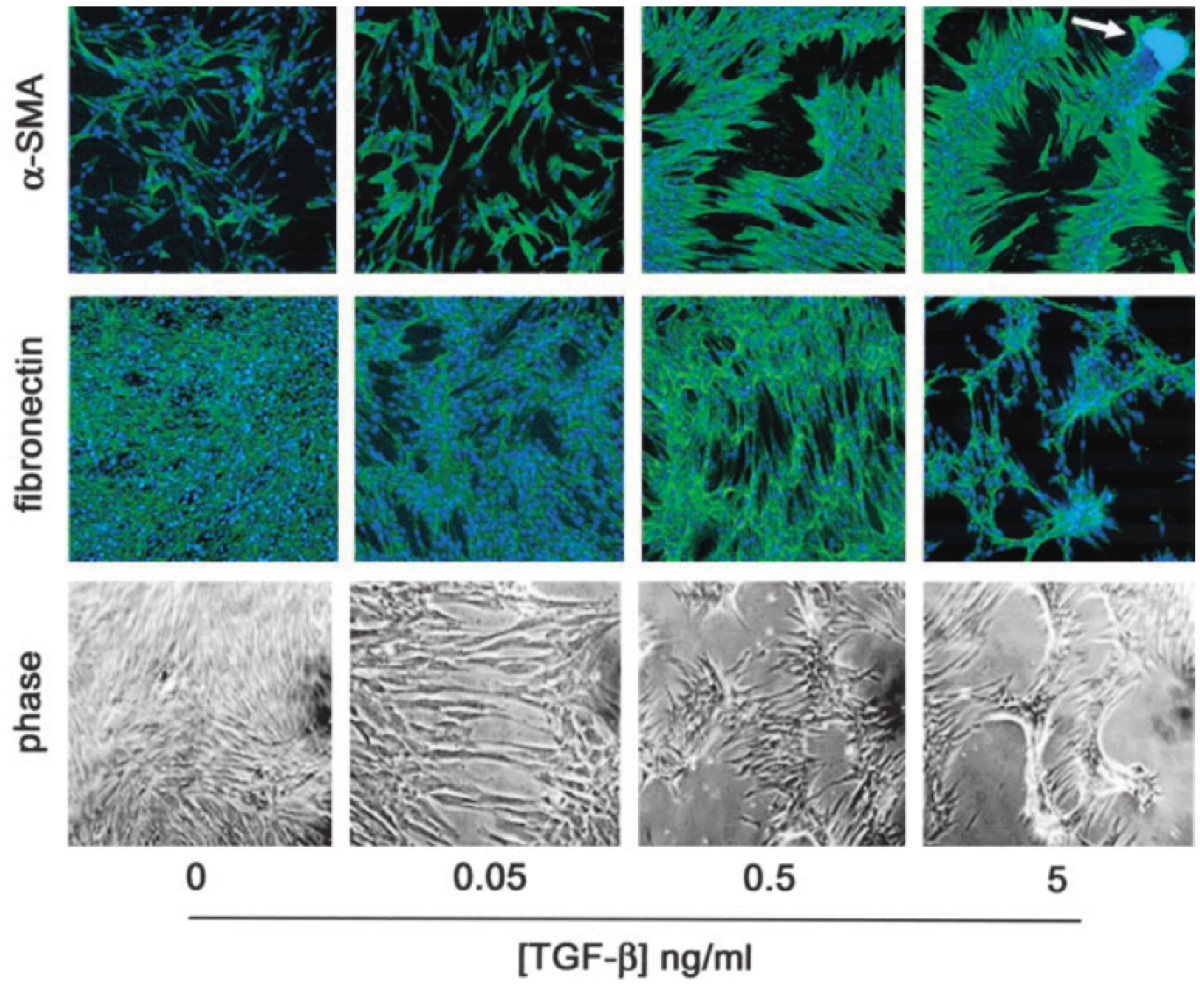

Figure 1.4 TGF-β increases activation of VICs [adapted from Walker et al. [5]]

During late stages of CAVD, an osteoblast-like VIC phenotype (obVICs) has been observed [38, 39]. This phenotype, like aVICs, is transdifferentiated from qVICs. However, unlike aVICs which can be observed during repair of healthy valves, obVICs are atypical for a healthy valve [14, 24]. obVICs are characterized by their ability to secrete alkaline phosphatase (ALP), osteopontin, osteocalcin, and other proteins active in mineralization processes. Due to their role in secretion of bone matrix proteins and related proteins, obVICs play a central role in the formation of calcific nodules that characterize the late stages of CAVD [24]. However, it is unclear what triggers this atypical behavior in VICs and what mechanisms may drive ECM changes that accumulate during CAVD.

1.2.2 The Extracellular Matrix

As previously described, the aortic valve leaflet exhibits a trilaminar structure comprised of the fibrosa, spongiosa, and ventricularis (Figure 1.3D, Figure 1.5A)). In a healthy aortic valve, each layer is identifiable by the distribution and orientation of the major ECM components collagen, glycosaminoglycans (GAGs), proteoglycans (PGs), and elastin [14]. The fibrosa, which faces the aorta, is composed mainly of fibrillar collagen (type I and III), oriented in a circumferential manner to allow for the crimping and uncrimping of fiber bundles during opening and closing of the valve (Figure 1.5B) [7, 40]. This collagen orientation is perpendicular to that found in the ventricularis, where the collagen is oriented radially along with fibers of elastin to support recoil of the valve [7, 17, 41].

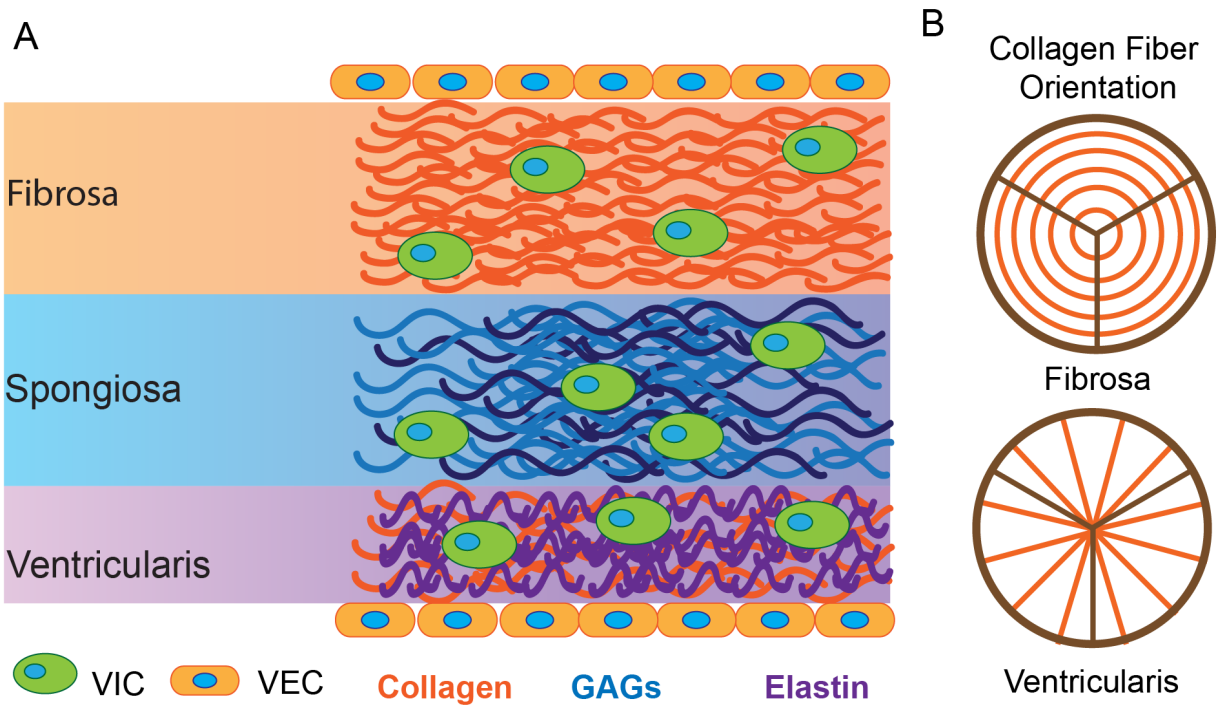

Figure 1.5 (A) Cross-section of the tri-layer structure (B) top-view of collagen fiber orientation

The inner-most layer of the valve leaflet is the spongiosa, which has very little fibrillar collagen despite lying between the collagen rich fibrosa and ventricularis. The bulk of the spongiosa is composed of GAGs (chains of repeating disaccharide units), and PGs [41, 42], which are glycosylated proteins formed by binding of GAGs to a core protein. While there are four groups of GAGs, hyaluronic acid (also known as hyaluronan, HA) and dermatan/chondroitin sulfate (CSGAGs) are the most common groups of GAGs represented in the valve [43-45]. Similarly, the most abundant PGs in the aortic valve are formed from CSGAGs and include biglycan, decorin, and versican. Decorin and biglycan are both part of the small leucine-rich proteoglycan family (SLRP), with biglycan being the most prevalent PG in the aortic valve [43, 44]. While the spongiosa

is necessary for the valve to function properly, it provides a minimal contribution to the mechanical role of the aortic valve [17, 22, 23, 41].

The trilaminar organization of collagen, elastin, and GAGs is necessary for the unique mechanical function of the aortic valve [17, 46]. During CAVD, this trilaminar structure becomes disrupted due to altered localization of ECM components, changes in ECM degradation, and altered synthesis of ECM components native to a healthy valve and atypically found in a healthy valve [46]. Specifically, changes in the ECM related to fibrosis and calcification processes are observed during CAVD [7]. Fibrosis is defined as an accumulation of fibrous ECM components such as fibronectin and collagen. Fibrosis is associated with tissue injury and as a result of inflammation [35]. In the aortic valve, fibrosis has been implicated as a precursor for the development of sclerosis. Calcification is indicated to be necessary for aortic valve stenosis [40] and can occur by dystrophic or ossific mechanisms. Dystrophic calcification is the result of fibrosis, which leads to aggregation and apoptosis of aVICs, followed by mineralization. Ossific calcification occurs due to calcium deposition and secretion of bone matrix proteins by obVICs [47]. in the localization of PGs and GAGs have been observed in diseased valves [7, 43, 48] with fibrosis and calcification. Specifically, PGs and GAGs have been observed localized to regions of calcific nodule formation (Figure 1.6).

However, while calcification, fibrosis, and the disarray of other ECM components have been reported in the diseased aortic valve, the connection between ECM changes and risk factors for developing aortic valve disease is not fully understood.

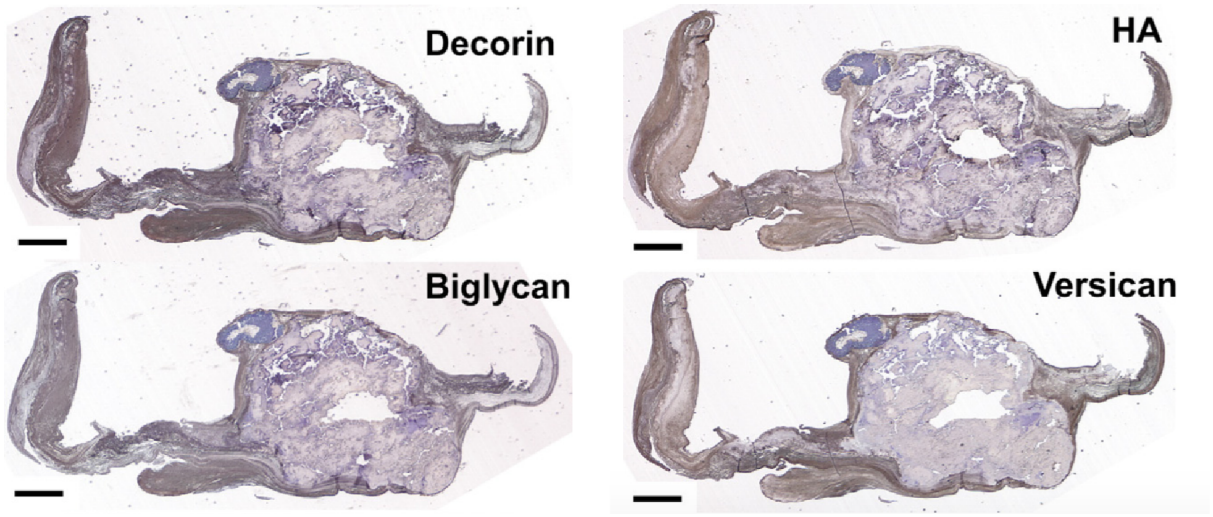

Figure 1.6 Expression of PGs and HA in diseased aortic valves. Positive expression of PGs and HA are indicated by brown staining. [adapted from Stephens et al [9]]

Many investigations have focused on the potential of pathological stimuli such as lipoproteins and TGF-β to promote VIC-driven changes in the ECM of the valve [49, 50]. However, increasing evidence suggests a co-stimulatory relationship between ECM components and circulating or secreted molecules and proteins in CAVD progression [7]. For example, recent studies have also shown that while increases in GAG content occurs in CAVD, it is not the increase in GAGs themselves that alter the VIC phenotypes [51]. Rather, these GAGs retain circulating pathological factors such as lipids and present them to VICs in a manner that drives phenotypic changes [31, 51]. Similarly, it has been reported that modifications to collagen, such as glycation, can alter both the binding of lipoproteins such as low-density lipoprotein (LDL) to these ECM

proteins and modify the potential of these lipoproteins to undergo oxidation [52], which is key to influence these molecules can have pathologically. These ECM-driven presentations of secreted and circulating factors can drive changes in cell behavior and phenotype that, as in the case of VIC activation, produce cell-driven alterations in the structure and content of ECM proteins.

The impact of the ECM in not limited to acting as delivery method for circulating factors. The ECM itself is capable of influence cell behavior. In the case of the valve, collagen has been shown to decrease VIC expression of markers indicative of an activated phenotype [5]. Mechanical properties of the ECM have also been shown to influence cell behavior [53, 54]. In the context of CAVD, stiffness of the substrates VICs were seeded on was able to drive their differentiation into aVICs or obVICs [47, 55]. This observation is critical for further understanding of CAVD etiology, as the valve is comprised of three, mechanically distinct layers of ECM that stiffen during disease progression [14, 17, 22]. The mechanical properties of the ECM can also alter VIC response to pathological stimuli. TGF-β, for example, is only able to fully induce an activated VIC phenotype on a sufficiently stiff substrate [28, 56]. Interestingly, contraction of the ECM by myofibroblasts or mechanical tension has also been shown to alter the activity of TGF-β bound to the ECM, converting latent TGF-β into an active form that can bind to receptors on the cell [57], which in the case of VICs would promote further myofibroblastic differentiation and activity, stiffening the ECM, and creating a positive feedback loop [7]. This example highlights the role of the ECM in modulating

interactions between cells and pathological factors that contribute to CAVD pathogenesis.

1.3 Risk Factors for CAVD

Major risk factors for CAVD include age, male sex, metabolic syndrome, and tobacco smoking [58]. Aging is associated with a 2-fold increase in risk of CAVD for every 10 years of age [9, 11, 58, 59]. While this observation was previously thought to suggest CAVD was a degenerative disease, investigations over the last 20 years indicate CAVD is an active process, sharing many pathological characteristics with atherosclerosis [60-62]. However, few studies have exclusively investigated age-related changes in the aortic valve, due to the limited availability of healthy human specimens of different age ranges [63, 64].

Male sex is the next strongest risk factor for CAVD. Males have a 2-fold increased risk of developing CAVD compared to females [2, 65-67]. While many cardiovascular diseases affect males and females differently [66, 68-70], very little is known about the mechanisms responsible for creating these disparities. Despite increasing evidence suggesting that the sex of research specimens alters experimental outcome [2], investigations into sex-related differences have been limited. Recent investigations into CAVD support the hypothesis that males tend to exhibit higher levels of calcification during CAVD while females exhibit more fibrosis (Figure 1.7) [4, 65, 67]. However, the active mechanisms behind this sex-related difference are not fully understood.

While age and male sex are two major risk factors for CAVD, there are a number of other factors that influences a person's susceptibility to developing CAVD. Metabolic

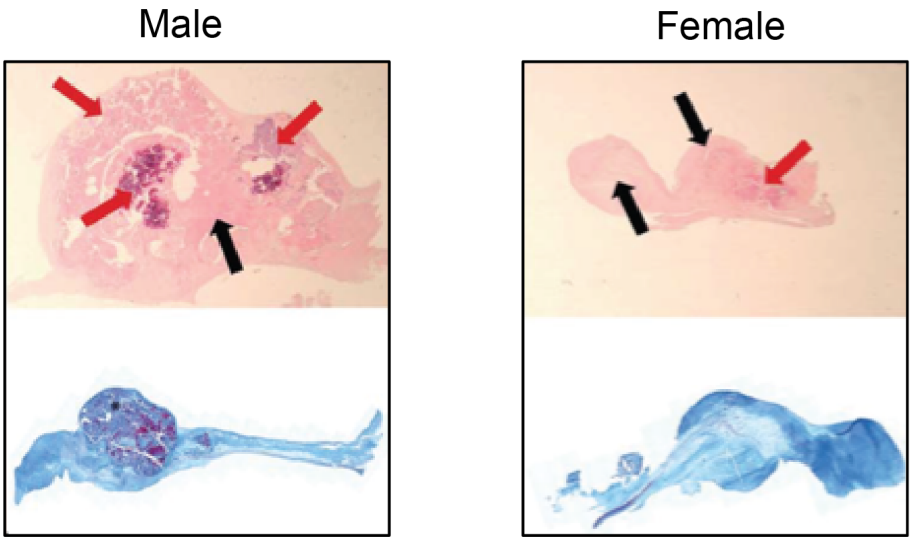

Figure 1.7 Sex-related differences in calcification (red) and fibrosis (black). [adapted from Simard et al. [4]]

syndrome is one risk factor for CAVD that may interact with sex and age-related changes in the valve to increase CAVD-related ECM dysfunction [71]. Metabolic syndrome is a collection of conditions including obesity, dyslipidemia, hypertension, and hyperglycemia that increases the risk of CAVD and other cardiovascular diseases [72]. While the definition of metabolic syndrome can vary in terms of which of these conditions is necessary for diagnosis, it must include a minimum of three of the aforementioned conditions [71, 72]. While the connection between metabolic syndrome and CAVD will not be explored in the work presented in this thesis, it is possible that there are underlying connections in the mechanisms which govern CAVD and metabolic syndrome, as both present in an age- and sex-based manner.

1.3.1 Aging

The ECM in many tissues undergoes changes during the aging process, resulting in alterations to tissue function [73-77]. These age-related ECM changes may be particularly pertinent to CAVD, where advanced age, defined as 65 years of age or older, is the primary risk factor [78, 79]. However, because aortic valve calcification was long viewed as a degenerative process that was simply a consequence of normal aging [27], many prior studies that examined “healthy” elderly valves did not exclude those with calcification [75, 80]. Thus, a full characterization of the aging aortic valve has only started to emerge in recent years, with most recent studies limited to analysis of age-related changes that occur prior to the age of typical CAVD onset. Valve features that exhibit age-related changes from childhood to adulthood (prior to age 65) include tissue-level characteristics such as increased leaflet stiffness [81, 82] as well as alterations in the composition [44], architecture [64], and crosslinking of specific valve ECM components [83]. Collagen crosslinking increases with age, as does the ratio of collagen III to collagen I due to increased production of collagen III [82]. Additionally, the valve ECM adapts to increases in diastolic blood pressure associated with aging by increasing collagen alignment [63, 64] and decreasing sulfated GAG content [64, 83]. Meanwhile, the majority of elastin remains localized to the ventricularis throughout the aging process [63, 64], yet alterations in elastin with aging have not been thoroughly investigated. However, as noted above, these studies do not encompass the age range of increased CAVD risk, so it remains uncertain whether these ECM alterations continue into late adulthood, when the risk of diseases such as CAVD increases.

In the absence of studies characterizing advanced aging of the aortic valve, reports on ECM changes in other tissues could provide insight into what may occur in the aortic valve past age 65. For example, many aged tissues exhibit both a decrease in collagen turnover rate and an increase in collagen crosslinking [84]. Similarly, aging of other cardiovascular tissues is accompanied by significant changes in molecules related to matrix remodeling, such as decreased MMP production in aged semilunar heart valves [85] or increased TIMP1 in myocardial tissue [81]. Some tissues also exhibit ECM stiffening with increased age [44] due to crosslinking induced by non-enzymatic protein glycation and the subsequent accumulation of advanced glycation end products (AGEs) [86]. AGEs can directly influence cell behavior [87, 88], and may alter collagen binding interactions with oxidized low-density lipoprotein (LDL) [52], which has been hypothesized to play an important role in CAVD progression [62, 89].

A compounding issue in the investigation into age-related ECM changes is that sex-dependent changes to the ECM have been reported. For example, studies into the myocardium revealed an increase in collaging III in female myocardium that is not observed in the male counterpart [81]. Considering male sex is the second highest risk factor for CAVD after age [58] and male VICs have been reported to express increased markers of ECM remodeling [90], future studies should differentiate the sex of patients to accurately characterize age-related changes in the valve.

1.3.2 Sex-Related Differences

Male sex has been implicated as a major risk factor for many diseases [69, 70, 91, 92]. However, it is only recently that studies into the differences between male and females

have been explored in relation to CAVD progression [2, 4, 90, 93]. As previously mentioned, a recent study by Simard et al. evaluated the level of aortic valve fibrosis and calcification in males and females scheduled for valve replacement due to severe aortic stenosis [4]. As indicated by hemodynamic severity via Doppler echocardiogram, it was reported that while males and females present with equal levels of aortic stenosis severity, males had higher levels of valvular calcification whereas females presented with higher levels of fibrosis [4]. This supports the results of a previous study that showed females displayed a similar severity of aortic stenosis compared to males, despite exhibiting lower levels of aortic valve calcification as measured by multidetector computed tomography [94].

In addition to *in vivo* studies, recent *in vitro* studies have reported sex-based differences in the expression of ALP and GAGs, with VICs from male swine expressing higher levels compared to VICs from female swine [90]. These findings support previous work that reported sex-based differences in the expression of 183 genes (Figure 1.8A) [2]. Analysis of these gene expression differences revealed higher expression in male VICs of genes associated with the development of CAVD (Figure 1.8B) [2]. Yet despite increasing data supporting sex-based differences in CAVD etiology, the extent of these differences is unclear.

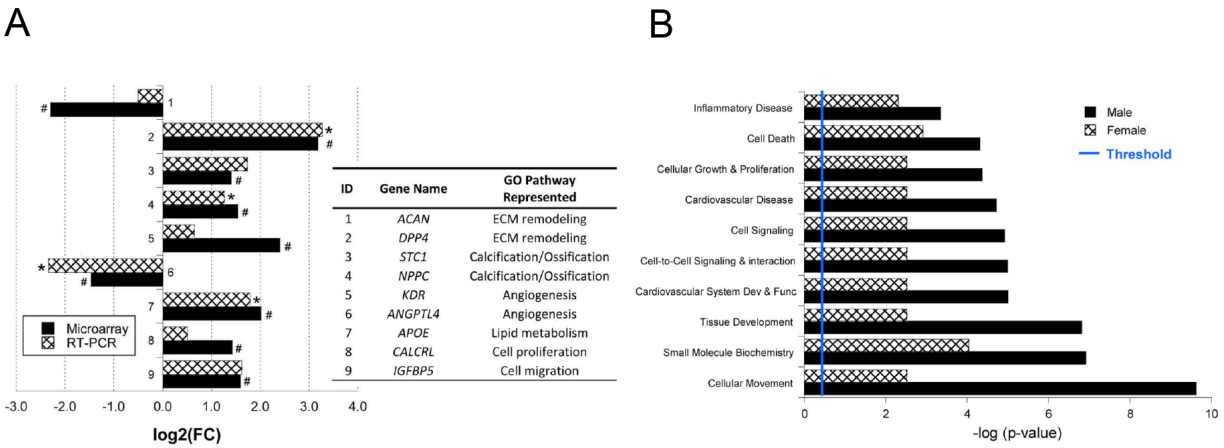

Figure 1.8 Sex related differences in gene expression of porcine VICs [adapted from McCoy et al. [2]]

1.4 2-D *In Vitro* Models of CAVD

Human specimens are vital for investigations into the pathology of CAVD and are utilized throughout this thesis. However, while tissue samples at end-stages of the disease are obtainable during valve replacement surgery, the availability of human specimens at earlier stages of CAVD progression is limited [95, 96]. Due to this limitation, *in vivo* and *in vitro* models have been used by researchers to investigate the underlying mechanisms of CAVD pathogenesis and support observations made using human specimens. While *in vivo* models such as mice and pigs are available, they are limited due either to their lack of ability to reproduce the trilaminar structure exhibited in human valves [97], do not reproduce the entire progression of CAVD [15], or are difficult due to the expense in maintaining the animals [95]. For these reasons, *in vitro* models are commonly utilized to identify the relationship between ECM alterations observed in human specimens and their influence on native cell populations [95].

Initial *in vitro* models of CAVD, like most traditional cell culture studies, used porcine VICs directly isolated from tissue and grown on 2-D tissue culture polystyrene (TCPS) [98]. This technique is still utilized in many studies despite the inability of this model to recreate many of the features of the native valve such as stiffness, mechanical stresses, and extracellular matrix interactions [96, 99]. However, VICs grown on TCPS spontaneously become activated, going from qVICS to aVICs [5, 29, 100], making this type of model useful for investigations into the role of aVICs in CAVD.

The 2-D environment can be altered to better mimic the native tissue environment and influence the phenotype of VICs by coating TCPS with specific ECM components [5, 101] or incorporating specific growth factors and cytokines into the growth media [102]. These alterations to the 2-D environment better mimic the native environment by providing integrin binding sites and other extracellular factors that VICs interact with *in vivo*. For example, VICs grown on collagen coated TCPS have shown decreased expression of aVIC markers, such as aSMA, compared to those on uncoated TCPS (Figure 1.9). Other ECM molecules such as fibrin have been shown to increase the activation level of VICs [5].

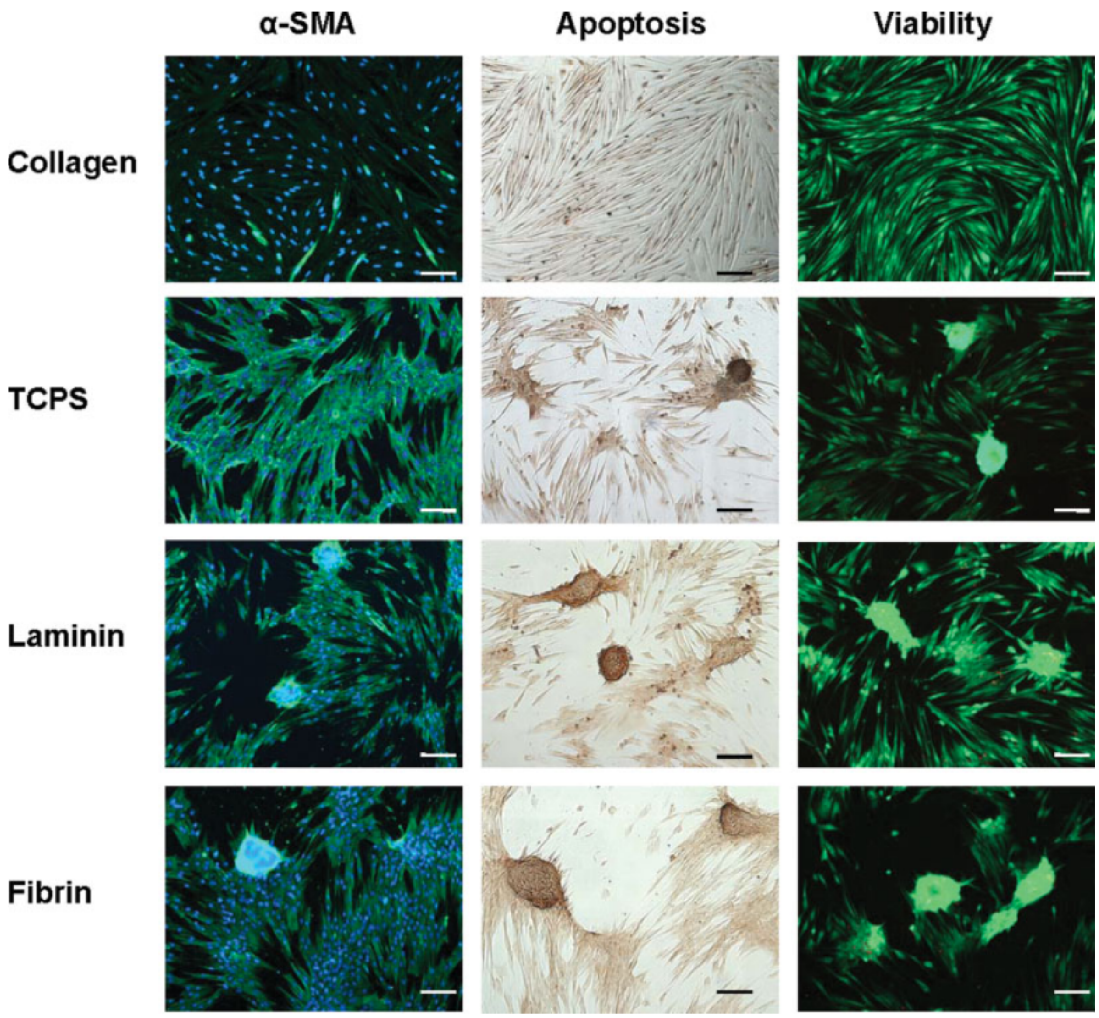

Figure 1.9 ECM influences VIC phenotype and viability. [adapted from Rodriguez et al. [5]]

In addition to modification to the culture substrate, *in vitro* models can be tailored to better mimic the state of a valve pathological state through modulation of medium formulation. Addition of TGF-β has been shown to augment aVIC phenotype through increased expression of aSMA and increased ECM deposition (Figure 1.4) compared to seeding on TCPS alone [37]. Osteogenic medium, TNF-α, and other cytokines have also been shown to promote VIC transdifferentiation in a 2-D TCPS environment [33,

102]. Meanwhile, maintenance of a qVIC phenotype is possible through culturing with low glucose media, insulin, and basic fibroblast growth factor (bFGF) on collagen-coated TCPS [103, 104]. These alterations of VICs phenotypes through modifications of medium allow for *in vitro* models to be tailored to investigate the interactions between specific VIC phenotypes and characteristics of ECM observed in human tissues and different *in vivo* models of CAVD.

To utilize these available *in vitro* models of VICs to their full potential it is necessary to further investigate how the valve ECM is altered due to aging, the sex of the tissue, and other risk factors of CAVD. Only through accurate characterization of the ECM at different stages of health and disease progression can we create *in vitro* models that accurately recapitulate the interactions between VICs and the native ECM to understand the underlying mechanisms that drive CAVD initiation and progression. Throughout this thesis, we aim to investigate these ECM changes in the valve in response to disease progression and risk factors for CAVD to further our understanding of the disease and promote the creation of new *in vitro* models of the valve ECM.

Elements of this chapter are in preparation for publication in a review paper by:
Hutson HN, Simon L, Porras AM, Masters KS.

1.5 References

1. Hutcheson, J., E. Aikawa, and W.D. Merryman, *Potential drug targets for calcific aortic valve disease.* Nature reviews. Cardiology, 2014. **11**.
2. McCoy, C.M., D.Q. Nicholas, and K.S. Masters, *Sex-related differences in gene expression by porcine aortic valvular interstitial cells.* PLoS ONE, 2012. **7**.

3. Schoen, F.J., *Mechanisms of Function and Disease of Natural and Replacement Heart Valves.* Annual Review of Pathology: Mechanisms of Disease, 2012. **7**: p. 161-183.
4. Simard, L., et al., *Sex-Related Discordance Between Aortic Valve Calcification and Hemodynamic Severity of Aortic Stenosis Is Valvular Fibrosis the Explanation ?* 2016.
5. Rodriguez, K.J. and K.S. Masters, *Regulation of valvular interstitial cell calcification by components of the extracellular matrix.* Journal of biomedical materials research. Part A, 2009. **90**: p. 1043-53.
6. Rock, C.a., L. Han, and T.C. Doehring, *Complex collagen fiber and membrane morphologies of the whole porcine aortic valve.* PloS one, 2014. **9**: p. e86087.
7. Chen, J.-H. and C.a. Simmons, *Cell-matrix interactions in the pathobiology of calcific aortic valve disease: critical roles for matricellular, matricrine, and matrix mechanics cues.* Circulation research, 2011. **108**: p. 1510-24.
8. Stephens, E.H., et al., *Differential proteoglycan and hyaluronan distribution in calcified aortic valves.* Cardiovascular Pathology, 2011. **20**: p. 334-342.
9. O'Brien, K.D., *Pathogenesis of calcific aortic valve disease: a disease process comes of age (and a good deal more).* Arteriosclerosis, thrombosis, and vascular biology, 2006. **26**: p. 1721-8.
10. Go, A.S., et al., *Executive summary: Heart disease and stroke statistics-2013 update: A Report from the American Heart Association.* Circulation, 2013. **127**: p. 143-152.
11. Sathyamurthy, I., et al., *Risk factor profile of calcific aortic stenosis.* Indian Heart Journal, 2016. **68**: p. 828-831.
12. Faggiano, P., et al., *Epidemiology and cardiovascular risk factors of aortic stenosis.* 2006. **10207**: p. 1-5.
13. Akat, K., M. Borggrefe, and J.J. Kaden, *Aortic valve calcification: basic science to clinical practice.* Heart (British Cardiac Society), 2009. **95**: p. 616-623.
14. Li, C., S. Xu, and A.I. Gotlieb, *The progression of calcific aortic valve disease through injury, cell dysfunction, and disruptive biologic and physical force feedback loops.* Cardiovascular pathology : the official journal of the Society for Cardiovascular Pathology, 2013. **22**: p. 1-8.
15. Rajamannan, N.M., et al., *Calcific aortic valve disease: not simply a degenerative process: A review and agenda for research from the National Heart and Lung and Blood Institute Aortic Stenosis Working Group. Executive summary: Calcific aortic valve disease-2011 update.* Circulation, 2011. **124**: p. 1783-91.
16. Larsson, S.C., A. Wolk, and M. Bäck, *Alcohol consumption, cigarette smoking and incidence of aortic valve stenosis.* Journal of Internal Medicine, 2017.
17. Sacks, M.S., W. David Merryman, and D.E. Schmidt, *On the biomechanics of heart valve function.* Journal of Biomechanics, 2009. **42**: p. 1804-1824.
18. Schoen, F.J., *Morphology , Clinicopathologic Correlations , and Mechanisms in Heart Valve Health and Disease.* Cardiovascular Engineering and Technology, 2016.
19. Schoen, F.J., *Evolving concepts of cardiac valve dynamics: The continuum of development, functional structure, pathobiology, and tissue engineering.* Circulation, 2008. **118**: p. 1864-1880.

20. Schoen, F.J., *Evolving concepts of cardiac valve dynamics: the continuum of development, functional structure, pathobiology, and tissue engineering.* Circulation, 2008. **118**: p. 1864-80.
21. Sacks, M.S., W. David Merryman, and D.E. Schmidt, *On the biomechanics of heart valve function.* Journal of biomechanics, 2009. **42**: p. 1804-24.
22. Stella, J.a. and M.S. Sacks, *On the biaxial mechanical properties of the layers of the aortic valve leaflet.* Journal of biomechanical engineering, 2007. **129**: p. 757-766.
23. Sacks, M.S., D.B. Smith, and E.D. Hiester, *The aortic valve microstructure: Effects of transvalvular pressure.* Journal of Biomedical Materials Research, 1998. **41**: p. 131-141.
24. Liu, A.C., V.R. Joag, and A.I. Gotlieb, *The emerging role of valve interstitial cell phenotypes in regulating heart valve pathobiology.* The American journal of pathology, 2007. **171**: p. 1407-18.
25. Freeman, R.V. and C.M. Otto, *Spectrum of calcific aortic valve disease: Pathogenesis, disease progression, and treatment strategies.* Circulation, 2005. **111**: p. 3316-3326.
26. Vahanian, A., et al., *Guidelines on the management of valvular heart disease (version 2012).* European Heart Journal, 2012. **33**: p. 2451-2496.
27. Buchanan, R.M. and M.S. Sacks, *Interlayer micromechanics of the aortic heart valve leaflet.* Biomech Model Mechanobiol, 2014. **13**(4): p. 813-26.
28. Yip, C.Y.Y. and C.a. Simmons, *The aortic valve microenvironment and its role in calcific aortic valve disease.* Cardiovascular pathology : the official journal of the Society for Cardiovascular Pathology, 2011. **20**: p. 177-82.
29. Rabkin-Aikawa, E., et al., *Dynamic and reversible changes of interstitial cell phenotype during remodeling of cardiac valves.* The Journal of heart valve disease, 2004. **13**: p. 841-7.
30. Taylor, P.M., et al., *The cardiac valve interstitial cell.* The international journal of biochemistry & cell biology, 2003. **35**: p. 113-8.
31. Derbali, H., et al., *Increased biglycan in aortic valve stenosis leads to the overexpression of phospholipid transfer protein via Toll-like receptor 2.* The American journal of pathology, 2010. **176**: p. 2638-2645.
32. Parolari, A., et al., *Nonrheumatic calcific aortic stenosis : an overview from basic science to pharmacological prevention §.* 2018. **35**.
33. Kaden, J.J., et al., *Inflammatory regulation of extracellular matrix remodeling in calcific aortic valve stenosis.* Cardiovascular pathology : the official journal of the Society for Cardiovascular Pathology, 2005. **14**: p. 80-7.
34. Kofler, S., T. Nickel, and M. Weis, *Role of cytokines in cardiovascular diseases: a focus on endothelial responses to inflammation.* Clinical science (London, England : 1979), 2005. **108**: p. 205-13.
35. Wynn, T.a. and T.R. Ramalingam, *Mechanisms of fibrosis: therapeutic translation for fibrotic disease.* Nature Medicine, 2012. **18**: p. 1028-1040.
36. Jian, B., et al., *Progression of aortic valve stenosis: TGF-β1 is present in calcified aortic valve cusps and promotes aortic valve interstitial cell calcification via apoptosis.* Annals of Thoracic Surgery, 2003. **75**: p. 457-465.

37. Walker, G.a., et al., *Valvular myofibroblast activation by transforming growth factor-β: Implications for pathological extracellular matrix remodeling in heart valve disease.* Circulation Research, 2004. **95**: p. 253-260.
38. Rajamannan, N.M., et al., *Human aortic valve calcification is associated with an osteoblast phenotype.* Circulation, 2003. **107**: p. 2181-4.
39. Aikawa, E., et al., *Multimodality molecular imaging identifies proteolytic and osteogenic activities in early aortic valve disease.* Circulation, 2007. **115**: p. 377-386.
40. Dweck, M.R., et al., *Calcific Aortic Stenosis A Disease of the Valve and the Myocardium.* JAC, 2012. **60**: p. 1854-1863.
41. Tseng, H. and K.J. Grande-Allen, *Elastic fibers in the aortic valve spongiosa: a fresh perspective on its structure and role in overall tissue function.* Acta biomaterialia, 2011. **7**: p. 2101-8.
42. Stallons, M.V.G., et al., *Molecular Mechanisms of Heart Valve Development and Disease.* Etiology and Morphogenesis of Congenital Heart Disease, 2016: p. 145-151.
43. Grande-Allen, K.J., et al., *Glycosaminoglycan synthesis and structure as targets for the prevention of calcific aortic valve disease.* Cardiovascular research, 2007. **76**: p. 19-28.
44. Stephens, E.H., C.-K. Chu, and K.J. Grande-Allen, *Valve proteoglycan content and glycosaminoglycan fine structure are unique to microstructure, mechanical load and age: Relevance to an age-specific tissue-engineered heart valve.* Acta biomaterialia, 2008. **4**: p. 1148-60.
45. Raman, R., V. Sasisekharan, and R. Sasisekharan, *Structural Insights into biological roles of protein-glycosaminoglycan interactions.* Chemistry and Biology, 2005. **12**: p. 267-277.
46. David Merryman, W., *Mechano-potential etiologies of aortic valve disease.* Journal of Biomechanics, 2010. **43**: p. 87-92.
47. Yip, C.Y.Y., et al., *Calcification by valve interstitial cells is regulated by the stiffness of the extracellular matrix.* Arteriosclerosis, thrombosis, and vascular biology, 2009. **29**: p. 936-42.
48. Hinton, R.B., *Extracellular Matrix Remodeling and Organization in Developing and Diseased Aortic Valves.* Circulation Research, 2006. **98**: p. 1431-1438.
49. Lehti, S., et al., *Modified lipoprotein-derived lipid particles accumulate in human stenotic aortic valves.* PloS one, 2013. **8**: p. e65810.
50. Hutcheson, J.D., et al., *5-HT(2B) antagonism arrests non-canonical TGF-β1-induced valvular myofibroblast differentiation.* Journal of molecular and cellular cardiology, 2012. **53**: p. 707-14.
51. Porras, A.M., et al., *Creation of disease-inspired biomaterial environments to mimic pathological events in early calcific aortic valve disease.* 2017: p. 363-371.
52. Mccormick, S. and M.A. Parniak, *Non-enzymic glycation of collagen inhibits binding of oxidized low-density lipoprotein.* 1993. **1**.
53. Mullen, Conleth A., et al., *The Effect of Substrate Stiffness, Thickness, and Cross-Linking Density on Osteogenic Cell Behavior.* Biophysical Journal, 2015. **108**: p. 1604-1612.

54. Mason, B.N., et al., *Tuning three-dimensional collagen matrix stiffness independently of collagen concentration modulates endothelial cell behavior.* Acta Biomaterialia, 2013. **9**: p. 4635-4644.
55. Quinlan, A.M.T. and K.L. Billiar, *Investigating the role of substrate stiffness in the persistence of valvular interstitial cell activation.* Journal of biomedical materials research. Part A, 2012. **100**: p. 2474-82.
56. Simionescu, A., D.T. Simionescu, and N.R. Vyavahare, *Osteogenic responses in fibroblasts activated by elastin degradation products and transforming growth factor-β1: Role of myofibroblasts in vascular calcification.* American Journal of Pathology, 2007. **171**: p. 116-123.
57. Wipff, P.-j., et al., *Myofi broblast contraction activates latent TGF- β 1 from the extracellular matrix.* 2007. **179**: p. 1311-1323.
58. Stewart, B.F., et al., *Clinical Factors Associated With Calcific Aortic Valve Disease.* 1997. **29**: p. 630-634.
59. Rosenhek, R., et al., *Mild and moderate aortic stenosis. Natural history and risk stratification by echocardiography.* European heart journal, 2004. **25**: p. 199-205.
60. Johnson, L.L., et al., *Imaging RAGE expression in atherosclerotic plaques in hyperlipidemic pigs.* EJNMMI research, 2014. **4**: p. 26.
61. Kuusisto, J., et al., *Atherosclerosis-like lesions of the aortic valve are common in adults of all ages: a necropsy study.* Heart (British Cardiac Society), 2005. **91**: p. 576-82.
62. Porras, A.M., et al., *Development of Aortic Valve Disease in Familial Hypercholesterolemic Swine: Implications for Elucidating Disease Etiology.* Journal of the American Heart Association, 2015. **4**: p. e002254.
63. Oomen, P.J.A., et al., *Age-dependent changes of stress and strain in the human heart valve and their relation with collagen remodeling.* Acta Biomaterialia, 2016. **29**: p. 161-169.
64. Van Geemen, D., et al., *Age-dependent changes in geometry, tissue composition and mechanical properties of fetal to adult cryopreserved human heart valves.* PLoS ONE, 2016. **11**.
65. Hayashida, K., et al., *Sex-Related Differences in Clinical Presentation and Outcome of Transcatheter Aortic Valve Implantation for Severe Aortic Stenosis.* JAC, 2012. **59**: p. 566-571.
66. Moura, L.M., F. Rocha-gonçalves, and C. Gavina, *Is it time for sex-specific recommendations in aortic stenosis ?* 2017. **0**: p. 1-2.
67. Thaden, J.J., et al., *Sex-related differences in calcific aortic stenosis : correlating clinical and echocardiographic characteristics and computed tomography aortic valve calcium score to excised aortic valve weight.* 2018: p. 693-699.
68. Mikkola, T.S., et al., *Sex Differences in Age-Related Cardiovascular Mortality.* PLoS ONE, 2013. **8**: p. 410-414.
69. Piro, M., et al., *Sex-Related Differences in Myocardial Remodeling.* JAC, 2010. **55**: p. 1057-1065.
70. Leinwand, L.A. and L.A. Leinwand, *Sex is a potent modifier of the cardiovascular system Find the latest version : Sex is a potent modifier of the cardiovascular system.* 2003. **112**: p. 302-307.

71. Lehmkuhl, V.R.-z.E. and M.O. Weickert, *Gender differences in the metabolic syndrome and their role for cardiovascular disease.* 2006. **147**: p. 136-147.
72. Huang, P.L., *AT A GLANCE A comprehensive definition for metabolic syndrome.* 2009. **237**: p. 231-237.
73. Abrass, C.K., M.J. Adcox, and G.J. Raugi, *Aging-associated changes in renal extracellular matrix.* The American journal of pathology, 1995. **146**: p. 742-52.
74. Harman, D., *The aging process.* 1981. **78**: p. 7124-7128.
75. Sell, S. and R.E. Scully, *Aging Changes in the Aorti and Mitral Valves.* Calcification of Cardiac Valves, 1964. **46**.
76. Horn, M.A., et al., *Age-related divergent remodeling of the cardiac extracellular matrix in heart failure: Collagen accumulation in the young and loss in the aged.* Journal of Molecular and Cellular Cardiology, 2012. **53**: p. 82-90.
77. Brownlee, M., *Advanced protein glycosylation in diabetes and aging.* Annual review of medicine, 1995. **46**: p. 223-34.
78. Eckert, C.E., et al., *On the biomechanical role of glycosaminoglycans in the aortic heart valve leaflet.* Acta Biomater, 2013. **9**(1): p. 4653-60.
79. Talman, E.A. and D.R. Boughner, *Glutaraldehyde fixation alters the internal shear properties of porcine aortic heart valve tissue.* Ann Thorac Surg, 1995. **60**(2 Suppl): p. S369-73.
80. Waller, B.F., *The old-age heart: normal aging changes which can produce or mimic cardiac disease.* Clin Cardiol, 1988. **11**(8): p. 513-7.
81. Dworatzek, E., I. Baczko, and G. Kararigas, *Effects of aging on cardiac extracellular matrix in men and women.* Proteomics - Clinical Applications, 2016. **10**: p. 84-91.
82. Stenderup, K., *Aging is associated with decreased maximal life span and accelerated senescence of bone marrow stromal cells,.* Bone, 2003. **33**: p. 919-926.
83. Spadaccio, C., et al., *Cells and extracellular matrix interplay in cardiac valve disease : because age matters.* Basic Research in Cardiology, 2016. **111**: p. 1-22.
84. Asif, M., et al., *An advanced glycation endproduct cross-link breaker can reverse age-related increases in myocardial stiffness.* Proceedings of the National Academy of Sciences of the United States of America, 2000. **97**: p. 2809-13.
85. Aikawa, E., et al., *Human semilunar cardiac valve remodeling by activated cells from fetus to adult: Implications for postnatal adaptation, pathology, and tissue engineering.* Circulation, 2006. **113**: p. 1344-1352.
86. Verzijl, N., et al., *Effect of collagen turnover on the accumulation of advanced glycation end products.* The Journal of biological chemistry, 2000. **275**: p. 39027-31.
87. Schmidt, a.M., et al., *Cellular receptors for advanced glycation end products. Implications for induction of oxidant stress and cellular dysfunction in the pathogenesis of vascular lesions.* Arteriosclerosis and thrombosis : a journal of vascular biology / American Heart Association, 1994. **14**: p. 1521-1528.
88. Ge, J., et al., *Advanced glycosylation end products might promote atherosclerosis through inducing the immune maturation of dendritic cells.* Arteriosclerosis, Thrombosis, and Vascular Biology, 2005. **25**: p. 2157-2163.

89. Cote, C., et al., *Association between circulating oxidised low-density lipoprotein and fibrocalcific remodelling of the aortic valve in aortic stenosis.* Heart, 2008. **94**: p. 1175-1180.
90. Masjedi, S., et al., *Sex-related differences in matrix remodeling and early osteogenic markers in aortic valvular interstitial cells.* Heart and Vessels, 2017. **32**: p. 217-228.
91. Hormone-dependent, M.D., et al., *Sex Differences in the Gut.* 2013. **339**: p. 1084-1089.
92. Whitacre, C.C., *Sex differences in autoimmune disease.* 2001. **2**: p. 777-780.
93. Porras, A.M., C.M. Mccoy, and K.S. Masters, *Calcific aortic valve disease.* Circulation Research, 2017. **120**: p. 604-606.
94. Aggarwal, S.R., et al., *Sex Differences in Aortic Valve Calcification Measured by Multidetector Computed Tomography in Aortic Stenosis.* 2013: p. 40-48.
95. Bowler, M.a. and W.D. Merryman, *In vitro models of aortic valve calcification: solidifying a system.* Cardiovascular pathology : the official journal of the Society for Cardiovascular Pathology, 2014: p. 1-10.
96. Sider, K.L., M.C. Blaser, and C.a. Simmons, *Animal models of calcific aortic valve disease.* International journal of inflammation, 2011. **2011**: p. 364310.
97. Kokubo, H., et al., *Hesr2 knockout mice develop aortic valve disease with advancing age.* Arteriosclerosis, Thrombosis, and Vascular Biology, 2013. **33**: p. 1-2.
98. Masters, K.S., et al., *Designing scaffolds for valvular interstitial cells: cell adhesion and function on naturally derived materials.* Journal of biomedical materials research. Part A, 2004. **71**: p. 172-80.
99. Tibbitt, M.W. and K.S. Anseth, *Hydrogels as extracellular matrix mimics for 3D cell culture.* Biotechnology and Bioengineering, 2009. **103**: p. 655-663.
100. Brand, N.J., et al., *Cultured interstitial cells from human heart valves express both specific skeletal muscle and non-muscle markers.* The international journal of biochemistry & cell biology, 2006. **38**: p. 30-42.
101. Gu, X. and K.S. Masters, *Regulation of valvular interstitial cell calcification by adhesive peptide sequences.* Journal of biomedical materials research. Part A, 2010. **93**: p. 1620-30.
102. Chen, J.-H., et al., *Identification and characterization of aortic valve mesenchymal progenitor cells with robust osteogenic calcification potential.* The American journal of pathology, 2009. **174**: p. 1109-19.
103. Latif, N., et al., *Modulation of Human Valve Interstitial Cell Phenotype and Function Using a Fibroblast Growth Factor 2 Formulation.* 2015: p. 1-19.
104. Porras, A.M., et al., *Robust Generation of Quiescent Porcine Valvular Interstitial Cell Cultures.* Journal of the American Heart Association, 2017. **6**: p. e005041.

CHAPTER 2: OBJECTIVES

2.1 Motivation

Calcific aortic valve disease (CAVD) is a prevalent disease with limited treatment options due to an insufficient understanding of its initiation and pathological progression. As discussed in the previous chapter, risk factors for CAVD are known, however there is limited understanding of the mechanisms that connect these risk factors with the development and progression of CAVD. These limitations motivate investigation into how two major risk factors, age and male sex, affect the valve extracellular matrix (ECM) and VIC phenotype. This thesis also aims to further characterize late-stage CAVD architectural changes in collagen, a major component in the aortic valve, to provide information at the microarchitectural level into ECM disarray during CAVD.

2.2 Objective 1: Assessment of changes in collagen architecture in CAVD

Valve ECM disarray is a known hallmark of CAVD [1, 2]. However, while collagen, a major ECM component of the aortic valve, is known to influence mechanical and biological properties of tissues, the microarchitectural changes that occur in collagen during CAVD is not fully understood [2]. In Chapter 3 this thesis describes an investigation into characterizing the microarchitecture of fibrillar collagen and related collagen modifications in human valves in the end-stage of CAVD. The studies described indicate that collagen disarray in CAVD is characterized by significant changes in fiber orientation in the fibrosa and spongiosa. An increase in collagen fibers

within the spongiosa was also noted, indicating a change in the mechanical stresses and loading experienced across the trilaminar structure of the valve.

2.3 Objective 2: Analysis of age-related extracellular matrix changes in the aortic valve

Despite being a known risk factor, there has been limited investigation into the connection between aging and alterations in the composition and distribution of extracellular matrix components of the valve, a known hallmark of CAVD [3]. The study in Chapter 4 aims to investigate age-related changes in fibrillar collagen and proteoglycans, two major ECM components of the aortic valve [1]. Results from these experiments revealed a decrease in collagen fiber width and increase in collagen fiber alignment with increased age in the fibrosa. Collagen fibers within the spongiosa were sparser in older valves. Proteoglycans remained consistent in both the fibrosa and spongiosa, which in comparison with previous studies using porcine models indicates the need for further investigation into aging using a combination of different models [4]. Expression of advanced glycation end products (AGEs) was also investigated. While there appeared to be a sex-related difference in AGEs, an in vitro model was created to further investigate the role of AGEs in CAVD.

2.4 Objective 3: Assessment of sex-related response of VICs to TGF-β1

Males have a 2-fold higher risk of developing CAVD compared to females. Initial studies, discussed in Chapter 1, indicate CAVD may have a sex-dependent progression, with males showing higher levels of calcification and females expressing

increased fibrosis [5]. Despite being a significant risk factor, investigations into sex-related differences in the progression of CAVD are limited [6]. The study discussed in chapter 6 uses a 2-D in vitro model to investigates the sex-related response of qVICs to a known disease stimuli, TGF-β1. Compared to females, male qVICs had higher proliferation and deposition of ECM proteins in response to TGF-β1. While both males and females exhibited an increase in expression of phosphorylated SMAD2/3 with increased TGF-β1, male expression was higher than females for each TGF-β1 treatment. The higher level of phosphorylated SMAD2/3 in males is likely due to a higher expression of total SMAD2/3 expressed in males across all conditions. While the cause of this sex-based difference in total SMAD2/3 is not fully understood, degradation of total SMAD2/3 in females in response to estrogen may play a role.

2.5 References

1. Chen, J.-H. and C.a. Simmons, *Cell-matrix interactions in the pathobiology of calcific aortic valve disease: critical roles for matricellular, matricrine, and matrix mechanics cues.* Circulation research, 2011. **108**: p. 1510-24.
2. Hutson, H.N., et al., *Calcific Aortic Valve Disease Is Associated with Layer-Specific Alterations in Collagen Architecture.* Plos One, 2016. **11**: p. e0163858.
3. Van Geemen, D., et al., *Age-dependent changes in geometry, tissue composition and mechanical properties of fetal to adult cryopreserved human heart valves.* PLoS ONE, 2016. **11**.
4. Stephens, E.H. and K.J. Grande-allen, *Porcine valve as a model for age-specific human heart valve disease : Analysis of collagen turnover throughout development and aging.* 2007. **205**: p. 2007.
5. Simard, L., et al., *Sex-related discordance between aortic valve calcification and hemodynamic severity of aortic stenosis.* Circulation Research, 2017. **120**: p. 681-691.
6. McCoy, C.M., D.Q. Nicholas, and K.S. Masters, *Sex-related differences in gene expression by porcine aortic valvular interstitial cells.* PLoS ONE, 2012. **7**.

CHAPTER 3: ANALYSIS OF LAYER SPECIFIC ALTERIATIONS IN COLLAGEN ARCHITECUTRE ASSOCIATED WITH CALCIFIC AORTIC VALVE DISEASE

Elements of this chapter have been published as:

Hutson, H. N., Marohl, T., Anderson, M., Eliceiri, K., Campagnola, P., & Masters, K. S. (2016). Calcific Aortic Valve Disease Is Associated with Layer-Specific Alterations in Collagen Architecture. *Plos One*, *11*(9), e0163858. http://doi.org/10.1371/journal.pone.0163858

3.1 Abstract

Disorganization of the valve extracellular matrix (ECM) is a hallmark of calcific aortic valve disease (CAVD). However, while microarchitectural features of the ECM can strongly influence the biological and mechanical behavior of tissues, little is known about the ECM microarchitecture in CAVD. In this work, we apply advanced imaging techniques to quantify spatially heterogeneous changes in collagen microarchitecture in CAVD. Human aortic valves were obtained from individuals between 50 and 75 years old with no evidence of valvular disease (healthy) and individuals who underwent valve replacement surgery due to severe stenosis (diseased). Second Harmonic Generation microscopy and subsequent image quantification revealed layer-specific changes in fiber characteristics in healthy and diseased valves. Specifically, the majority of collagen fiber changes in CAVD were found to occur in the spongiosa, where collagen fiber number increased by over 2-fold, and fiber width and density also significantly increased. Relatively few fibrillar changes occurred in the fibrosa in CAVD, where fibers became significantly shorter, but did not otherwise change in terms of number, width, density, or alignment. Immunohistochemical staining for lysyl oxidase showed localized

increased expression in the diseased fibrosa. These findings reveal a more complex picture of valvular collagen enrichment and arrangement in CAVD than has previously been described using traditional analysis methods. Changes in fiber architecture may play a role in regulating the pathobiological events and mechanical properties of valves during CAVD. Additionally, characterization of the ECM microarchitecture can inform the design of fibrous scaffolds for heart valve tissue engineering.

3.2 Introduction

The aortic heart valve is comprised of three distinct extracellular matrix (ECM) layers: the fibrosa, spongiosa, and ventricularis. Type I collagen is the predominant component of the fibrosa in healthy valves, while the spongiosa and ventricularis are primarily composed of proteoglycans and a collagen/elastin network, respectively [1]. This trilaminar structure is believed to be important in guiding both the biological and mechanical functions of the aortic valve [2], and its disruption occurs early in the development of calcific aortic valve disease (CAVD). Although valve failure is typically associated with extensive calcification of the valve structure, even mild leaflet fibrosis and thickening in the absence of calcification is correlated with an increase in cardiovascular and all-cause mortality [3, 4]. These consequences of leaflet thickening highlight the critical role of the ECM in maintaining valvular function, but the precise role and timing of altered ECM remodeling within the cascade of CAVD events remain unknown [5, 6].

Several studies in recent years have illustrated the powerful influence of the valvular ECM in regulating pathological events in valve tissues or cultures. For instance, 2-D investigations of valvular interstitial cells (VICs) cultured on different ECM coatings demonstrated that ECM identity can modulate VIC differentiation to a myofibroblastic or osteoblastic phenotype [7–9]. Forced disruption of targeted ECM components via enzymatic treatment of native leaflets provided 3-D evidence that confirmed the aforementioned 2-D findings [8, 10]. Examination of aortic valve leaflets from swine with homozygous familial hypercholesterolemia, a disease associated with a 1-in-2 chance of CAVD in humans [11, 12], revealed that ECM disorganization and the consequent leaflet thickening preceded almost all other hallmarks typically associated with CAVD [13].

The majority of valve ECM investigations have focused on bulk changes in ECM composition, but several studies have also examined nano- and microscale architecture in the valves. These examinations of ECM architecture in healthy valves from humans [14] and animals [15–19] have yielded valuable insight into fiber-level contributions to the unique mechanical properties of the valve. In highlighting the importance of fiber architecture in regulating the valvular response to mechanical loading, these studies also provide strong motivation to pursue quantification of ECM microarchitecture in human valves with CAVD, where altered valve mechanical performance plays a significant role in valve failure. The microarchitecture of ECM components can not only contribute to tissue mechanics, but also provide contact guidance cues that are highly influential in regulating cell function. Fibril/fiber features in type I collagen, such as

length, thickness, alignment, and density can regulate cellular behaviors such as cell polarity, motility, proliferation, and differentiation [20]. Culture of various cell types on substrates patterned with nano/micro-topographical features, as well as within scaffolds with varied fiber characteristics, have revealed numerous, highly specific architecture-dependent cellular phenomena, including downregulated fibrotic activity and promotion of a quiescent phenotype in corneal fibroblasts cultured on aligned fibers [21], increased motility of fibroblasts in areas of pattern anisotropy [22], or leading edge localization of focal adhesions and greater cytoskeletal alignment on dense, but not sparse, nanoscale grooves [23].

In the present study, we determine whether CAVD is associated with microarchitectural remodeling by quantifying collagen fiber characteristics, distribution, and crosslinking enzymes in age-matched healthy and diseased human aortic valves. Because standard histological and microscopy techniques can provide only limited information about ECM architecture, Second Harmonic Generation (SHG) microscopy was employed to accomplish this goal. SHG is an imaging technique that allows for direct imaging of collagen architecture without the need for exogenous stains or dyes [24]. The characterization of collagen structures enabled by this analysis can provide further insight into the pathological events that are capable of regulating both the biological and mechanical behaviors of valves during CAVD.

3.3 Methods and Materials

All reagents used were purchased from Sigma Aldrich (St. Louis, MO) unless otherwise indicated.

3.3.1 Tissue Acquisition and Classification

Aortic valve leaflets from individuals 50–75 years of age were collected from the University of Wisconsin Hospital and the William S. Middleton Veterans Memorial Hospital in Madison, WI. Healthy aortic heart valves were obtained within 24 hours postmortem from individuals with no previous diagnosis of CAVD; this protocol was reviewed by the UW-Madison IRB and granted an exemption (#2012–0721) due to not qualifying as human subjects research as defined under 45 CFR 46.102(f). Diseased valves were obtained from individuals undergoing aortic valve replacement surgery due to CAVD. Written consent was obtained from patients by the cardiothoracic surgery team, in accordance with protocol #2009–1094 approved by the UW-Madison IRB. These valves were confirmed as diseased by the cardiothoracic surgery team and a pathologist, and all had macroscopically visible and palpable calcification (example pictured in Fig 3.1). Tissues were embedded in paraffin and sectioned in 5 μm slices for histological staining or 13–15 μm slices for SHG imaging. Classification of valves as healthy or diseased was also confirmed via histological analysis. Specifically, the width of leaflet cross- sections that had undergone Movat's pentachrome staining was measured using ImageJ software [25] at 40 different locations within the tissue interior (i.e., a minimum of 100 μm from the free and attached edges). Leaflets <700 μm thick were considered healthy.

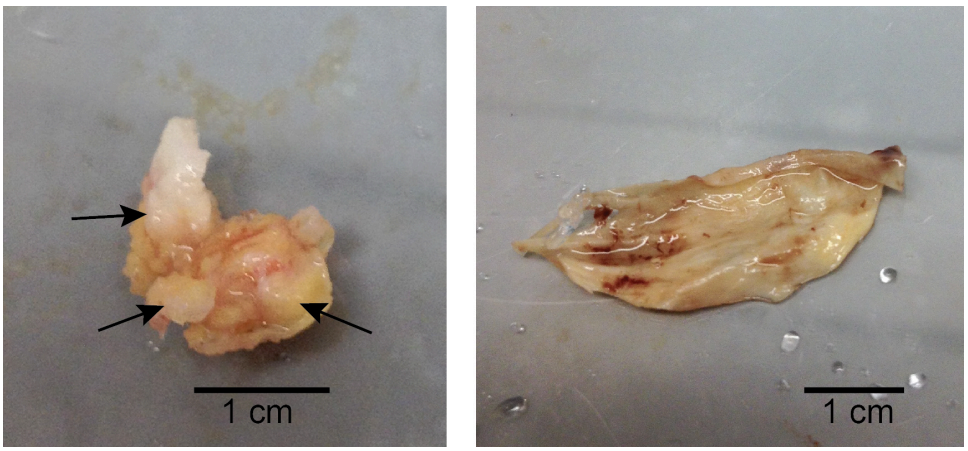

Figure 3.1 Representative images of a diseased leaflet (left) and a healthy leaflet (right) used in this study. Arrows indicate macroscopically evident calcified nodules

3.3.2 Histological Staining

Deparaffinized tissue sections were stained with Movat's pentachrome for connective tissue (Poly Scientific R&D Corp., Bay Shore, NY), mounted using Permount, and imaged using an Olympus IX51 inverted microscope. Picrosirius red staining was conducted as previously described [26] on sections from the belly region of the leaflet. Briefly, following deparaffinization tissue sections were stained using 0.1% (w/v) Direct Red 80 in saturated aqueous picric acid solution for one hour then washed twice in acidified water, followed by dehydration in graded washes of ethanol and xylene. Sections were mounted using Permount and imaged on an Olympus BX60 upright microscope with a DP25 camera using CellSens Standard software (V1.13) for both bright field and linearly polarized birefringence. Using FIJI (open source, version 2.0.0-rc-43/1.5e) [27] the birefringence of three areas of equal dimensions per tissue layer per

image was measured. The birefringence of each region of interest was quantified using a method previously described [28].

3.3.3 Second Harmonic Generation Imaging

In preparation for SHG imaging, tissue sections of the belly region of the leaflet were deparaffinized in xylene, followed by graded washes in ethanol before being mounted with coverslips sealed with lacquer. Prepared sections were stored at 4°C and imaged within 2 weeks. SHG imaging of collagen was achieved using a mode-locked 890 nm laser. SHG was measured at 445 nm with a 20 nm bandpass filter. As described elsewhere [29], SHG images were acquired using a 40x water-immersion objective, (working distance 3mm, 0.8NA) on an Olympus BX61 upright microscope (Olympus, Tokyo, Japan) using Olympus Fluoview300 scanning system at a 1x digital zoom.

3.3.4 Fiber Analysis

To quantify fiber characteristics, three SHG z-stacks were taken per tissue section from five dis- eased specimens and five healthy specimens of similar age. Images within the z-stack were taken every 1 μm throughout the entire section. Three serial images from the interior of each stack were analyzed together to negate signal changes due to tissue edge effects and to better characterize fibers angled out of a single plane. Analysis of fiber structure was performed using ctFIRE V1.3 Beta [30] and CurveAlignV3.0 Beta2, both of which are open source software developed by the Laboratory for Optical and Computational Instrumentation (LOCI) at the University of Wisconsin-Madison. SHG images (in 8-bit tiff format) were imported into the program where they underwent

curvelet transform (CT) reconstruction through use of CurveLab 2.1.2 (April 2008) followed by creation of fiber overlays via the FIRE algorithm [31]. Measurements from ctFIRE then underwent feature analysis through CurveAlign enabling output of final fiber features. MATLAB (The MathWorks, Inc., Natick, MA) was used as the platform to run the ctFIRE and CurveAlign software. The data from selected fibers were then exported from CurveAlign in Excel file format (Microsoft, Redmond, WA) to undergo statistical analysis.

The analysis described above yielded quantification of the following fiber features: length, width, curvature, density, and alignment. Fiber total length refers to the full length of the fiber within the plane of view, tracing along any curving or crimping the fibers may display, while the end-to-end length measurement is the straight distance from one end of the fiber to the other end, without tracing along the fiber. Curvature is a ratio of these two characteristics, thereby describing the degree of curving and/or crimping the fibers display. Fiber width is the average width of the fiber along its length. Fiber density and alignment were measured in relation to the nearest 2, 4, 8, and 16 nearest neighboring fibers as well as in image regions of defined area: 11.25 μm x 11.25 μm, 22.5 μm x 22.5 μm, and 45 μm x 45 μm. Box density refers to the number of fibers within a specified area, while Distance to Nearest indicates the distance to the closest of a specified number of fibers. Alignment of Nearest and Box Alignment are calculated in relation to the nearest of a specified number of neighboring fibers and the alignment within a designated area, respectively; an alignment value of one indicates

parallel alignment to the neighboring fibers, while a value of zero indicates that the fiber is perpendicular to the specified comparison set.

3.3.5 Detection of ECM-Crosslinking Enzymes

Prior to immunohistological staining for lysyl oxidase (LOX) and procollagen-lysine,2-oxoglutarate 5-dioxygenase 1 (PLOD1), tissue sections were deparaffinized using xylene and rehydrated with decreasing concentrations of ethanol. Antigen retrieval was performed for 2 hours at 80°C in a citric acid solution (Vector Laboratories, Burlingame, CA). Staining for LOX was conducted using a rabbit polyclonal anti-LOX antibody (ab31238, Abcam, Cambridge, MA), while PLOD1 was detected using a rabbit polyclonal anti-PLOD1 antibody that recognizes the N-terminus (aa73-102) of human PLOD1 (ab171140, Abcam). Both colorimetric and fluorescent detection methods were used in order to yield images optimized for qualitative and quantitative analysis, respectively. For colorimetric detection, the Universal Vectastain Elite ABC system (Vector Laboratories) was used as the secondary antibody and combined with ImmPACT DAB Peroxidase (HRP) Substrate (Vector Laboratories). Tissues were then mounted using Aquamount and imaged on an Olympus IX51 inverted microscope. Fluorescence-based detection was conducted using an anti-rabbit biotinylated secondary antibody (Vector Laboratories) and Dylight-488 streptavidin tertiary antibody (Vector Laboratories). Tissue sections were mounted using Prolong Gold Antifade reagent and imaged.

Quantification of LOX and PLOD1 expression was performed by capturing three fluorescent images per tissue layer using an Olympus IX51 inverted microscope. Using FIJI, the integrated intensity of three areas of equal dimensions per tissue layer per image was measured.

LOX and PLOD1 were also quantified in digested tissue samples using a modified dot blot method [32]. Tissue sections (10 μm thickness) were digested overnight at 55°C in a solution of >600mAU/mL proteinase K (Qiagen, Hilden, Germany), diluted 1:8 in diH2O, followed by quantification of total protein content using a Micro BCA Assay kit (Thermo Fisher Scientific, Waltham, MA). Tissue digests were diluted to 5 μg/μL total protein, and 1 μL was loaded onto a PVDF membrane (Bio-Rad Laboratories, Hercules, CA) that had been soaked in methanol for one minute and rinsed in diH_2O for 5 minutes. Collagen quantification was completed using a picrosirius red dot blot method described previously [32], utilizing rat tail collagen type I to create a standard curve from 0.1 to 0.8 μg/μL.

LOX quantification was completed using the same tissue digests prepared for collagen quantification and diluted to 5 μg/μL total protein. A PVDF membrane (Bio-Rad) was prepared in the same manner as for collagen quantification, and a LOX standard curve (from 0.625 to 20 ng/μL) was created using a full-length human LOX protein (ab187448, Abcam). The membrane was loaded with 1 μL of each sample and standard. Standards and samples were fixed onto the membrane through incubation at 37°C for 5 minutes. Once fixed, the membrane was blocked in 5% non-fat, dry milk in 1x PBS for 1 hour at

room temperature with shaking. Following blocking, the membrane was incubated overnight at 4°Cwith the same anti-LOX antibody (Abcam) used above for immunohistological staining, diluted 1:1000 in a solution of 1% dry milk and 0.1% Tween-20 in 1x PBS. The membrane was then washed 4 times in 0.01% Tween-20 in 1x PBS before incubating for 1 hour in a secondary antibody solution at room temperature with shaking. The secondary antibody solution consisted of an anti-rabbit IgG HRP conjugated antibody (#20320, Alpha Diagnostic Intl. Inc, San Antonio, TX) diluted 1:10000 in 1% dry milk, and 0.1% Tween-20 in 1x PBS. Following incubation with the secondary solution, the membrane was washed 4 times in 0.01% Tween-20 in 1x PBS. The membrane was then incubated in SuperSignal™ ELISA Pico Chemiluminescent Substrate (Thermo Fisher) before imaging. Membranes for both collagen and LOX quantification were imaged using a ChemiDoc™ MP(Bio-Rad) and analyzed using FIJI. Before measurement of signals, the Subtract Background command was used, and signals were measured using a circular selector of the same size for all standards and samples on membrane.

3.3.6 COL1A1 and LOX Gene Expression via qRT-PCR

Isolation of RNA from tissues sections for qRT-PCR was completed using the RNeasy FFPE kit (Qiagen), which is specifically tailored for the isolation of RNA from tissues that were previously formalin fixed and paraffin embedded (FFPE). RNA quantity and quality was determined via Nanodrop (Thermo Fisher Scientific) before creation of cDNA using a High-Capacity cDNA Reverse Transcription Kit (Applied Biosystems, Carlsbad CA). RT-PCR amplification was conducted using Taqman Gene Expression Assays (Applied

Biosystems) for *Col1A1* (Hs00164004_m1) and *LOX* (Hs00180_m1). The ΔΔCt method was used to normalize to *GAPDH* (Hs02758991_g1) and determine relative expression of *Col1A1* and *LOX* genes compared to healthy samples.

3.3.7 Statistical Analysis

Statistical analysis of SHG fiber characteristics was completed in Prism6 (Graphpad Software, Inc., La Jolla CA) using a one-way ANOVA followed by a Tukey post hoc test. All other comparisons between two groups were completed using two-tailed, unpaired t-tests assuming unequal variance. Differences were considered to be significant when $p<0.05$. Each experiment was conducted using age-matched tissues from a total of 10 individuals (N = 5 healthy, N= 5 diseased) unless otherwise noted.

3.4 Results

3.4.1 Valve Classification

Histological measurement of leaflet cross-sections demonstrated an average leaflet thickness of 423.7 ± 163.0 μm for healthy specimens and 1866 ± 1032 μm for diseased specimens ($p = 0.03434$; Table 3.1). In all cases, the histological classification of healthy vs. diseased was consistent with the clinical evaluation of the valves. There was no statistically significant difference in the age of patients across the groups.

Table 3.1 Human valve specimen information

Sex	Diseased	Age (yrs)	Mean Age (yrs) (p = 0.825)	Tissue Thickness (μm)	Mean Thickness (μm) (p = 0.034)
Female	N	50	64.2 ± 9.42	422.6 ± 88.60	423.7 ± 163.0
Female	N	61		206.4 ± 63.06	
Male	N	66		515.5 ± 137.6	
Male	N	69		341.1 ± 210.4	
Male	N	75		633.0 ± 127.6	
Female	Y	50	65.6 ± 9.92	872.9 ± 346.4	1866 ± 1032
Male	Y	62		3398 ± 1895	
Female	Y	69		1409 ± 526.3	
Male	Y	73		1229 ± 1090	
Male	Y	74		2422 ± 946.0	

3.4.2 CAVD Is Accompanied by Layer-Specific Changes In Collagen Content

Movat's pentachrome staining of healthy human aortic valve leaflets showed a defined trilaminar ECM architecture and uniform thickness (Fig 3.2A). Collagen (yellow) was prevalent in the fibrosa and ventricularis, while glycosaminoglycans (blue) comprised the spongiosa, and elastin (black/purple) was localized to the ventricularis (Fig 3.2B).

This layered ECM structure was clearly disrupted in diseased leaflets (Fig 3.2A). Specifically, one of the most notable changes in the ECM of diseased valves was the enrichment of collagen (yellow) throughout the leaflet thickness (Fig 3.2B).

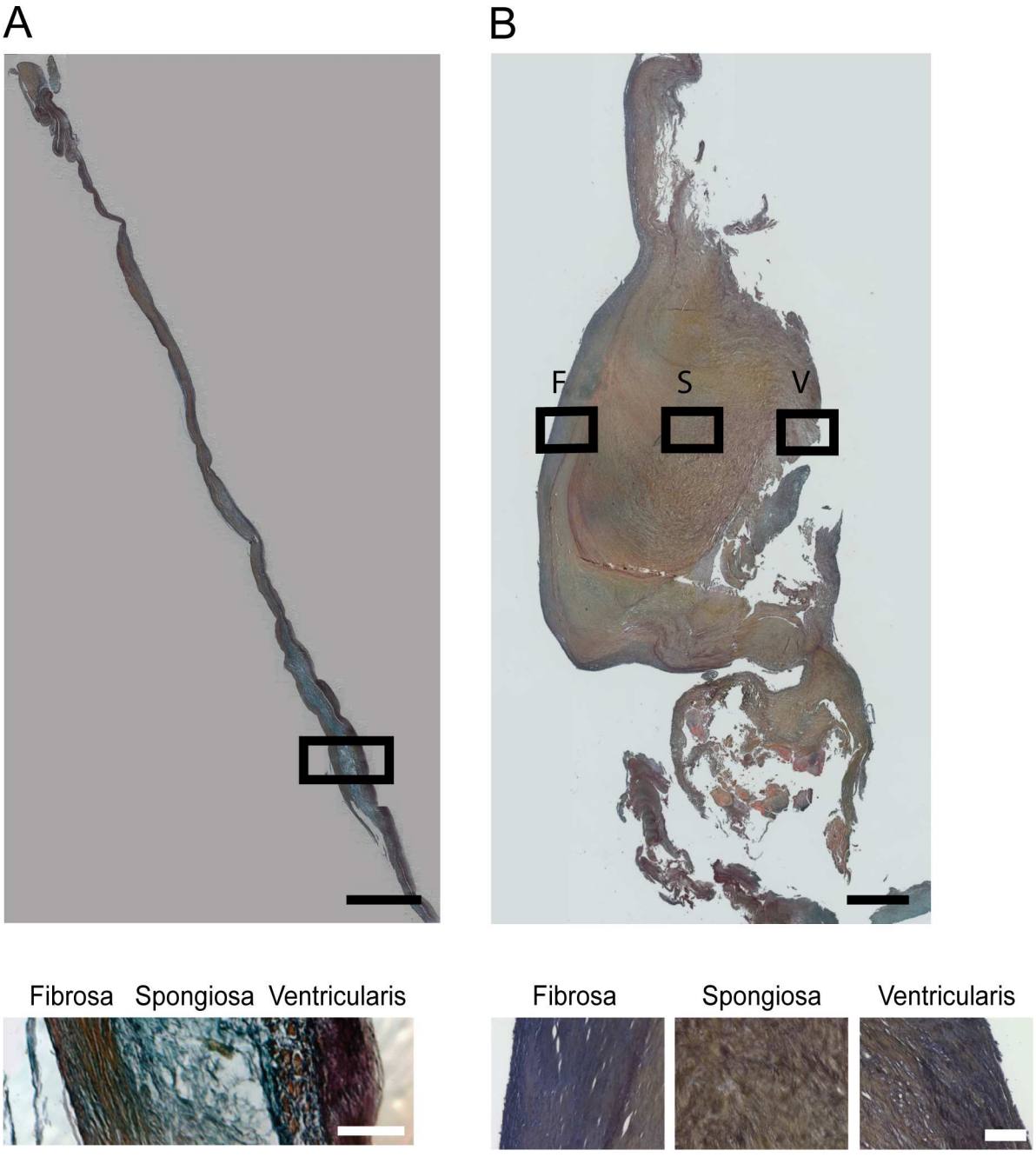

Figure 3.2 Representative images of human aortic valve leaflets stained with Movat's Pentachrome. Top: Images of a complete leaflet are shown for a representative (A) healthy and (B) diseased valve. F = fibrosa, S = spongiosa, V = ventricularis. Scale bar = 100 μm

To provide a more targeted analysis of collagen content and initial characterization of fiber organization, leaflets were stained with picrosirius red and imaged under polarized light. The birefringent color of collagen fibers viewed in this manner is commonly related to fiber diameter (where increasing diameter corresponds to transition from green to yellow to orange to red color), although other fiber features such as packing density and alignment may influence color [33]. In healthy leaflets, the fibrosa was densely populated with collagen fibers showing mainly orange-red birefringence (Fig 3.3A). Sporadic, thin collagen fibers were observed in the spongiosa and exhibited a yellow-green color under polarization. In the healthy ventricularis, brightfield imaging of picrosirius red staining showed faint collagen presence, but few collagen fibers were detected under birefringence, likely due to fibers being orthogonal to the plane of imaging.

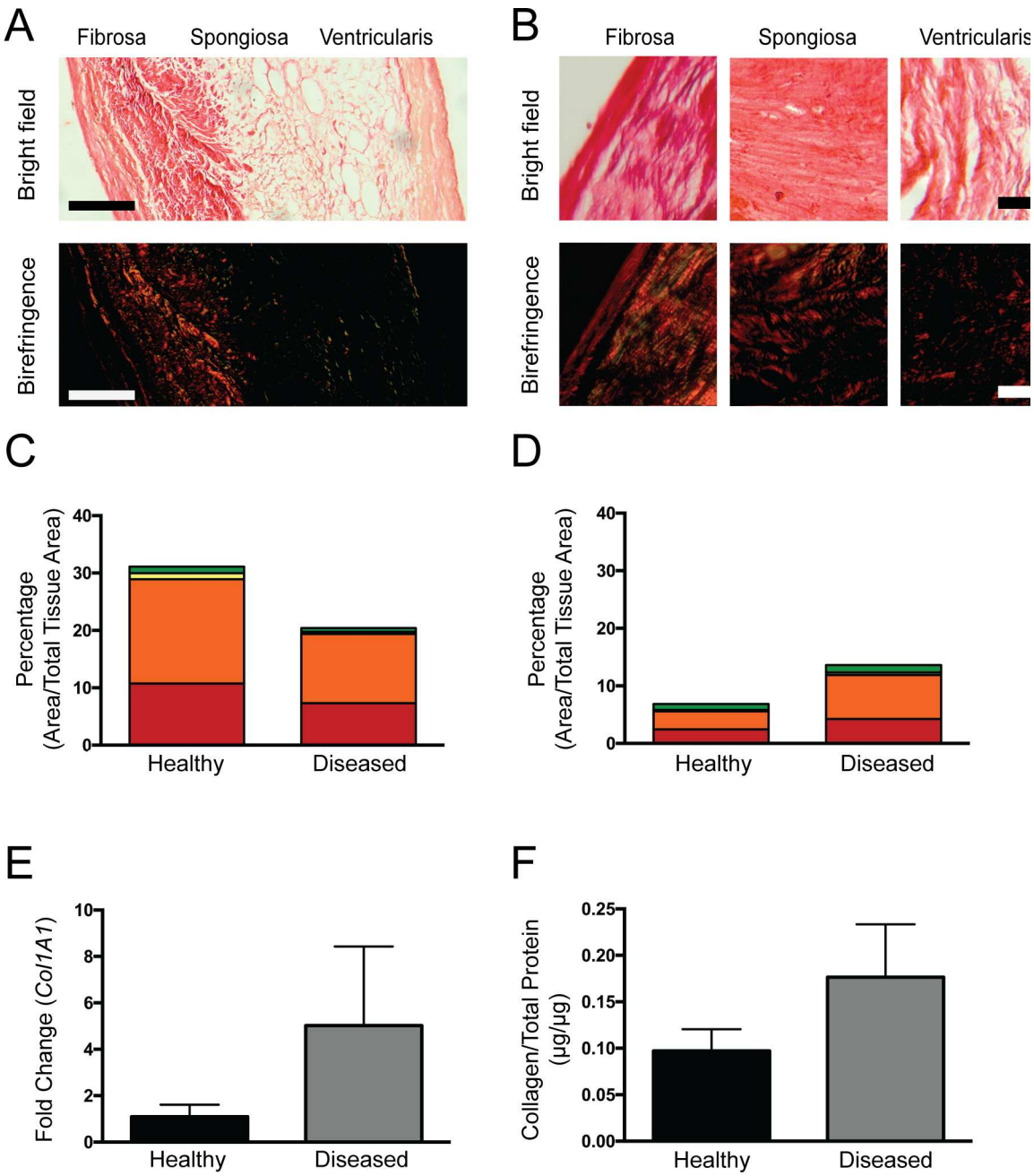

Figure 3.3 Visualization of collagen fibers via picrosirius red staining and quantification of collagen content. Picrosirius red staining of (A) healthy and (B) diseased leaflets was visualized using brightfield microscopy and polarized light. Birefringence hue and amount were quantified as a percent of total tissue area (N = 5, n = 3) in the (C) fibrosa and (D) spongiosa. Collagen production was also quantified via (E) qRT-PCR analysis of COL1A1 gene expression (N = 4, n = 3) and (F) measurement of total collagen protein via dot blot (N = 5 healthy; N = 4 diseased, n = 3).

In diseased leaflets, the fibrosa was densely populated with collagen fibers of orange-red birefringence (Fig 3.3B), similar to the fibrosa of healthy leaflets. The spongiosa in diseased leaflets, however, was densely populated with orange-red birefringent collagen fibers, which was in contrast with the spongiosa of healthy leaflets where little to no birefringence was observed. The percent of the tissue area occupied by birefringent collagen fibers was decreased in the fibrosa of diseased valves relative to healthy valves (Fig 3.3C), but was increased in the spongiosa with disease (Fig 3.3D). However, because fiber orientation can also impact the presence of birefringence, the changes in collagen content inferred from the birefringence analysis may actually be due to a combination of changes in collagen content and collagen fiber orientation. Traditional tissue-level analyses did not show a statistically significant increase in overall leaflet collagen content (Fig 3.3E) or *COL1A1* mRNA (Fig 3.3F).

Although imaging of picrosirius red staining under polarized light enables improved visualization of collagen fibers relative to other histological methods, only limited quantitative information about their architecture could be obtained in our tissues with this approach. Quantification of the amount of each birefringent hue in the fibrosa and spongiosa revealed few differences between the healthy and diseased samples for each layer (Fig 3.4). When comparing the spongiosa to the fibrosa, it appeared that the spongiosa was composed of more immature (i.e., thinner) fibers, as suggested by the presence of more green fibers. However, as noted above, the birefringence hue can change not only with fiber width, but also fiber density and alignment [33].

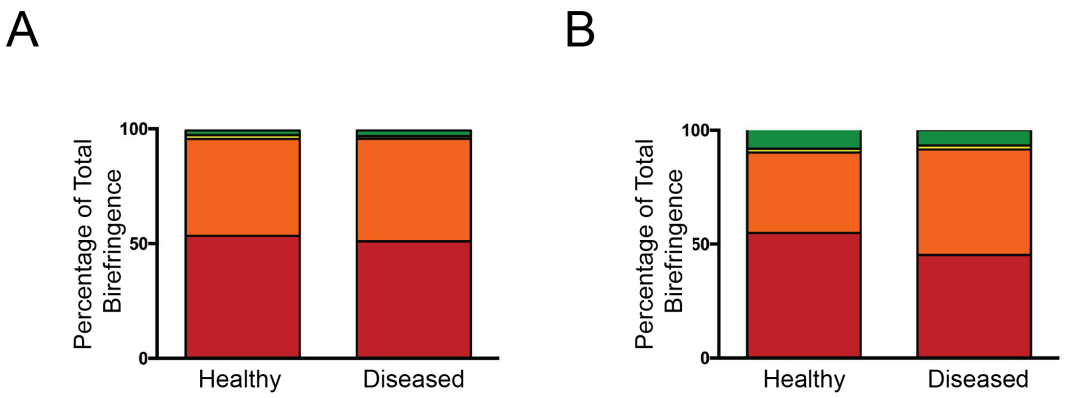

Figure 3.4 Distribution of birefringent hues in the fibrosa (A) and spongiosa (B), expressed as a percentage of total birefringence.

3.4.3 CAVD Is Accompanied by Layer-Specific Changes In Collagen Architecture

While picrosirius birefringence did reveal greater collagen fiber detail compared to Movat's staining, SHG imaging was employed to achieve greater and more directly quantifiable detail about fiber characteristics. SHG imaging of the fibrosa in both healthy and diseased valves showed densely-packed, radially-aligned collagen fibers (Fig 3.5A and 3.5B; Fig 3.6). The ventricularis in healthy valves contained collagen fibers oriented

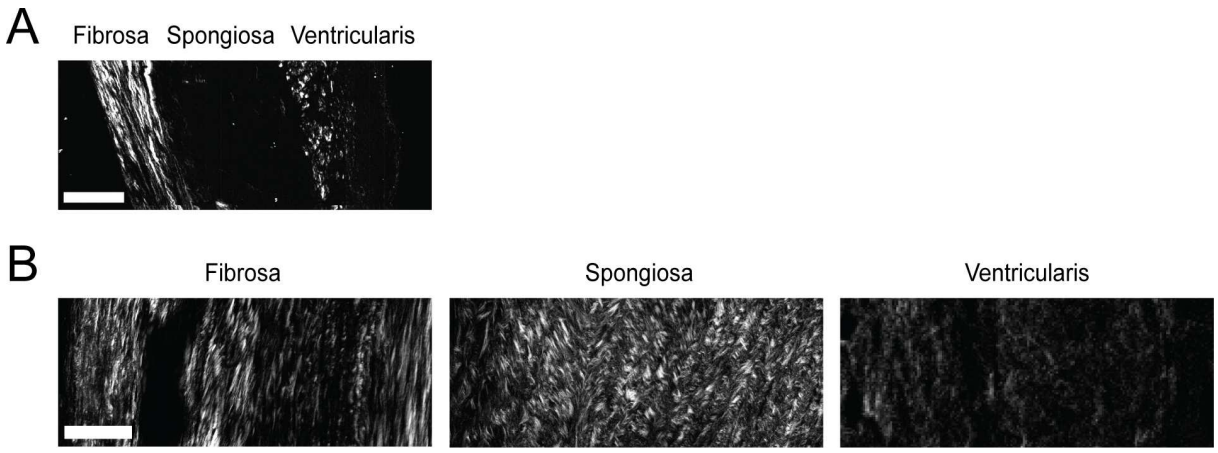

Figure 3.5 Visualization of collagen fiber microarchitecture using SHG microscopy. Representative images from (A) healthy and (B) diseased leaflets show microarchitectural changes in collagen in the fibrosa and spongiosa. Scale bar = 50 μm.

perpendicularly to those in the fibrosa, as viewed by fibers emanating outward from the viewing plane; the SHG signal from the ventricularis in diseased tissues was more diffuse, but the orthogonal imaging orientation of this layer precludes drawing conclusions about changes in fiber architecture. Finally, the most marked qualitative differences in collagen were seen in the spongiosa (Fig 3.7 and Fig 3.8). In contrast to the picrosirius red images, which showed some collagen fibers in the diseased spongiosa with limited distinction of individual fiber architecture, SHG imaging revealed an abundance of dense and disorganized collagen fibers in this layer, with clear distinction of individual fibers and their organization.

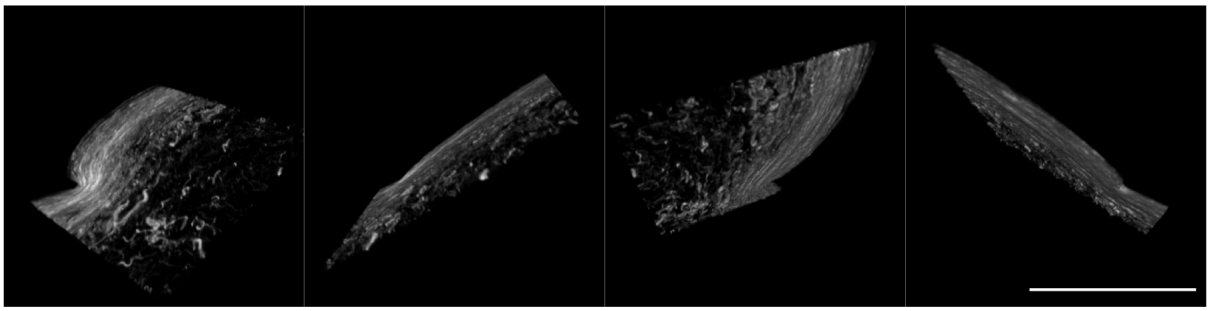

Figure 3.6 3D rendering of SHG images of collagen architecture in the fibrosa and spongiosa of a healthy valve. Images were captured from movie file as still photographs. Scale bar = 100 μm.

Quantitative analysis of SHG images yielded layer-specific data for characteristics of the individual collagen fibers. The ventricularis was omitted from this analysis for several reasons, including both significant logistical constraints and the consideration that this layer is generally not the site of valve calcification [34]. With respect to logistical constraints, accurate analysis of the fibers in the ventricularis would require *en face* leaflet sectioning to yield fibers laying within the imaging plane; because of the thinness of ventricularis, this approach would necessitate dedicated samples from a separate set of patients, with only one SHG section available per leaflet, and no ventricularis material available for complementary analyses (*e.g.*, immunohistochemistry, biochemical assays, PCR). Importantly, such sectioning would also not be possible in diseased valves, which are highly amorphous (Fig 3.2B). Thus, our acquisition of fiber data focused on the fibrosa and spongiosa. In the fibrosa, development of CAVD was associated with surprisingly few changes to fiber characteristics; there was a significant decrease in fiber length and a change in fiber orientation in the diseased fibrosa, but

fiber width, density, and alignment with neighboring fibers were not substantially changed (Table 3.2).

Table 3.2 Quantification of collagen fiber characteristics in the fibrosa and spongiosa of healthy vs. diseased aortic valve leaflets.

	FIBROSA		SPONGIOSA	
MEASUREMENT	**HEALTHY AVERAGE (30,093 fibers)**	**DISEASED AVERAGE (36,052 fibers)**	**HEALTHY AVERAGE (12,922 fibers)**	**DISEASED AVERAGE (31,417 fibers)**
FIBER DIMENSIONS				
Fiber Total Length (μm)	29 ± 2.3	25 ± 1.5^{F}	22 ± 2.6^{F}	22 ± 1.8
Fiber End-to-End Distance (μm)	26 ± 2.2	23 ± 1.6^{F}	20 ± 2.4^{F}	20 ± 1.8
Curvature	0.96 ± 0.0060	0.92 ± 0.0046	0.91 ± 0.0066^{F}	0.91 ± 0.0057
Fiber Width (μm)	1.9 ± 0.13	1.9 ± 0.033	1.7 ± 0.025^{F}	1.9 ± 0.089^{S}
FIBER DENSITY				
Distance to Nearest 2	7.7 ± 0.23	7.4 ± 0.16	9.8 ± 0.55^{F}	8.0 ± 0.77^{S}
Distance to Nearest 4	10 ± 0.33	9.5 ± 0.20	13 ± 0.84^{F}	10 ± 1.1^{S}
Distance to Nearest 8	14 ± 0.51	13 ± 0.25	19 ± 1.8^{F}	14 ± 1.6^{S}
Distance to Nearest 16	19 ± 0.65	18 ± 0.35	29 ± 3.5^{F}	20 ± 2.6^{S}
Box Density 11.25 x 11.25 μm	1.7 ± 0.031	1.7 ± 0.043	1.5 ± 0.050^{F}	1.7 ± 0.084^{S}
Box Density 22.5 x 22.5 μm	4.4 ± 0.15	4.7 ± 0.17	3.4 ± 0.27^{F}	4.3 ± 0.48^{S}
Box Density 45 x 45 μm	15 ± 1.2	16 ± 0.65	9.9 ± 1.3^{F}	14 ± 2.4^{S}
FIBER ALIGNMENT				
Fiber Absolute Angle (°)	69 ± 15	89 ± 28^{F}	73 ± 3.8	94 ± 26^{S}
Alignment of Nearest 2	0.90 ± 0.020	0.86 ± 0.031	0.82 ± 0.059^{F}	0.80 ± 0.047
Alignment of Nearest 4	0.86 ± 0.031	0.80 ± 0.045	0.73 ± 0.093^{F}	0.71 ± 0.072
Alignment of Nearest 8	0.83 ± 0.037	0.77 ± 0.052	0.68 ± 0.12^{F}	0.66 ± 0.092
Alignment of Nearest 16	0.82 ± 0.043	0.75 ± 0.057	0.64 ± 0.14^{F}	0.63 ± 0.11
Box Alignment 11.25 x 11.25 μm	0.94 ± 0.014	0.91 ± 0.023	0.91 ± 0.027	0.88 ± 0.020
Box Alignment 22.5 x 22.5 μm	0.86 ± 0.030	0.80 ± 0.045	0.78 ± 0.072	0.74 ± 0.057
Box Alignment 45 x 45 μm	0.82 ± 0.043	0.76 ± 0.057	0.69 ± 0.11	0.64 ± 0.093

F: $p<0.05$ vs. healthy fibrosa
S: $p<0.05$ vs. healthy spongiosa

Meanwhile, the nature of the changes in collagen fiber architecture that occurred in the diseased spongiosa had minimal overlap with the type of changes observed in the diseased fibrosa. For example, CAVD was associated with a decrease in fiber length and no change in width for collagen in the fibrosa, but collagen fibers in the spongiosa exhibited no change in length and a significant increase in width in diseased leaflets

(Table 3.2). Consistent with qualitative examination of SHG images and Fig 3.7 and Fig 3.8, quantitative fiber analysis confirmed a substantial increase in fiber number and density in the spongiosa of diseased valves relative to healthy conditions.

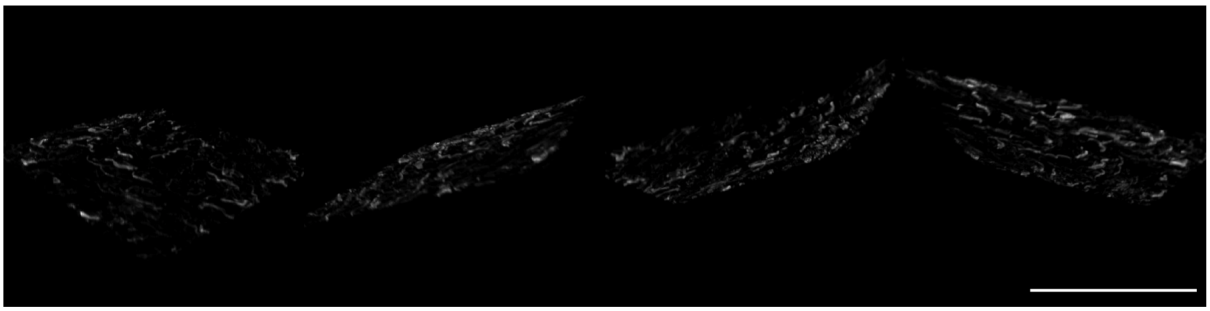

Figure 3.7 3D rendering of SHG images of collagen architecture in the spongiosa of a healthy valve. Images were captured from movie file as still photographs. Scale bar = 100 μm.

The boundary between the fibrosa and spongiosa in healthy leaflets is usually marked by a sudden decrease in collagen staining, which is consistent with our quantification of collagen fibers across these layers. Specifically, Table 3.2 shows significant differences between the healthy fibrosa and spongiosa for almost every collagen fiber parameter examined: total number, length, width, density, and alignment. However, in diseased leaflets, the abundance of collagen in the spongiosa appeared to blur this boundary, and the fibrosa and spongiosa became difficult to distinguish from each other both qualitatively and quantitatively.

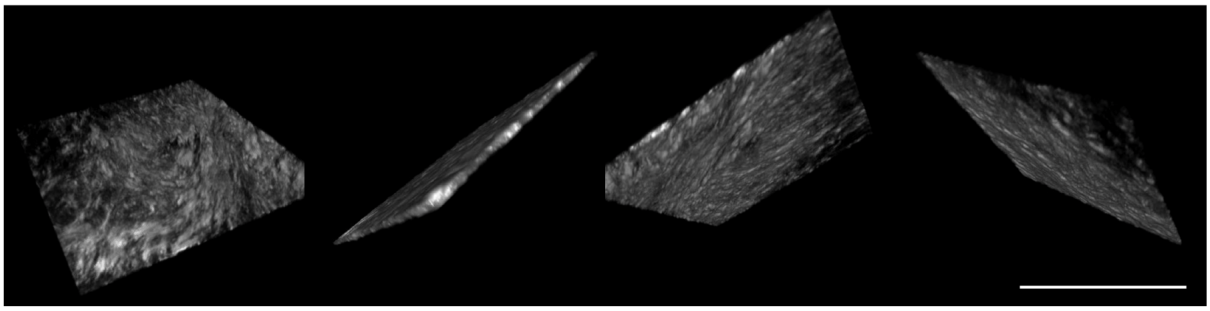

Figure 3.8 3D rendering of SHG images of collagen architecture in the spongiosa of a diseased valve. Images were captured from movie file as still photographs. Scale bar = 100 μm.

These two layers went from differing in almost all measurement areas in a healthy valve to no significant differences in any fiber feature in the diseased valve (Table 3.2). This increase in layer similarity in diseased valves appeared to be driven by fibers in the spongiosa becoming more similar to those in the fibrosa. For example, although fibers in the healthy spongiosa were much thinner than those in the healthy fibrosa (as observed in Fig 3.3 and Table 3.2), the thickening of fibers solely in the diseased spongiosa ultimately yielded an average fiber width that did not differ from that found in the corresponding fibrosa.

3.4.4 Increased LOX Expression in Diseased Fibrosa

We next investigated whether CAVD was associated with an increase in the production of enzymes involved in post-translational modification of collagen, specifically PLOD and LOX, as these molecules are capable of effecting changes in collagen fibrillar structure [35, 36]. PLOD is responsible for converting triple helical lysyl residues into hydroxylysine groups; this modification is a required step in the formation of fiber crosslinks and collagen maturation [36]. Immunohistochemical staining for PLOD1

showed relatively uniform presence of this enzyme across all leaflet layers, with no quantitative differences between healthy and diseased leaflets (Fig 3.9).

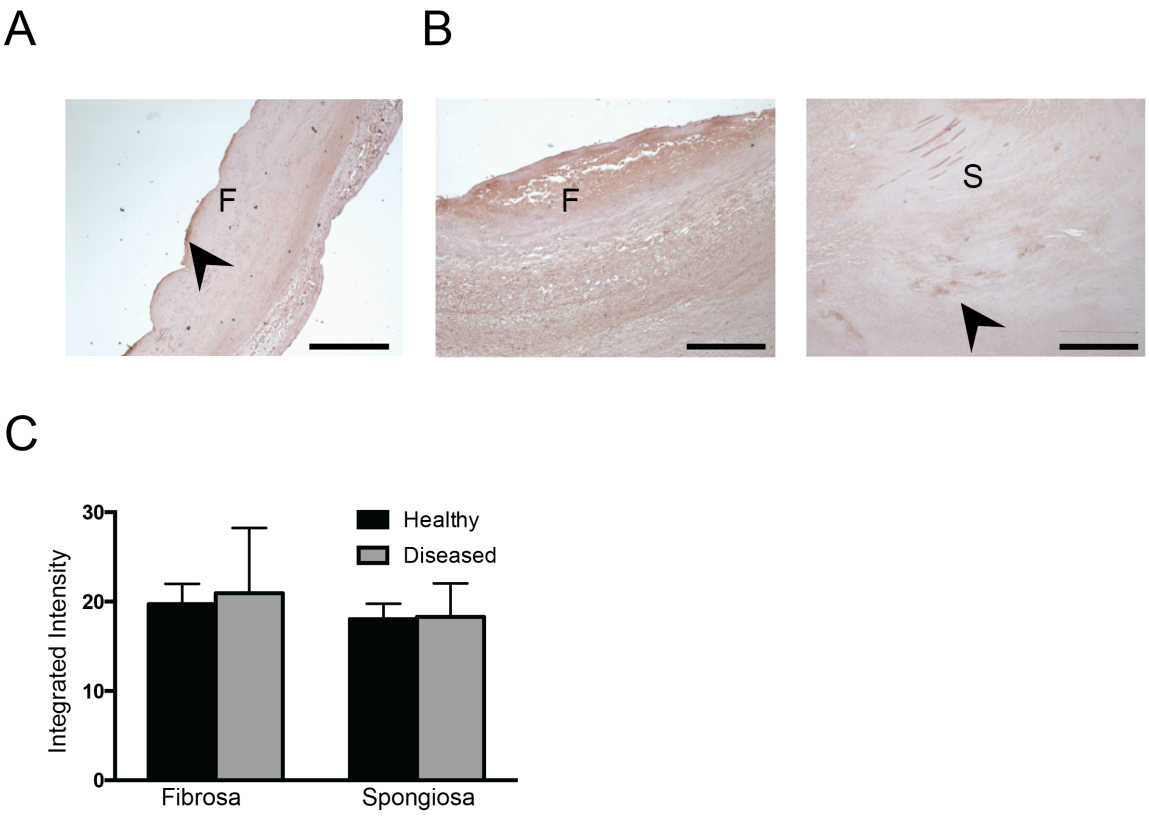

Figure 3.9 Immunohistochemical detection of PLOD1 in healthy and diseased aortic valve leaflets. Arrows indicate localized areas of positive PLOD1 staining. N=5.

We also measured the presence and expression of LOX, which catalyzes the formation of highly reactive aldehydes from lysyl residues and comprises the rate-limiting step in forming stable collagen fibrils [35]. In both healthy and diseased tissues, LOX was prevalent in the fibrosa and ventricularis, with fainter expression throughout the spongiosa (Fig 3.10A and 3.10B). However, the spongiosa of diseased leaflets also

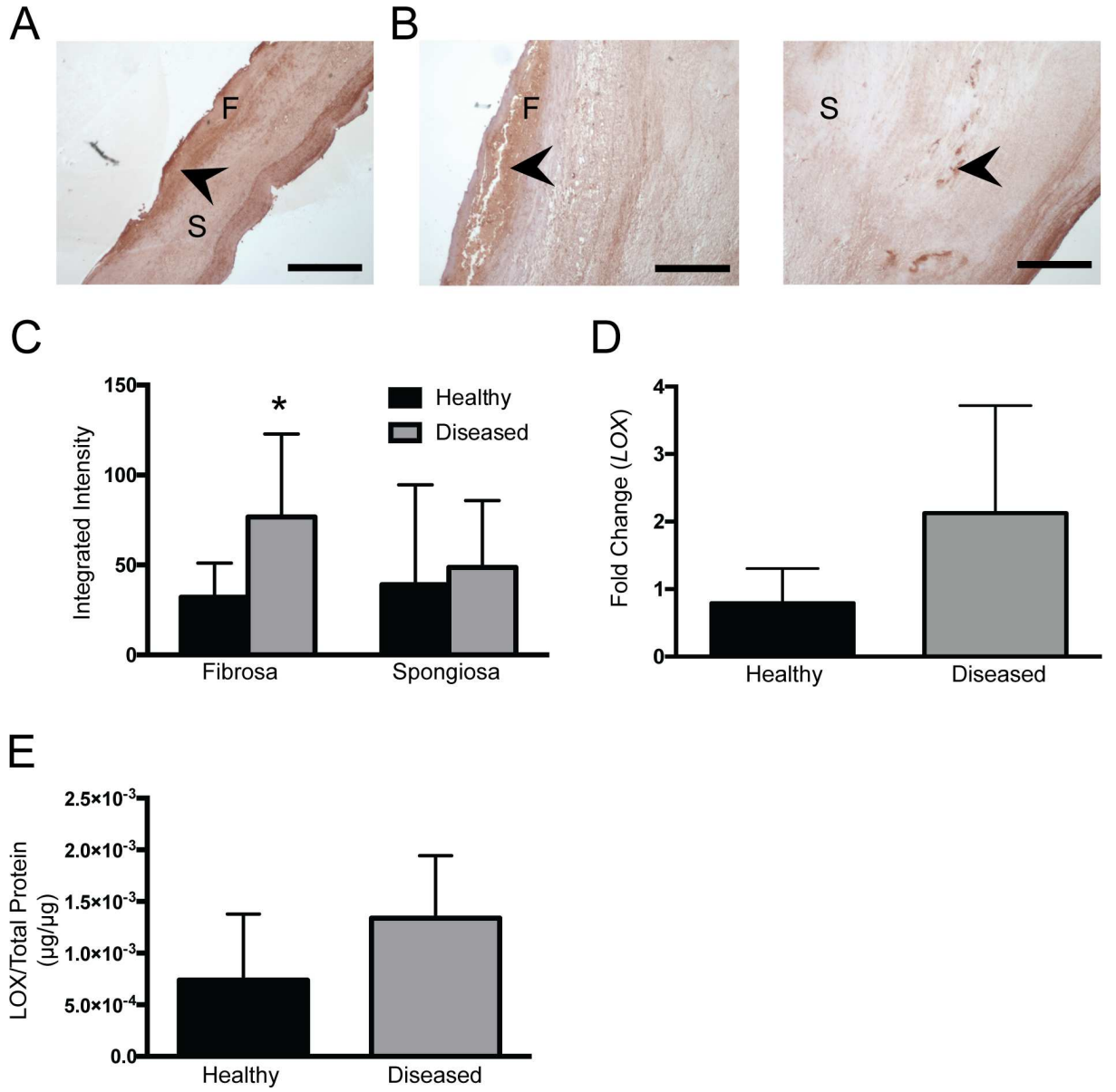

Figure 3.10 Immunohistochemical detection and quantification of lysyl oxidase (LOX) expression. Immunohistochemical staining of (A) healthy and (B) diseased leaflets shows distribution of LOX production throughout leaflet, with some areas of localized high- intensity staining (indicated by arrows). F = fibrosa, S = spongiosa. N = 5. Scale bar = 0.50 mm. (C) Layer-specific quantification of LOX staining, indicating significantly greater amounts of LOX in the diseased fibrosa relative to the healthy condition ($p = 0.001728$). N = 5, n = 3. Total LOX expression across the entire leaflet was also quantified via (D) qRT-PCR for *LOX* (N = 5, n = 3) and (E) measurement of LOX protein via dot blot (N = 5, n = 3).

contained localized areas of intense LOX staining, which were not seen in healthy valves. The expression of LOX was quantified via fluorescent staining, as shown in Fig 3.10C. While LOX expression was not significantly increased in the diseased spongiosa, there was a significant increase in LOX expression in the diseased fibrosa. Quantification of *LOX* mRNA and protein across the entire leaflet structure did not yield any statistically significant differences between healthy and diseased tissues (Fig 3.10D and 3.10E).

3.5 Discussion

Previous studies of valves with CAVD have noted an increase in collagen disorganization using traditional histological analysis techniques [6, 37]. However, the nature of this disorganization has not been clearly described, nor have its causes been elucidated. Although collagen fiber orientation in healthy human aortic valves has previously been characterized [14], the current work is the first to quantify collagen fiber characteristics in human valves with CAVD. Additionally, this work examined fiber architecture in healthy valves from elderly individuals (>65 years old), which has not previously been done, but is particularly important in the context of CAVD, where advanced age is the primary risk factor. Through the application of advanced imaging modalities, we were able to conduct a quantitative, layer-specific characterization of individual collagen fibers in these healthy and diseased aortic valves, demonstrating differences in the distribution, architecture, and post-translational modification of collagen in CAVD. Together, these findings reveal a more complex picture of collagen

enrichment and arrangement than has previously been described using traditional analysis methods, both with respect to the level of architectural quantification achieved using SHG, as well as the layer-specific quantification of collagen characteristics. The results from this analysis also motivated the quantification of collagen crosslinking enzymes, which have not been previously examined in healthy or diseased human aortic valves.

The combination of layer-specific analysis and fibrillar quantification revealed surprisingly few changes to the fibrosa during disease; fibers in the diseased fibrosa were significantly shorter than those in the healthy fibrosa, but otherwise had similar overall fiber number, width, density, and alignment. It should be noted that measurements for fiber length may be affected by fibers exiting the plane of imaging, and a change in fiber length could also be due to a change in fiber alignment out of the circumferential direction. However, fiber analyses of single-plane images from z-stacks yielded statistically similar length values as analyses of multiple merged images from z-stacks, which suggests that the changes in fiber length are not likely to be artifacts related to fiber clipping. In contrast to the fibrosa, the spongiosa underwent substantial changes to its collagen fiber structure with disease. There was a >2-fold increase in total number of collagen fibers in the diseased spongiosa, where the fibers maintained constant length, but became significantly wider and denser. These types of structural changes are important because they have the ability to alter both cellular behaviors and valve mechanical properties [38–40]. As noted earlier, features such as fiber width, density, and alignment can regulate cell polarity, proliferation, migration, ECM

production, and differentiation [20, 38]. Fiber alignment may also enjoy a reciprocal relationship with VIC orientation, as an investigation of porcine VICs in 3D collagen gels cultured under anisotropic cyclic strain found that increased VIC orientation can precede increased collagen fiber alignment [41]. VIC orientation may be an interesting parameter to evaluate in future studies of human valve disease, as it was found to strongly influence VIC phenotype *in vitro* [41].

Performance of our analysis in a layer-specific manner was also important in order to characterize the spatial heterogeneity in valve ECM rearrangement that was not evident in full-tissue analyses. Considering both the collagen quantification and LOX results together, it is possible that the changes in collagen architecture in the fibrosa and spongiosa are proceeding via different mechanisms. Specifically, because the diseased fibrosa exhibits decreased fiber length, little change in fiber number or density, and an increase in LOX, we speculate that collagen degradation is outpacing collagen biosynthesis in the diseased fibrosa, while crosslinking of existing fibers is increased. In contrast, the increase in fiber number and density in the spongiosa, without any change in LOX, could be an indication that the spongiosa is in a phase of elevated collagen production [42, 43]. These potential explanations are consistent with the picrosirius red birefringence analysis, which showed an abundance of mature collagen fibers in the fibrosa, and a greater proportion of immature fibers in the spongiosa (Fig 3.4).

Relating this work to existing literature on the ECM in sclerotic and stenotic valves, collagen “disorganization” is a common hallmark of CAVD [37], and our analysis

indicates that the collagen appears disorganized primarily due to it being strongly enriched in the spongiosa, rather than large-scale changes in collagen orientation or alignment. It is also useful to note that the general fibrillar arrangement within our healthy valve cohort appears qualitatively similar to that described for adult porcine valves [17, 18]. With respect to collagen remodeling, significantly increased production of both matrix metalloproteinases (MMPs) and their inhibitors (TIMPs) in human valves with CAVD has previously been described [44–46]; while some have found an imbalance favoring MMP production [44], others have hypothesized a more nuanced situation where the production of these molecules depends upon the local environment within the valve [46]. Our findings of differential collagen remodeling in different layers of the leaflet are in agreement with this hypothesis. Expression of collagen crosslinking enzymes has not previously been evaluated in human aortic valves, but an analysis of healthy porcine valves found more LOX in the spongiosa compared to the fibrosa of young, healthy valves, and an increase in the overall presence of LOX with advanced age [47]. Our findings differ in that we did not observe differences in the amount of LOX in the fibrosa vs. spongiosa in healthy human valves; this could be due to a difference in species, difference in age relative to the swine, or just greater heterogeneity amongst humans. The layer-by-layer approach to quantifying ECM architecture that was employed in this study may also be applied to further our understanding the layer-specific nature of valve calcification in human valves, where calcific deposits occur preferentially in the fibrosa [34]. Although many features likely contribute to this layer-specific nature of calcification, collagen architecture has not previously considered as a

factor that may influence this process; other studies of bone mineralization indicate that fiber organization can indeed regulate calcification [48].

Alterations in collagen fiber organization are also likely to impact the mechanical properties of the valve. The opposing alignment of collagen fibers in the fibrosa and ventricularis in healthy aortic heart valves is critical for maintaining appropriate opening and closure of the valve [2]. Significant changes in the orientation angle of fibers in both the diseased fibrosa and spongiosa, as well as the overall increase in collagen fibers in the spongiosa, may indicate that mechanical loads are being supported outside of the planes of mechanical stress that would be typical for a healthy aortic valve leaflet. This may be especially true for the spongiosa, which normally works to minimize friction between the stress-bearing fibrosa and ventricularis during healthy aortic valve function. An increase in collagen fiber density is likely to impede the ability of the spongiosa to insulate the mechanical properties of the fibrosa from the ventricularis and vice versa. Disruptions to the mechanical properties of the valve may not only influence its physical functionality, but also cellular behavior. For example, *in vitro* investigations have shown that increased substrate stiffness causes an increase in the expression of disease markers such as αSMA and apoptosis by VICs [49].

Finally, the use of high-resolution SHG in this work was found to enable a level of collagen fiber characterization not possible with histological approaches. The application of new approaches and complementary tools to characterize ECM organization is important for understanding the etiology of fibrotic diseases such as

CAVD. Because SHG does not require tissue fixation or staining, its use could advance current efforts to engineer fibrotic environments *in vitro* [50]. The combination of fibrosis tissue engineering with SHG may offer the ability to gain insight into fibrogenic processes through the non-invasive visualization of ECM dynamics in living cultures [51]. Recent work has also shown that SHG imaging of collagen alterations may be combined with machine learning algorithms to characterize the extent of fibrosis in clinical samples, as well as provide automated, high-throughput diagnoses of fibrotic disease [52–56]

3.6 Conclusions

The ECM, and specifically, collagen, is known to regulate cell behavior not only through its primary amino acid sequence, but also through its architecture and organization. Prior to the current work, the nano/micro-scale architecture of collagen had not been quantified in human valves with CAVD. The responsiveness of many other cell types to changes in nano/microtopographies and the changes in collagen fiber structure described herein motivate future investigations into whether these changes in ECM architecture are capable of influencing VIC function and/or calcification. The implications for this work range from gaining insight into the biological and mechanical events in valve pathology to informing the creation of scaffold environments for tissue engineering of valves.

3.7 References

1. Latif N, Sarathchandra P, Taylor PM, Antoniw J, Yacoub MH. Localization and pattern of expression of extracellular matrix components in human heart valves. J Heart Valve Dis. 2005; 14(2):218±27. PMID: 15792183
2. Ja Stella, Sacks MS. On the biaxial mechanical properties of the layers of the aortic valve leaflet. Journal of biomechanical engineering. 2007; 129:757±66. doi: 10.1115/1.2768111 PMID: 17887902
3. Rosenhek R, Klaar U, Schemper M, Scholten C, Heger M, Gabriel H, et al. Mild and moderate aortic stenosis. Natural history and risk stratification by echocardiography. Eur Heart J. 2004; 25(3):199± 205. doi: 10.1016/j.ehj.2003.12.002 PMID: 14972419
4. Volzke H, Haring R, Lorbeer R, Wallaschofski H, Reffelmann T, Empen K, et al. Heart valve sclerosis predicts all-cause and cardiovascular mortality. Atherosclerosis. 2010; 209(2):606±10. doi: 10.1016/j.atherosclerosis.2009.10.030 PMID: 19922935
5. Li C, Xu S, Gotlieb AI. The progression of calcific aortic valve disease through injury, cell dysfunction, and disruptive biologic and physical force feedback loops. Cardiovasc Pathol. 2013; 22(1):1±8. doi: 10.1016/j.carpath.2012.06.005 PMID: 22795219
6. Rajamannan NM, Evans FJ, Aikawa E, Grande-Allen KJ, Demer LL, Heistad DD, et al. Calcific aortic valve disease: not simply a degenerative process: A review and agenda for research from the National Heart and Lung and Blood Institute Aortic Stenosis Working Group. Executive summary: Calcific aortic valve disease-2011 update. Circulation. 2011; 124(16):1783±91. doi: 10.1161/CIRCULATIONAHA.110.006767 PMID: 22007101
7. Benton JA, Kern HB, Anseth KS. Substrate properties influence calcification in valvular interstitial cell culture. J Heart Valve Dis. 2008; 17(6):689±99. PMID: 19137803
8. Rodriguez KJ, Piechura LM, Masters KS. Regulation of valvular interstitial cell phenotype and function by hyaluronic acid in 2-D and 3-D culture environments. Matrix Biol. 2011; 30(1):70±82. doi: 10.1016/j.matbio.2010.09.001 PMID: 20884350
9. Rodriguez KJ, Masters KS. Regulation of valvular interstitial cell calcification by components of the extracellular matrix. J Biomed Mater Res A. 2009; 90(4):1043±53. doi: 10.1002/jbm.a.32187 PMID:18671262
10. Rodriguez KJ, Piechura LM, Porras AM, Masters KS. Manipulation of valve composition to elucidate the role of collagen in aortic valve calcification. BMC Cardiovasc Disord. 2014; 14:29. doi: 10.1186/1471-2261-14-29 PMID: 24581344
11. Kawaguchi A, Miyatake K, Yutani C, Beppu S, Tsushima M, Yamamura T, et al. Characteristic cardiovascular manifestation in homozygous and heterozygous familial hypercholesterolemia. Am Heart J.1999; 137(3):410±8. doi: 10.1016/s0002-8703(99)70485-0 PMID: 10047619
12. Rajamannan NM, Edwards WD, Spelsberg TC. Hypercholesterolemic aortic-valve disease. The New England journal of medicine. 2003; 349(7):717±8. doi: 10.1056/NEJMc031360 PMID: 12917318

13. Porras AM, Shanmuganayagam D, Meudt JJ, Krueger CG, Hacker TA, Rahko PS, et al. Development of Aortic Valve Disease in Familial Hypercholesterolemic Swine: Implications for Elucidating Disease Etiology. J Am Heart Assoc. 2015; 4(10):e002254. doi: 10.1161/JAHA.115.002254 PMID: 26508741
14. Aikawa E, Whittaker P, Farber M, Mendelson K, Padera RF, Aikawa M, et al. Human semilunar cardiac valve remodeling by activated cells from fetus to adult: implications for postnatal adaptation, pathology, and tissue engineering. Circulation. 2006; 113(10):1344±52. doi: 10.1161/CIRCULATIONAHA.105. 591768 PMID: 16534030
15. Schenke-Layland K, Riemann I, Opitz F, Konig K, Halbhuber KJ, Stock UA. Comparative study of cellular and extracellular matrix composition of native and tissue engineered heart valves. Matrix Biol.2004; 23(2):113±25. doi: 10.1016/j.matbio.2004.03.005 PMID: 15246110
16. Schenke-Layland K, Riemann I, Stock UA, Konig K. Imaging of cardiovascular structures using near infrared femtosecond multiphoton laser scanning microscopy. J Biomed Opt. 2005; 10(2):024017. doi:10.1117/1.1896966 PMID: 15910091
17. Mega M, Marom G, Halevi R, Hamdan A, Bluestein D, Haj-Ali R. Imaging analysis of collagen fiber networks in cusps of porcine aortic valves: effect of their local distribution and alignment on valve functionality. Comput Methods Biomech Biomed Engin. 2016; 19(9):1002±8. doi: 10.1080/10255842.2015. 1088009 PMID: 26406926
18. Tower TT, Tranquillo RT. Alignment maps of tissues: II. Fast harmonic analysis for imaging. Biophys J. 2001; 81(5):2964±71. doi: 10.1016/S0006-3495(01)75936-X PMID: 11606306
19. Zhang W, Ayoub S, Liao J, Sacks MS. A meso-scale layer-specific structural constitutive model of the mitral heart valve leaflets. Acta Biomater. 2016; 32:238±55. doi: 10.1016/j.actbio.2015.12.001 PMID:26712602
20. Kim DH, Provenzano PP, Smith CL, Levchenko A. Matrix nanotopography as a regulator of cell function. J Cell Biol. 2012; 197(3):351±60. doi: 10.1083/jcb.201108062 PMID: 22547406
21. Muthusubramaniam L, Peng L, Zaitseva T, Paukshto M, Martin GR, Desai TA. Collagen fibril diameter and alignment promote the quiescent keratocyte phenotype. J Biomed Mater Res A. 2012; 100 (3):613±21. doi: 10.1002/jbm.a.33284 PMID: 22213336
22. Kim DH, Seo CH, Han K, Kwon KW, Levchenko A, Suh KY. Guided Cell Migration on Microtextured Substrates with Variable Local Density and Anisotropy. Adv Funct Mater. 2009; 19(10):1579±86. doi:10.1002/adfm.200990041 PMID: 20046799
23. Kim DH, Han K, Gupta K, Kwon KW, Suh KY, Levchenko A. Mechanosensitivity of fibroblast cell shape and movement to anisotropic substratum topography gradients. Biomaterials. 2009; 30(29):5433±44.doi: 10.1016/j.biomaterials.2009.06.042 PMID: 19595452
24. Campagnola PJ, Loew LM. Second-harmonic imaging microscopy for visualizing biomolecular arrays in cells, tissues and organisms. Nat Biotechnol. 2003; 21(11):1356±60. doi: 10.1038/nbt894 PMID:14595363

25. Schneider CA, Rasband WS, Eliceiri KW. NIH Image to ImageJ: 25 years of image analysis. Nat Methods.2012; 9(7):671±5. doi: 10.1038/nmeth.2089 PMID: 22930834
26. Junqueira LC, Bignolas G, Brentani RR. Picrosirius staining plus polarization microscopy, a specific method for collagen detection in tissue sections. Histochem J. 1979; 11(4):447±55. doi: 10.1007/bf01002772 PMID: 91593
27. Schindelin J, Arganda-Carreras I, Frise E, Kaynig V, Longair M, Pietzsch T, et al. Fiji: an open-source platform for biological-image analysis. Nat Methods. 2012; 9(7):676±82. doi: 10.1038/nmeth.2019 PMID: 22743772
28. Rich L, Whittaker P. Collagen and Picrosirius Red Staining: a Polarized Light Assessment of Fibrillar Hue and Spatial Distribution. Braz J Morphol Sci. 2005; 22:97±104.
29. Chen X, Nadiarynkh O, Plotnikov S, Campagnola PJ. Second harmonic generation microscopy for quantitative analysis of collagen fibrillar structure. Nat Protoc. 2012; 7(4):654±69. doi: 10.1038/nprot.2012.009 PMID: 22402635
30. Bredfeldt JS, Liu Y, Pehlke CA, Conklin MW, Szulczewski JM, Inman DR, et al. Computational segmentation of collagen fibers from second-harmonic generation images of breast cancer. J Biomed Opt. 2014; 19(1):16007. doi: 10.1117/1.JBO.19.1.016007 PMID: 24407500
31. Stein AM, Vader DA, Jawerth LM, Weitz DA, Sander LM. An algorithm for extracting the network geometry of three-dimensional collagen gels. J Microsc. 2008; 232(3):463±75. doi: 10.1111/j.1365-2818. 2008.02141.x PMID: 19094023
32. Rodriguez-Rodriguez P, Arribas SM, De Pablo ALL, GonzaÂ lez MC, Abderrahim F, Condezo-Hoyos L. A simple dot-blot-Sirius red-based assay for collagen quantification. Analytical and Bioanalytical Chemistry. 2013; 405:6863±71. doi: 10.1007/s00216-013-7101-0 PMID: 23780225
33. Dayan D, Hiss Y, Hirshberg A, Bubis JJ, Wolman M. Are the polarization colors of picrosirius red stained collagen determined only by the diameter of the fibers? Histochemistry. 1989; 93(1):27±9. doi:10.1007/bf00266843 PMID: 2482274
34. Yip CY, Simmons CA. The aortic valve microenvironment and its role in calcific aortic valve disease.Cardiovasc Pathol. 2011; 20(3):177±82. doi:10.1016/j.carpath.2010.12.001 PMID: 21256052
35. Smith-Mungo LI, Kagan HM. Lysyl oxidase: properties, regulation and multiple functions in biology. Matrix Biol. 1998; 16(7):387±98. doi: 10.1016/s0945-053x(98)90012-9 PMID: 9524359
36. Eyre D, Shao P, Weis MA, Steinmann B. The kyphoscoliotic type of Ehlers-Danlos syndrome (type VI): differential effects on the hydroxylation of lysine in collagens I and II revealed by analysis of crosslinked telopeptides from urine. Mol Genet Metab. 2002; 76(3):211±6. doi: 10.1016/s1096-7192(02) 00036-7 PMID: 12126935
37. Chen JH, Simmons CA. Cell-matrix interactions in the pathobiology of calcific aortic valve disease: critical roles for matricellular, matricrine, and matrix mechanics cues. Circ Res. 2011; 108(12):1510±24. doi: 10.1161/CIRCRESAHA.110.234237 PMID: 21659654

38. Arjunon S, Rathan S, Jo H, Yoganathan AP. Aortic valve: Mechanical environment and mechanobiology. Annals of Biomedical Engineering. 2013; 41:1331±46. doi: 10.1007/s10439-013-0785-7 PMID:23515935
39. Bishop J. Regulation of cardiovascular collagen synthesis by mechanical load. Cardiovascular Research. 1999; 42:27±44. doi: 10.1016/s0008-6363(99)00021-8 PMID: 10434993
40. Hadi MF, Barocas VH. Microscale fiber network alignment affects macroscale failure behavior in simulated collagen tissue analogs. Journal of biomechanical engineering. 2013; 135:021026. doi: 10.1115/1.4023411 PMID: 23445071
41. Gould RA, Chin K, Santisakultarm TP, Dropkin A, Richards JM, Schaffer CB, et al. Cyclic strain anisotropy regulates valvular interstitial cell phenotype and tissue remodeling in three-dimensional culture. Acta Biomater. 2012; 8(5):1710±9. doi: 10.1016/j.actbio.2012.01.006 PMID: 22281945
42. Herchenhan A, Uhlenbrock F, Eliasson P, Weis M, Eyre D, Kadler KE, et al. Lysyl oxidase activity is required for ordered collagen fibrillogenesis by tendon cells. Journal of Biological Chemistry. 2015; 290:16440±50. doi: 10.1074/jbc.M115.641670 PMID: 25979340
43. Mouw JK, Ou G, Weaver VM. Extracellular matrix assembly: a multiscale deconstruction. Nature reviews Molecular cell biology. 2014; 15:771±85. doi: 10.1038/nrm3902 PMID: 25370693
44. Satta J, Oiva J, Salo T, Eriksen H, Ohtonen P, Biancari F, et al. Evidence for an altered balance between matrix metalloproteinase-9 and its inhibitors in calcific aortic stenosis. Ann Thorac Surg.2003; 76(3):681±8; discussion 8. doi: 10.1016/s0003-4975(03)00529-0 PMID: 12963177
45. Soini Y, Satta J, Maatta M, Autio-Harmainen H. Expression of MMP2, MMP9, MT1-MMP, TIMP1, and TIMP2 mRNA in valvular lesions of the heart. J Pathol. 2001; 194(2):225±31. doi: 10.1002/path.850 PMID: 11400152
46. Fondard O, Detaint D, Iung B, Choqueux C, Adle-Biassette H, Jarraya M, et al. Extracellular matrix remodelling in human aortic valve disease: the role of matrix metalloproteinases and their tissue inhibitors. Eur Heart J. 2005; 26(13):1333±41. doi: 10.1093/eurheartj/ehi248 PMID: 15827062
47. Stephens EH, Grande-Allen KJ. Age-related changes in collagen synthesis and turnover in porcine heart valves. J Heart Valve Dis. 2007; 16(6):672±82. PMID: 18095519
48. Wang Y, Azais T, Robin M, Vallee A, Catania C, Legriel P, et al. The predominant role of collagen in the nucleation, growth, structure and orientation of bone apatite. Nat Mater. 2012; 11(8):724±33. doi:10.1038/nmat3362 PMID: 22751179
49. Yip CYY, Chen J-H, Zhao R, Simmons Ca. Calcification by valve interstitial cells is regulated by the stiffness of the extracellular matrix. Arteriosclerosis, thrombosis, and vascular biology. 2009; 29:936± 42. doi: 10.1161/ATVBAHA.108.182394 PMID: 19304575
50. Smithmyer ME, Sawicki LA, Kloxin AM. Hydrogel scaffolds as in vitro models to study fibroblast activation in wound healing and disease. Biomater Sci. 2014; 2(5):634±50. doi: 10.1039/C3BM60319A PMID: 25379176

51. Porras AM, Hutson HN, Berger AJ, Masters KS. Engineering approaches to study fibrosis in 3-D in vitro systems. Curr Opin Biotechnol. 2016; 40:24±30. doi: 10.1016/j.copbio.2016.02.006 PMID: 26926460
52. Tilbury K, Hocker J, Wen BL, Sandbo N, Singh V, Campagnola PJ. Second harmonic generation microscopy analysis of extracellular matrix changes in human idiopathic pulmonary fibrosis. Journal of biomedical optics. 2014; 19:086014. doi: 10.1117/1.JBO.19.8.086014 PMID: 25134793
53. Pena A, Fabre A, Debarre D, Marchal-Somme J, Crestani B, Martin J, et al. Three-Dimensional Investigation and Scoring of Extracellular Matrix Remodeling During Lung Fibrosis Using Multiphoton Microscopy.Microscopy research and technique. 2007; 70:162±70. doi: 10.1002/jemt.20400 PMID: 17177275
54. Strupler M, Pena a-M, Hernest M, Tharaux P-L, Martin J-L, Beaurepaire E, et al. Second harmonic imaging and scoring of collagen in fibrotic tissues. Optics express. 2007; 15:4054±65. doi: 10.1364/oe.15.004054 PMID: 19532649
55. Bredfeldt JS, Liu Y, Conklin MW, Keely PJ, Mackie TR, Eliceiri KW. Automated quantification of aligned collagen for human breast carcinoma prognosis. J Pathol Inform. 2014; 5(1):28. doi: 10.4103/2153-3539.139707 PMID: 25250186
56. Li C, Xu S, Gotlieb AI. The progression of calcific aortic valve disease through injury, cell dysfunction, and disruptive biologic and physical force feedback loops. Cardiovascular pathology: the official journal of the Society for Cardiovascular Pathology. 2013; 22:1±8. doi: 10.1016/j.carpath.2012.06.005

CHAPTER 4: METHODS OF TISSUE PRESERVATION FOR ANALYSIS OF COLLAGEN STRUCTURE

Elements of this chapter have been submitted for publication as:
"Impact of Tissue Preservation Method on Collagen Fiber Architecture" in Biotechnic & Histochemistry

4.1 Abstract

Microarchitectural features of the extracellular matrix provide the mechanical foundation of tissue function and present topographical cues which influence cellular behaviors such as proliferation, migration, protein expression. Preservation of tissue microarchitecture is required for accurate evaluation of tissue characteristics and pathologies, but it is unclear if common preservation methods are equivalent in their abilities to conserve these structures. In the current work, we performed a quantitative analysis of collagen microarchitecture in samples that had been either flash-frozen, fixed in formalin, or preserved in RNA*later*®, and which contained both collagen-rich and collagen-sparse regions. Fibrillar collagen organization was characterized using picrosirius red staining as well as second harmonic generation (SHG) microscopy. Maintenance of collagen fiber characteristics compared to the gold standard of flash-freezing was dependent on both the method of preservation and the local collagen content of the tissue. Analysis via SHG revealed that both formalin fixation and RNA*later*® were able to maintain similar collagen fiber characteristics as flash freezing in collagen-rich areas of the tissue, but not in collagen-sparse regions. Meanwhile, analysis via picrosirius red staining indicated preservation-dependent changes in overall tissue architecture and suprafibrillar organization, but also potential incompatibility of

RNA*later*® with the picrosirius red dye for quantification of individual fiber features. Combined with considerations of cost, ease of use, storage conditions, and ability to use the preserved tissue for RNA or protein analyses, this quantitative characterization of the effect of preservation method on collagen microarchitecture can help provide further guidance to researchers in identifying the most appropriate preservation approach for their needs.

4.2 Introduction

Identification of an optimal tissue preservation approach involves a balance of many competing factors, including cost, ease of use, ease of storage, storage longevity, ability to multi-plex tissue analysis, and retention of native tissue structure and physiology. Flash-freezing (or snap-freezing) of tissues in liquid nitrogen is often deemed the “gold standard” for tissue preservation due to its ability to retain native tissue structure, while also maintaining the integrity of nucleic acids and phosphoproteins [1-4]. However, despite the benefits of flash freezing, this technique requires access to liquid nitrogen immediately following tissue isolation and continued storage of banked tissues at temperatures at or below -20°C, rendering it impractical and costly for large-scale tissue acquisition and storage [5]. Meanwhile, formalin fixation is the standard technique used for long-term tissue preservation as it overcomes many of the difficulties associated with flash-freezing while still preserving tissue morphology [6]. Formalin fixation allows for facile sample collection methods, temporary storage at room temperature, and simpler transportation between tissue isolation and storage sites [7]. However, formalin fixation is known to cause increased nucleic acid fragmentation and decreased RNA extraction

efficiency due to the creation of crosslinks [8-11]. The crosslinking of endogenous proteins in the preserved tissue occurs through the formation of methylene bridges [12, 13], thereby interfering with the integrity of phosphoproteins and necessitating the use of heat or other methods to reduce these crosslinks prior to RNA isolation or immunohistochemistry [4, 14].

RNA*later*®, an ammonium sulfate solution, is not as common in histological preparations, but has been widely used for its ability to stabilize nucleic acids in tissue samples to be used for subsequent gene expression or genomic analyses [15]. Previous studies have shown that tissues stored in RNA*later*® yield comparable [16] or even better RNA quality compared to flash-frozen tissues [17, 18]. Tissue banks have also begun adopting RNA*later*® storage protocols due to its improved ability to preserve nucleic acid integrity compared to formalin fixed samples, while yielding similar histological results [15]. The ability to use a single sample for multiple different types of analyses is desirable due to limited tissue availability creating a common and significant obstacle in the analysis of specimens from both human and animal sources [19, 20].

While the aforementioned preservation approaches have been extensively compared with respect to histological, immunohistochemical, and gene expression outcomes [1, 21], the effect of the preservation method on tissue microarchitecture has received less attention [22]. There is an increasing appreciation of the importance of collagen fiber architecture in determining cell behavior [23, 24], disease progression [25], and mechanical properties [26, 27], motivating the need to faithfully retain these structures

during sample preservation to allow accurate analysis of tissue pathobiology [23, 28]. In this study, we applied histological staining techniques and second harmonic generation (SHG) imaging to evaluate how different preservation conditions altered the collagen fiber architecture of two model tissues: one that exhibits distinct high-density and low-density collagen areas within the same native tissue structure and one that exhibits a high degree of collagen crimping. Specifically, we examined and quantified the collagen fiber structure of porcine aortic heart valves, which exhibit a distinct trilaminar architecture composed of a region of high collagen content and alignment (fibrosa), a region of low collagen content and high glycosaminoglycan content (spongiosa), and a region of significant elastin content (ventricularis) [29, 30]. The thin nature of the valve also ensures quick and complete penetration of preservation solutions, minimizing issues that may arise from differences in diffusion of the solutions through the tissue [12]. We also analyzed collagen architecture in rat tail tendon fascicles, which have a highly dense and crimped collagen structure and are often used as a standard in SHG imaging [31-33]. In this work, we sought to quantitatively characterize the effect of preservation method on collagen microarchitecture. Combined with existing observations on the limitations and advantages of these preservation techniques, it is hoped that this information can help provide further guidance to researchers in identifying the most appropriate preservation approach for their needs.

4.3 Materials and Methods

All materials were purchased from Sigma Aldrich unless otherwise noted.

4.3.1 Tissue Acquisition and Preservation

Aortic heart valves were isolated from porcine hearts obtained from a local butcher (Hoesly's Meats, New Glarus, WI) from pigs between 5 and 6 months of age. Rat tails were collected from rats undergoing euthanasia for other studies, and tendon fascicles were removed. Valve leaflets and rat tail tendon fascicles (RTTfs) were isolated within 4 hours of animal slaughter and washed in 1X phosphate buffered saline (PBS) before being preserved via three different methods. "Frozen" denotes tissues that were flash-frozen in liquid nitrogen and stored at -20ºC until being embedded in paraffin. The other two preservation methods involved treatment with exogenous chemicals, where "Formalin" refers to tissues placed in 10% neutral buffered formalin for a minimum of 24 hours and "RNA*later*®" refers to tissues preserved by immersion in RNA*later*® for a minimum of 24 hours. Tissues preserved in formalin or RNA*later*® were stored at -20ºC in their respective preservation solutions until being embedded in paraffin.

4.3.2 Histological Staining

Tissues were washed in fresh 1X PBS and either flash frozen using liquid nitrogen, stored in 10% Formalin, or stored in RNA*later*® before being prepared for staining. Fascicles were cut to length and washed prior to histological staining. Heart valve leaflets were paraffin-embedded and cut into 5 μm thick sections; these sections were then deparaffinized and rehydrated prior to staining with picrosirius red to visualize collagen, as previously described [34]. Briefly, tissue sections were first stained using 0.1 % (w/v) Direct Red 80 in saturated aqueous picric acid solution for one hour. Excess stain solution was removed before tissues were washed twice in acidified water,

dehydrated in graded washes of ethanol and xylene, and mounted in Permount. Tissue sections were imaged on an Olympus BX60 upright microscope with a DP25 camera using CellSens Standard software (V1.13) for both bright field and linearly polarized birefringence. The birefringence of three areas of equal dimensions per tissue layer per image was measured using FIJI (open source, version 2.0.0-rc-43/1.5e). The birefringence of each region of interest was analyzed using a previously described method [35] to quantify the percentage of tissue area exhibiting birefringence and the distribution of birefringence color. Tissue width and crimp period were analyzed in RTTfs, as these are standard measurements for these tissues [33]. Width was measured at 5 places per image along the fascicle. Crimp period was measured as the distance between spots of minimum birefringence along the length of the RTTfs. The crimp period was measured at 5 places in each image and averaged per image for analysis.

4.3.3 Second Harmonic Generation Imaging and Collagen Fiber Analysis

Paraffin-embedded valve tissues were cut into 13-15 μm thick sections in preparation for detection of collagen via second harmonic generation (SHG) imaging. Deparaffinized tissues were rehydrated before being mounted with coverslips and sealed with lacquer. Fascicles were cut to length and washed before being mounted and sealed. Prepared sections were stored at 4ºC and imaged within 2 weeks. SHG imaging was conducted using a mode-locked 890 nm laser, and SHG was measured using a 445/20 nm filter along with a 40x water-immersion objective (working distance 3 mm, 0.8 NA) on an Olympus BX61 upright microscope (Olympus, Tokyo, Japan) using an Olympus

Fluoview 300 scanning system at 2x digital zoom. Analysis of fiber characteristics in valve leaflets was conducted on three sections tissue, in three distinct areas of each section. SHG was collected through the entire depth of the tissue section at a step size of 1 μm and the five middle images were averaged together for analysis. SHG was not collected from the ventricularis layer of the valve leaflets, as the organization of the fibers within that layer are perpendicular to the field of view, and the layer is too thin to capture via *en face* sectioning. Analysis of RTTfs fiber characteristics was conducted similarly to analysis of valve leaflets, with SHG collected through the entire depth of three distinct fascicles, in three distinct areas of each fascicle. Quantification of fiber characteristics was performed using ctFIRE V2 Beta and CurveAlign V4.0 Beta, which are both open source software developed by the Laboratory for Optical and Computational Instrumentation (LOCI) at the University of Wisconsin-Madison. SHG images in 8-bit tiff format were imported into the program where they underwent curvelet transform (CT) reconstruction through the use of CurveLab 2.1.2 (April 2008) followed by creation of fiber overlays via the FIRE algorithm. The fiber outputs from ctFIRE then underwent feature analysis through CurveAlign for output of final fiber features. Matlab (The MathWorks, Inc., Natick, MA) was used as the platform to run the ctFIRE and CurveAlign software. Data from selected fibers were then exported from CurveAlign into Excel (Microsoft, Redmond, WA) to undergo statistical analysis. Quantification of multiple fiber characteristics was performed using this method, and reported using the following definitions: “Fiber width” is a measurement of the width at multiple points along the fiber within the image. “Distance to nearest x”, where x is either 2, 4, 8, or 16 fibers, is the distance in microns between the nearest x fibers from multiple

points along the length of the reference fiber. “Box density” is a measurement of the average number of fibers within a region of specified size. “Fiber angle” denotes the average angle of fibers within an image relative to each other. “Alignment of nearest x”, where x is either 2, 4, 8, or 16 fibers, is a measurement of the alignment of the nearest x fibers relative to a reference fiber where 0 indicates no alignment, or the fibers are perpendicular, and 1 indicates complete alignment, where the fibers are parallel. “Box alignment” is a measurement of the alignment of all fibers within an area of specified size, with 0 indicating no alignment and 1 indicating complete alignment of fibers within the region.

4.3.4 Statistics

Statistical analysis of data from SHG imaging was completed in Prism 6 (Graphpad Software, Inc., La Jolla CA) using a one-way ANOVA and Tukey’s post-hoc test. Statistical significance of all other groups was analyzed using a two-tailed, unpaired t-test assuming equal variance. Values of $p<0.05$ were considered significant. All tests were n = 3 unless otherwise noted.

4.4 Results

4.4.1 Assessment of Collagen Architecture via Picrosirius Red Birefringence

The impact of tissue preservation technique on collagen organization was first examined using polarized light imaging of heart valve leaflet sections stained with picrosirius red. This approach provides semi-quantitative information about both the fraction of tissue that is composed of fibrillar collagen (*i.e.*, percentage of total tissue

area that exhibits birefringence) as well as the diameter of the fibers. Figure 4.1A shows bright-field images of leaflet sections stained with picrosirius red, where areas of fibrillar collagen are indicated by red staining. Corresponding images of picrosirius red birefringence are shown in Figure 4.1B, where fiber diameter is indicated by the color of birefringence (thin fibers appear green, with yellow, orange, and red indicating increasing thickness). As expected in a normal aortic valve leaflet, the fibrosa was dense with collagen, while the spongiosa (middle) was more sparsely populated with collagen fibers. The percentage of total area exhibiting birefringence within the fibrosa was not statistically different across the three preservation methods (Figure 4.2A). In the

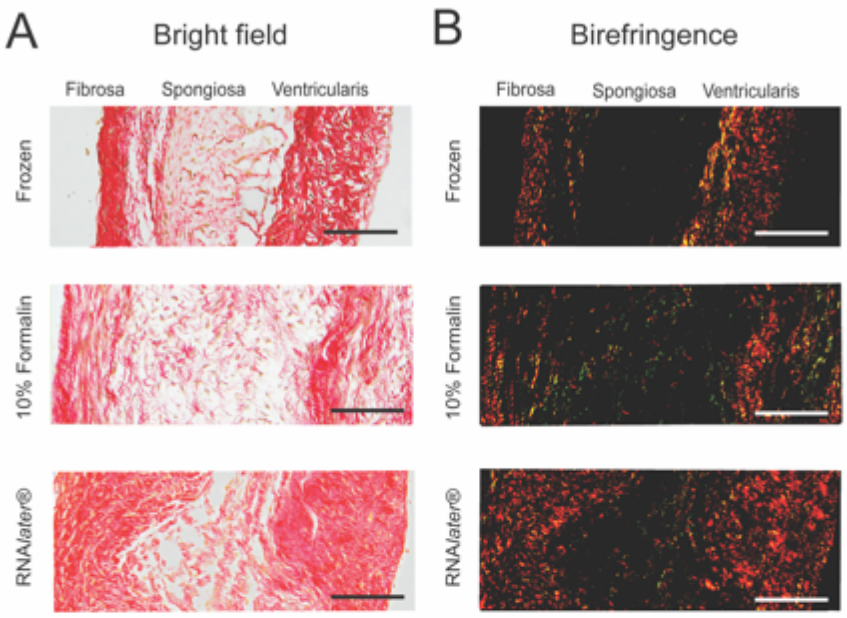

Figure 4.1 Collagen Visualization in Valve Leaflets via Picrosirius Red Staining Images of aortic valve leaflets stained with picrosirius red taken using brightfield or polarized light (birefringence). Samples had been preserved using flash-freezing, formalin, or RNA*later*®. Scale bar = 50 μm.

spongiosa, the fraction of tissue composed of fibrillar collagen was also similar across all the preservation methods. As expected, the collagen content within the spongiosa was generally lower than that observed in the fibrosa (Figure 4.2B).

Leaflet sections stained with picrosirius red were also analyzed to determine the percentage of total birefringence represented by each hue (green, yellow, orange, or red). The amount of red birefringence in the fibrosa did not differ across tissues that had been fixed in formalin vs. those that had been flash-frozen ($p=0.08$), but the fibrosa of tissues preserved in RNA*later*® did have a significantly lower amount of red birefringence compared to both frozen and formalin-fixed tissues ($p=0.017$ and $p=0.049$, respectively; Figure 4.2C). The amount of orange birefringence in the fibrosa of tissues preserved in RNA*later*® was similar to that observed in frozen tissues, but was significantly higher ($p=0.0010$) compared to the orange birefringence in the fibrosa of tissues preserved in formalin. Analysis of each hue as a percentage of total birefringence in the spongiosa (Figure 4.2D) revealed similar findings, with preservation in RNA*later*® associated with decreased red and orange birefringence compared to frozen tissues ($p=0.0016$ and $p=0.00036$ for red and orange, respectively) and formalin-fixed tissues ($p=0.041$ and $p=0.013$, respectively). No significant differences were observed between formalin-fixed and frozen tissues in any birefringence analysis.

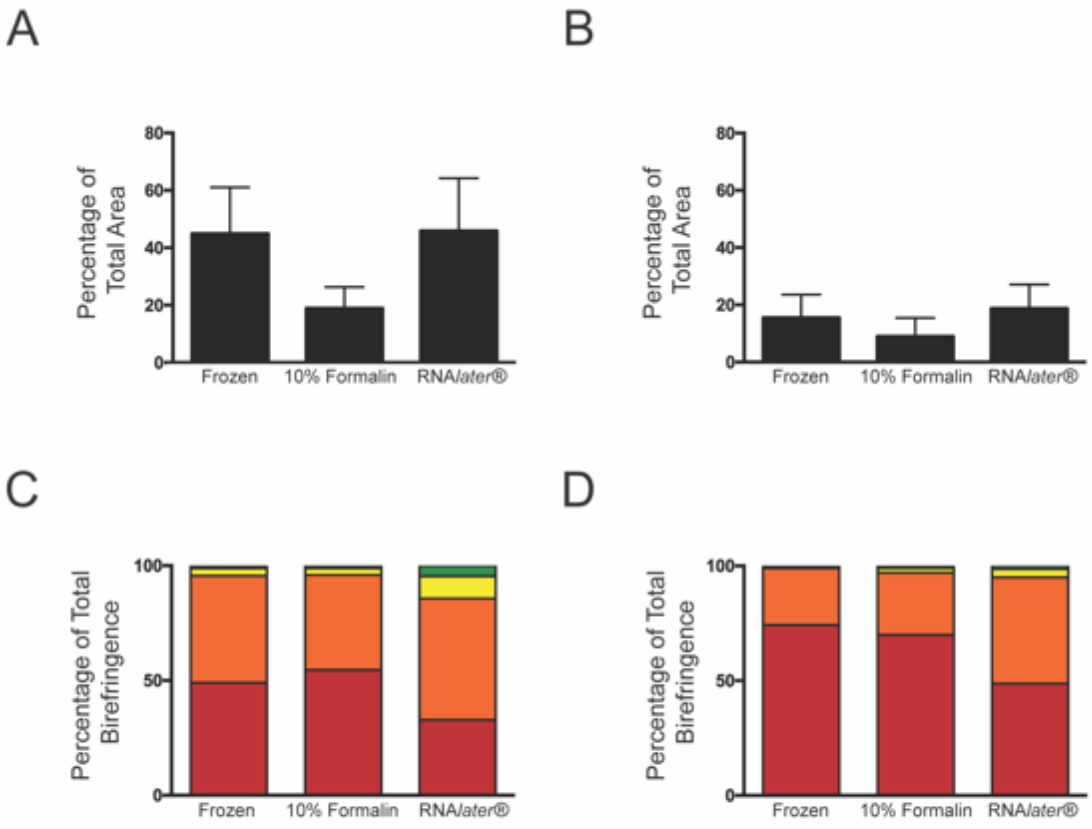

Figure 4.2 Quantification of Picrosirius Red Birefringence in Valve Leaflets Quantification of birefringence measured in aortic valve leaflets stained with picrosirius red, showing birefringence as a measure of total area within the fibrosa (A) and spongiosa (B). Color of birefringence as a percentage of total birefringence in the fibrosa (C) and spongiosa (D). Red refers to red birefringence (bottom), followed by orange, yellow, and green.

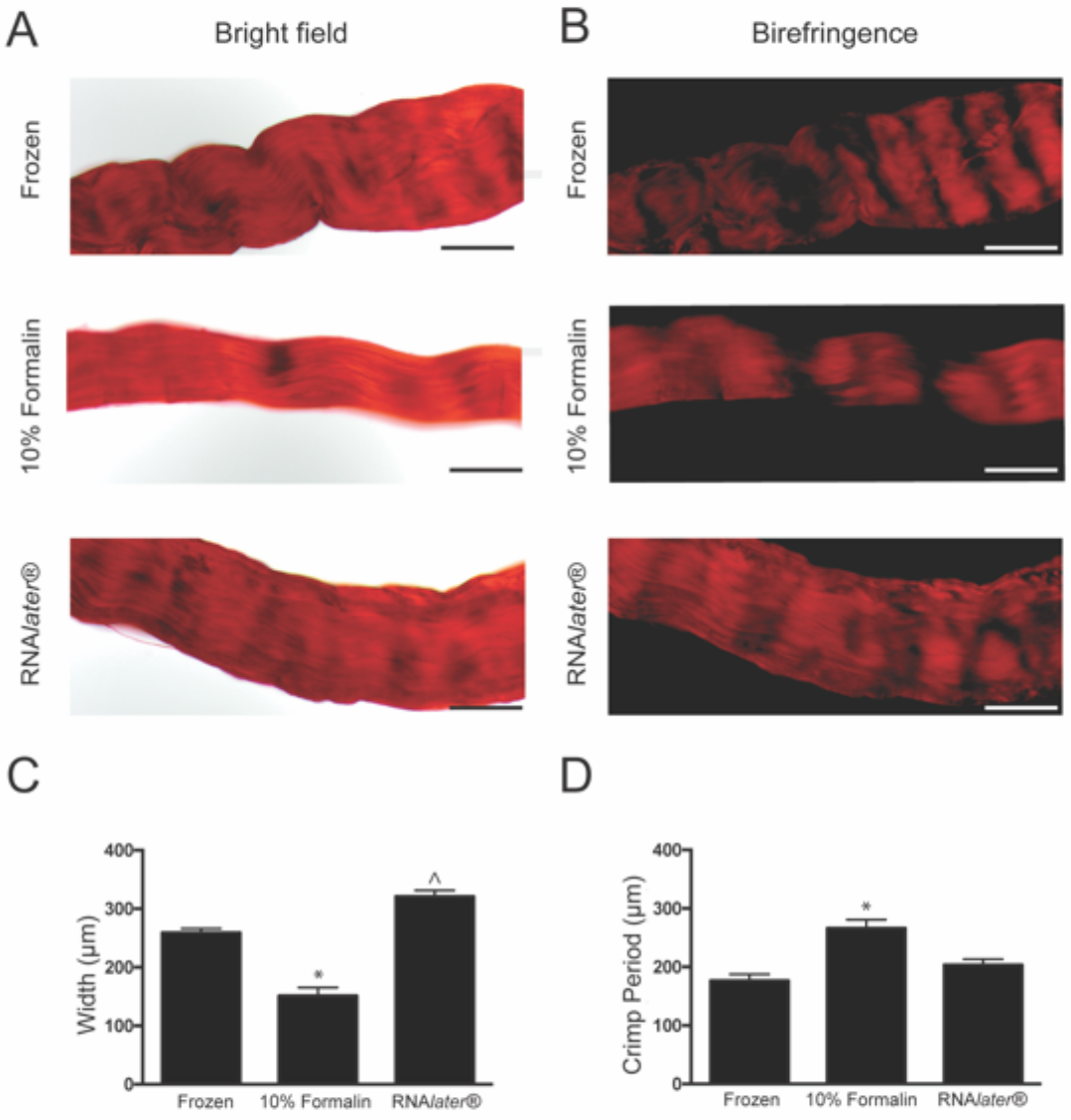

Figure 4.3 Visualization and Quantification of Collagen Crimp and Fascicle Width in RTTfs Images of RTTfs stained with picrosirius red obtained using brightfield (A) or polarized light (B). Scale bar = 200 µm. Quantification of RTTf width (C) and period of collagen crimp (D). *p < 0.05 compared to flash-frozen. ^p < 0.05 compared to formalin. Samples had been preserved using flash freezing, formalin, or RNA*later*®.

To investigate the impact of preservation methods on characteristics related to rat tendon fascicle functions such as contraction, fascicles stained with picrosirius red were

analyzed for crimp period and fascicle width (Figure 4.3) [36]. Analysis of RTTf widths revealed a significant difference across preservation techniques (Figure 4.3C), with formalin fixation resulting in decreased width compared to frozen RTTfs ($p=0.030$), which is consistent with previous observations [33]. Fascicles preserved in RNAlater® had a similar width as tissues that had been flash frozen, but were significantly wider compared to formalin fixed fascicles ($p=0.010$), Fascicles preserved in formalin had a significantly longer crimp period compared to frozen tissues ($p=0.014$), but fascicles preserved in RNA*later*® did not significantly differ in crimp period relative to RTTfs that were flash frozen or preserved in formalin ($p=0.073$ and $p=0.19$, respectively; Figure 4.3D).

4.4.2 Assessment of Collagen Architecture via Second Harmonic Generation Imaging

Picrosirius red birefringence provided information about collagen localization and organization in the preserved tissues, and some insight into the suprafibrillar architecture of RTTFs (*e.g.*, crimping). However, further analysis of individual fiber characteristics was necessary to understand the impact of the preservation methods on collagen architecture. Thus, SHG imaging of valve leaflet sections (Figure 4.4) and RTTfs (Figure 4.5) was conducted to determine whether the preservation method affected the characteristics of individual collagen fibers and their organization relative to neighboring fibers.

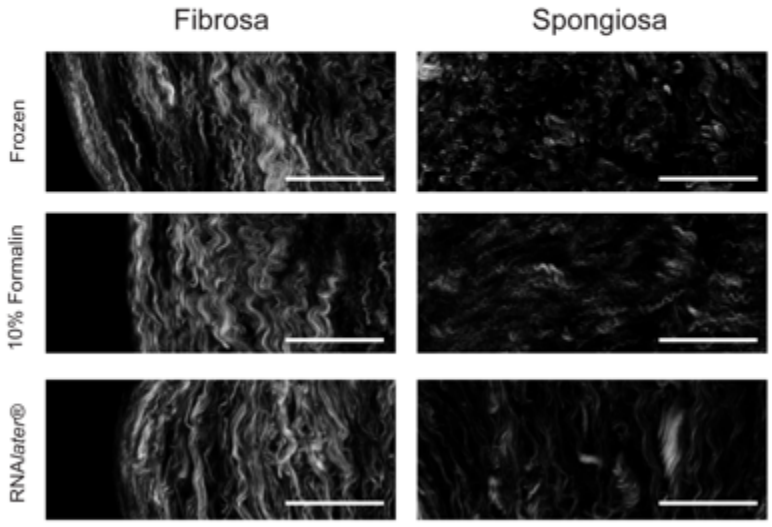

Figure 4.5 Collagen Visualization in Valve Leaflets via Second Harmonic Generation Imaging Images of the fibrosa and spongiosa of aortic valve leaflets acquired using SHG imaging. Samples had been preserved using flash freezing, formalin, or RNA*later*®. Scale bar = 50 μm

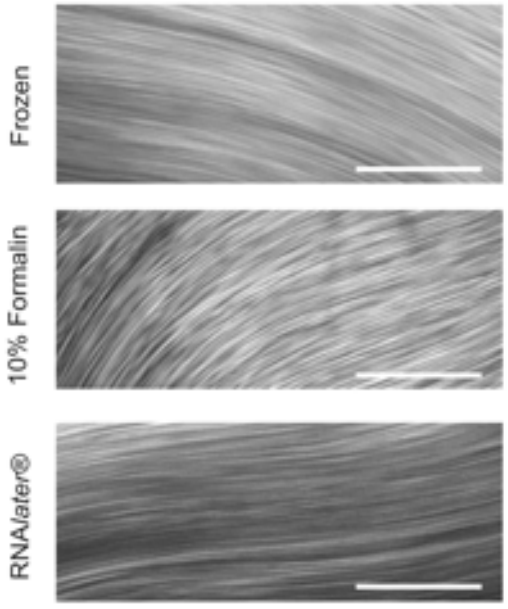

Figure 4.4 Collagen Visualization in RTTfs via Second Harmonic Generation Imaging Images of the collagen fibers in RTTfs acquired using SHG imaging. Samples had been preserved using flash freezing, formalin, or RNA*later*®. Scale bar = 50 μm.

SHG exploits the ability of fibrillar collagen to generate a second harmonic wave (at 445 nm), providing detailed micro-level structural information in the absence of any staining or chemical treatment.

In the collagen-dense fibrosa layer of the leaflet, SHG analysis yielded consistent values for virtually all measured fiber characteristics - fiber width, density, and alignment across all three preservation techniques (Table 4.1). Meanwhile, some preservation dependent variation in fiber characteristics was observed in the spongiosa, the collagen-sparse layer of the valve leaflet. While fiber width in the spongiosa was consistent across all preservation methods, fixation in formalin was associated with an increase in distance between individual fibers compared to flash-frozen samples. However, the overall fiber density across larger tissue areas remained similar for all preservation methods.

Table 4.1 Collagen Fiber Architecture in the Heart Valve Leaflet Fibrosa

MEASUREMENT	FROZEN AVERAGE	10% FORMALIN AVERAGE	RNA*later*® AVERAGE
FIBER DIMENSIONS			
Fiber Width (μm)	1.91 ± 0.0177	1.91 ± 0.0985	1.89 ± 0.0217
FIBER DENSITY			
Distance to Nearest 2	6.24 ± 0.517	6.65 ± 1.88	6.06 ± 0.261
Distance to Nearest 4	8.75 ± 0.760	9.57 ± 2.87	8.53 ± 0.541
Distance to Nearest 8	13.3 ± 1.54	14.7 ± 3.73	12.9 ± 1.02
Distance to Nearest 16	20.8 ± 2.96	22.8 ± 5.36	20.2 ± 1.42
Box Density 11.25 μm x 11.25 μm	2.83 ± 0.224	2.66 ± 0.368	2.79 ± 0.153
Box Density 22.5 μm x 22.5 μm	6.07 ± 0.951	5.18 ± 0.890	5.91 ± 0.831
Box Density 45 μm x 45 μm	14.0 ± 2.12	12.4 ± 2.29	13.4 ± 1.83

FIBER ALIGNMENT			
Fiber Absolute Angle (°)	77.6 ± 6.17	95.6 ± 7.50[a]	54.3 ± 5.38[a]
Alignment of Nearest 2	0.952 ± 0.0449	0.960 ± 0.0293	0.983 ± 0.00519
Alignment of Nearest 4	0.922 ± 0.0648	0.927 ± 0.0578	0.969 ± 0.0105
Alignment of Nearest 8	0.887 ± 0.104	0.904 ± 0.0623	0.957 ± 0.00943
Alignment of Nearest 16	0.835 ± 0.182	0.892 ± 0.0820	0.937 ± 0.0242
Box Alignment 11.25 μm x 11.25 μm	0.987 ± 0.0100	0.990 ± 0.00436	0.992 ± 0.00273
Box Alignment 22.5 μm x 22.5 μm	0.965 ± 0.0230	0.959 ± 0.0221	0.980 ± 0.00869
Box Alignment 45 μm x 45 μm	0.911 ± 0.0847	0.925 ± 0.0517	0.959 ± 0.00475

[a] = $p<0.5$ compared to flash freezing, [b] = $p<0.5$ compared to formalin fixation.

In collagen-sparse regions, fiber alignment was the property most consistently altered by preservation method, as both RNA*later*® and formalin yielded lower alignment values compared to the flash-frozen condition (Table 4.2).

Table 4.2 Collagen Fiber Architecture in the Heart Valve Leaflet Spongiosa

MEASUREMENT	FROZEN AVERAGE	10% FORMALIN AVERAGE	RNA*later*® AVERAGE
FIBER DIMENSIONS			
Fiber Width (μm)	1.89 ± 0.118	1.85 ± 0.0597	1.87 ± 0.0336
FIBER DENSITY			
Distance to Nearest 2	7.86 ± 0.282	9.62 ± 0.773[a]	8.40 ± 0.370
Distance to Nearest 4	12.3 ± 0.600	16.1 ± 1.33[a]	13.0 ± 0.416[b]
Distance to Nearest 8	18.9 ± 1.13	25.4 ± 3.08[a]	20.3 ± 1.13
Distance to Nearest 16	29.9 ± 1.48	43.0 ± 6.74[a]	33.1 ± 3.10
Box Density 11.25 μm x 11.25 μm	2.55 ± 0.0910	2.52 ± 0.0687	2.42 ± 0.251
Box Density 22.5 μm x 22.5 μm	4.53 ± 0.364	4.24 ± 0.291	4.33 ± 0.661
Box Density 45 μm x 45 μm	8.80 ± 0.269	8.00 ± 0.572	8.02 ± 0.962
FIBER ALIGNMENT			
Fiber Absolute Angle (°)	75.2 ± 8.07	92.4 ± 9.72	57.6 ± 7.10[b]
Alignment of Nearest 2	0.945 ± 0.0123	0.896 ± 0.0508	0.918 ± 0.00602[a]
Alignment of Nearest 4	0.898 ± 0.00985	0.804 ± 0.0450[a]	0.864 ± 0.0185[a,b]
Alignment of Nearest 8	0.864 ± 0.00993	0.671 ± 0.0260[a]	0.805 ± 0.0237[a,b]
Alignment of Nearest 16	0.806 ± 0.0237	0.601 ± 0.0417[a]	0.764 ± 0.0379[a,b]

Box Alignment 11.25 μm x 11.25 μm	0.989 ± 0.00707	0.966 ± 0.0190	0.977 ± 0.00734
Box Alignment 22.5 μm x 22.5 μm	0.953 ± 0.0189	0.889 ± 0.0203[a]	0.934 ± 0.0309[b]
Box Alignment 45 μm x 45 μm	0.907 ± 0.0158	0.790 ± 0.0317[a]	0.850 ± 0.0196[a]

[a] = $p<0.05$ compared to flash freezing, [b] = $p<0.05$ compared to formalin fixation.

SHG analysis of collagen fibers was also conducted on RTTfs. Despite the preservation-dependent differences in fascicle width and crimp period noted in picrosirius red analysis, no significant differences between were identified in fiber width, density, or alignment measurements between any storage methods according to analysis of SHG images (Table 4.3).

Table 4.3 Collagen Fiber Architecture in Rat Tail Tendons

MEASUREMENT	FROZEN AVERAGE	10% FORMALIN AVERAGE	RNA*later*® AVERAGE
FIBER DIMENSIONS			
Fiber Width (μm)	1.55 ± 0.0655	1.67 ± 0.0808	1.55 ± 0.0654
FIBER DENSITY			
Distance to Nearest 2	7.50 ± 1.51	6.86 ± 1.58	6.84 ± 0.427
Distance to Nearest 4	11.7 ± 2.58	9.72 ± 2.21	9.69 ± 0.705
Distance to Nearest 8	28.3 ± 5.60	23.1 ± 9.74	22.0 ± 1.58
Box Density 11.25 μm x 11.25 μm	2.56 ± 0.265	2.85 ± 0.429	2.84 ± 0.436
Box Density 22.5 μm x 22.5 μm	4.29 ± 0.413	5.71 ± 1.36	5.82 ± 1.31
Box Density 45 μm x 45 μm	8.63 ± 1.88	14.5 ± 5.33	15.5 ± 3.67
FIBER ALIGNMENT			
Fiber Absolute Angle (°)	85.6 ± 62.9	58.0 ± 71.9	36.6 ± 15.1
Alignment of Nearest 2	$0.999 \pm 9.05\times10^{-4}$	0.997 ± 0.00335	0.997 ± 0.00127
Alignment of Nearest 4	0.997 ± 0.00152	0.996 ± 0.00222	0.994 ± 0.00259
Box Alignment 11.25 μm x 11.25 μm	$1.00 \pm 6.44\times10^{-5}$	$0.999 \pm 8.73\times10^{-4}$	$1.00 \pm 1.44\times10^{-4}$
Box Alignment 22.5 μm x 22.5 μm	$1.00 \pm 1.59\times10^{-4}$	1.00 ± 0.00120	1.00 ± 0.000187
Box Alignment 45 μm x 45 μm	$0.998 \pm 8.29\times10^{-4}$	0.996 ± 0.00249	0.996 ± 0.00260

[a] = $p<0.05$ compared to flash freezing, [b] = $p<0.05$ compared to formalin fixation.

4.5 Discussion

Microarchitectural features of the extracellular matrix (ECM) provide topographical cues that exert a profound influence on numerous cellular behaviors, including protein expression, proliferation, differentiation, and migration [25, 37, 38]. As the most abundant ECM component in the body, fibrillar collagen is the dominant microstructural element in many tissues, and changes in collagen fiber features can act as important indicators of tissue health or even disease prognosis. For example, hypertrophic cardiomyopathy is associated with a significant increase in collagen fiber size [39], while alignment of collagen fibers is thought to be a predictor of breast tumor metastasis and patient survival [40, 41]. Thus, to enable accurate investigations of tissue function and pathology, it is critical to ensure that tissue preparation faithfully preserves these microstructural features. In the current work, we found that both formalin and RNA*later*® were able to maintain the collagen fiber architecture found in collagen-dense areas of flash-frozen tissues, as evaluated by SHG imaging. However, preservation method did impact some measures of fiber arrangement in collagen-sparse areas of tissues. Additionally, our findings suggest a potential weakness in the compatibility of RNA*later*® with analysis of birefringent properties of fibers stained with picrosirius red. Overall, this information may be combined with consideration of cost, ease of use, storage conditions, and ability to use the preserved tissue for RNA or protein analyses to help guide investigators in their selection of preservation methods appropriate for their specific needs.

Analysis of collagen architecture through both histological and advanced imaging techniques illustrated preservation of the trilayer structure of the aortic heart valve. Heart valve leaflets and RTTfs preserved in either RNA*later*® or formalin generally exhibited similar tissue morphology as frozen tissues. However, birefringence hue distribution was altered by preservation in RNA*later*® relative to either flash-frozen or formalin-fixed tissues. Birefringence measured through this technique results from multiple interactions of the dye with the collagen, so the significant difference in the amount of red and orange birefringence observed with RNA*later*® preservation could indicate a shift in fiber density or width [34, 42]. It is also possible for alterations in birefringence signal intensity to occur due to unintentional fixation of tissue by alcohol during the tissue embedding process [43]. This alcohol fixation would result in frozen tissues and tissues preserved in RNA*later*®, both of which are not fixation methods, to have differences in birefringence compared to tissues that had undergone formalin fixation prior to processing [44, 45]. These uncertainties helped to motivate the use of SHG to perform a quantitative analysis of collagen fiber architecture across the different tissue preservation methods.

Analysis of the collagen microarchitecture via SHG demonstrated that all three storage methods were equivalent in their ability to preserve the width of collagen fibers throughout collagen-rich and collagen-sparse areas. Compared to frozen tissues, both RNA*later*® and formalin preservation were also able to preserve the density and alignment of collagen fibers in collagen-rich areas. This observation is consistent with previous work that compared fibrillar collagen organization across flash-frozen and

formalin-fixed tissues [46, 47], although this prior work did not include RNA*later*®, and was limited to only qualitative observations of ECM structure. However, in collagen-sparse areas, many measures of alignment were significantly lower for tissues preserved in RNA*later*® or formalin in comparison to flash-frozen. This difference was not observed for RTTfs preserved in formalin or RNA*later*®, suggesting that the effects of preservation method on alignment may be specific to local collagen sparseness. Additionally, the differences in collagen fiber density and/or width implied by the birefringent hue analysis of tissues preserved in RNA*later*® vs. flash-frozen were not borne out by the more precise fiber analysis via SHG. This finding raises the possibility of interactions between RNA*later*® and the picrosirius dye causing an altered signal.

While this study provides valuable information on the preservation of the extracellular matrix structure through both histological and advanced imaging techniques, it focused solely on fibrillar collagen architecture, and thus did not address other ECM components. Although our findings indicate little impact of preservation method on collagen fiber measurements, it is possible that preservation method could impact the nano- or micro-scale architecture of other ECM components. This study also did not investigate the ability of these storage methods to preserve nucleic acids or phosphoproteins due to the fact that this outcome has been described in detail in previous studies [15].

Compared to the standard of flash-freezing, tissue preservation in either RNA*later*® or formalin was able to conserve native tissue microarchitecture with relatively equal

success. Therefore, any of the storage methods discussed in this study could be used to preserve the microarchitectural features of the extracellular matrix, and thus are valuable methods for storing tissues for the purpose of investigating architectural characteristics that occur in a variety of diseases. Overall, by combining many of the advantages of formalin fixation (*e.g.*, ease of use and handling) with those of flash-freezing (*e.g.*, nucleic acid preservation) [18], while also preserving equivalent architecture, RNA*later*® may offer improved versatility compared to other common methods (Table 4.4). This conclusion is supportive of a previous suggestion to use RNA*later*® as an alternative to formalin for tissue banking [15]. Our findings also indicate that samples preserved via different methods (*e.g.*, formalin and RNA*later*®) should not be mixed when performing histological analyses; while neither formalin nor RNA*later*® introduced significant deviation from flash-freezing in terms of fiber architecture in collagen-rich areas, they did exhibit differences in areas of sparse collagen.

Table 4.4 Comparison of common preservation methods

APPLICATION	FROZEN	10% FORMALIN	RNA*later*®
Nucleic Acid Quality[2, 3, 16-18, 48-50]	+	-*	++
Antigen Quality [4, 51-54]	++	-*	+
Mass Spectroscopy [16, 48]	++	+	++
Cost of Storage [2, 12, 17, 18]	$$$	$	$$
Histological Morphology [3, 13, 50, 54]	+	++	+/-
Collagen Microarchitecture	++	++	++
Cellular Morphology [51, 54]	+	++	+

* requires additional processing

4.6 References

1. Beckstead, J.H., *A simple technique for preservation of fixation-sensitive antigens in paraffin-embedded tissues.* Journal of Histochemistry and Cytochemistry, 1994. **42**: p. 1127-1134.
2. Kashofer, K., et al., *Quality Control of RNA Preservation and Extraction from Paraffin-Embedded Tissue: Implications for RT-PCR and Microarray Analysis.* PLoS ONE, 2013. **8**.
3. Staff, S., et al., *Preservation of nucleic acids and tissue morphology in paraffin-embedded clinical samples: comparison of five molecular fixatives.* Journal of clinical pathology, 2013. **66**: p. 807-10.
4. Mueller, C., et al., *One-step preservation of phosphoproteins and tissue morphology at room temperature for diagnostic and research specimens.* PLoS ONE, 2011. **6**.
5. Cox, M.L., et al., *Assessment of fixatives, fixation, and tissue processing on morphology and RNA integrity.* Experimental and Molecular Pathology, 2006. **80**: p. 183-191.
6. Dotti, I., et al., *Effects of formalin, methacarn, and fineFIX fixatives on RNA preservation.* Diagnostic Molecular Pathology, 2010. **19**: p. 112-122.
7. Bussolati, G., et al., *Formalin fixation at low temperature better preserves nucleic acid integrity.* PLoS ONE, 2011. **6**.
8. Williams, C., et al., *A high frequency of sequence alterations is due to formalin fixation of archival specimens.* The American journal of pathology, 1999. **155**: p. 1467-1471.
9. David, L.E., et al., *The effect of formaldehyde fixation on RNA: Optimization of formaldehyde adduct removal.* Journal of Molecular Diagnostics, 2011. **13**: p. 282-288.
10. Cronin, M., et al., *Measurement of Gene Expression in Archival Paraffin-Embedded Tissues: Development and Performance of a 92-Gene Reverse Transcriptase-Polymerase Chain Reaction Assay.* The American Journal of Pathology, 2004. **164**: p. 35-42.
11. von Ahlfen, S., et al., *Determinants of RNA quality from FFPE samples.* PLoS ONE, 2007. **2**: p. 1-7.
12. Buesa, R.J., *Histology without formalin?* Annals of Diagnostic Pathology, 2008. **12**: p. 387-396.
13. Howat, W.J. and B.A. Wilson, *Tissue fixation and the effect of molecular fixatives on downstream staining procedures.* Methods, 2014. **70**: p. 12-19.
14. Neumeister, V.M., *Tools to assess tissue quality.* Clinical Biochemistry, 2014. **47**: p. 280-287.
15. Florell, S.R., et al., *Preservation of RNA for functional genomic studies: a multidisciplinary tumor bank protocol.* Modern Pathology, 2001. **14**: p. 116-128.

16. Bennike, T.B., et al., *Proteome stability analysis of snap frozen, RNAlater preserved, and formalin-fixed paraffin-embedded human colon mucosal biopsies.* Data in Brief, 2016. **6**: p. 942-947.
17. Hatzis, C., et al., *Effects of tissue handling on rna integrity and microarray measurements from resected breast cancers.* Journal of the National Cancer Institute, 2010. **103**: p. 1871-1883.
18. Sherker, A.R., et al., *Optimal preservation of liver biopsy samples for downstream translational applications.* Hepatology International, 2013. **7**: p. 758-766.
19. Gugic, D., et al., *Novel tissue preservative and tissue fixative for comparative pathology and animal research.* Journal of Experimental Animal Science, 2007. **43**: p. 271-281.
20. Lin, J., et al., *High-quality genomic DNA extraction from formalin-fixed and paraffin-embedded samples deparaffinized using mineral oil.* Analytical Biochemistry, 2009. **395**: p. 265-267.
21. Su, J.M.F., et al., *Comparison of ethanol versus formalin fixation on preservation of histology and RNA in laser capture microdissected brain tissues.* Brain Pathology, 2004. **14**: p. 175-182.
22. Schenke-Layland, K., et al., *Optimized Preservation of Extracellular Matrix in Cardiac Tissues: Implications for Long-Term Graft Durability.* Annals of Thoracic Surgery, 2007. **83**: p. 1641-1650.
23. Fraley, S.I., et al., *Three-dimensional matrix fiber alignment modulates cell migration and MT1-MMP utility by spatially and temporally directing protrusions.* Scientific reports, 2015. **5**: p. 14580.
24. Muthusubramaniam, L., et al., *Collagen fibril diameter and alignment promote the quiescent keratocyte phenotype.* Journal of biomedical materials research. Part A, 2012. **100**: p. 613-21.
25. Provenzano, P.P., et al., *Collagen density promotes mammary tumor initiation and progression.* BMC medicine, 2008. **6**: p. 11.
26. Sacks, M.S., D.B. Smith, and E.D. Hiester, *The aortic valve microstructure: Effects of transvalvular pressure.* Journal of Biomedical Materials Research, 1998. **41**: p. 131-141.
27. Hadi, M.F. and V.H. Barocas, *Microscale fiber network alignment affects macroscale failure behavior in simulated collagen tissue analogs.* Journal of biomechanical engineering, 2013. **135**: p. 021026.
28. Lee, C.H., et al., *Nanofiber alignment and direction of mechanical strain affect the ECM production of human ACL fibroblast.* Biomaterials, 2005. **26**: p. 1261-1270.
29. Stella, J.a. and M.S. Sacks, *On the biaxial mechanical properties of the layers of the aortic valve leaflet.* Journal of biomechanical engineering, 2007. **129**: p. 757-766.
30. Schoen, F.J. and A.I. Gotlieb, *Heart valve health, disease, replacement, and repair: A 25-year cardiovascular pathology perspective.* Cardiovascular Pathology, 2016. **25**: p. 341-352.

31. Campagnola, P.J. and L.M. Loew, *Second-harmonic imaging microscopy for visualizing biomolecular arrays in cells, tissues and organisms.* Nature biotechnology, 2003. **21**: p. 1356-60.
32. Freund, I., M. Deutsch, and A. Sprecher, *Connective tissue polarity. Optical second-harmonic microscopy, crossed-beam summation, and small-angle scattering in rat-tail tendon.* Biophysical Journal, 1986. **50**: p. 693-712.
33. Williams, R.M., W.R. Zipfel, and W.W. Webb, *Interpreting second-harmonic generation images of collagen I fibrils.* Biophysical Journal, 2005. **88**: p. 1377-1386.
34. Dayan, D., et al., *Are the polarization colors of picrosirius red-stained collagen determined only by the diameter of the fibers?* Histochemistry, 1989. **93**: p. 27-29.
35. Rich, L. and P. Whittaker, *Collagen and Picrosirius Red Staining : a Polarized Light Assessment of Fibrillar Hue and Spatial Distribution.* Brazillian Journal of Morphological Sciences, 2005. **22**: p. 97-104.
36. Lavagnino, M., et al., *Crimp length decreases in lax tendons due to cytoskeletal tension, but is restored with tensional homeostasis.* Journal of Orthopaedic Research, 2017. **35**: p. 573-579.
37. Cox, T.R. and J.T. Erler, *Remodeling and homeostasis of the extracellular matrix: implications for fibrotic diseases and cancer.* Disease Models & Mechanisms, 2011. **4**: p. 165-178.
38. Riching, K.M., et al., *3D Collagen Alignment Limits Protrusions to Enhance Breast Cancer Cell Persistence.* Biophysical Journal, 2014. **107**: p. 2546-2558.
39. Shirani, J., et al., *Morphology and significance of the left ventricular collagen network in young patients with hypertrophic cardiomyopathy and sudden cardiac death.* Journal of the American College of Cardiology, 2000. **35**(1): p. 36-44.
40. Conklin, M.W., et al., *Aligned collagen is a prognostic signature for survival in human breast carcinoma.* American Journal of Pathology, 2011. **178**(3): p. 1221-32.
41. Provenzano, P.P., et al., *Collagen reorganization at the tumor-stromal interface facilitates local invasion.* BMC Medicine, 2006. **4**(1): p. 38.
42. Junqueira, L.C., G.S. Montes, and E.M. Sanchez, *The influence of tissue section thickness on the study of collagen by the Picrosirius-polarization method.* Histochemistry, 1982. **74**: p. 153-156.
43. Montes, G.S. and L.C. Junqueira, *The use of the Picrosirius-polarization method for the study of the biopathology of collagen.* Memorias do Instituto Oswaldo Cruz, 1991. **86 Suppl 3**: p. 1-11.
44. Dapson, R.W., *Fixation for the 1990's: a Review of Needs and Accomplishments.* Biotechnic and Histochemistry, 1993. **68**: p. 75-82.
45. Jarrett, A. and J.A. Hardy, *The Value of Alcohol for Fixation of Skin.* Stain Technology, 1957. **32**: p. 225-233.
46. Chen, A.C.H., et al., *Second harmonic generation and multiphoton microscopic detection of collagen without the need for species specific antibodies.* Burns, 2011. **37**: p. 1001-1009.

47. Pena, A., et al., *Three-Dimensional Investigation and Scoring of Extracellular Matrix Remodeling During Lung Fibrosis Using Multiphoton Microscopy.* Microscopy Research and Technique, 2007. **70**: p. 162-170.
48. Bennike, T.B., et al., *Comparing the proteome of snap frozen, RNAlater preserved, and formalin-fixed paraffin-embedded human tissue samples.* EuPA Open Proteomics, 2016. **10**: p. 9-18.
49. Berney, D.M., R. Montironi, and L. Egevad, *Pathology in prostate research: Optimizing tissue quality.* Acta Oncologica, 2011. **50**: p. 53-55.
50. Su, J.M.F., et al., *Comparison of ethanol versus formalin fixation on preservation of histology and RNA in laser capture microdissected brain tissues.* Brain pathology (Zurich, Switzerland), 2004. **14**: p. 175-182.
51. Folkvord, J.M., et al., *Optimization of immunohistochemical techniques to detect extracellular matrix proteins in fixed skin specimens.* The journal of histochemistry and cytochemistry : official journal of the Histochemistry Society, 1989. **37**: p. 105-113.
52. Beckstead, J.H., *A simple technique for preservation of fixation-sensitive antigens in paraffin-embedded tissues.* Journal of Histochemistry & Cytochemistry, 1994. **42**: p. 1127-1134.
53. Ezaki, T., *Antigen retrieval on formaldehyde-fixed paraffin sections: Its potential drawbacks and optimization for double immunostaining.* Micron, 2000. **31**: p. 639-649.
54. Florell, S.R., et al., *Preservation of RNA for functional genomic studies: a multidisciplinary tumor bank protocol.* Modern pathology : an official journal of the United States and Canadian Academy of Pathology, Inc, 2001. **14**: p. 116-128.

CHAPTER 5: AGE-RELATED EXTRACELLULAR MATRIX CHANGES IN THE HUMAN AORTIC VALVE

5.1 Abstract

Aging is a major risk factor for the development of aortic valve stenosis, with every 10 years of age resulting in a 2-fold increase in risk of developing the disease. However, despite the prevalence of aortic valve stenosis and the increased average age of the population, limited investigations into the aging of the aortic valve have been reported. The aim of this chapter is to investigate aging of the human aortic valve through analysis of the extracellular matrix. Aortic valve specimens from a wide age range of humans were used to investigate age-related changes in major valve extracellular matrix components such as collagen, proteoglycans, and glycosaminoglycans. While total collagen and proteoglycan content did not change with age, analysis of collagen fiber architecture using second harmonic generation microscopy revealed a decrease in collagen fiber width and increase in alignment in the aging fibrosa. Analysis of the expression of both enzymatic and non-enzymatic collagen crosslinkers revealed no difference in the expression of lysyl oxidase (LOX) and lysyl hydroxylase 1 (PLOD1), however the content of advanced glycation end products (AGEs) was reported to decrease in the valve with aging. Together, the findings of this study suggest that collagen undergoes age-dependent alterations in micro-architecture and non-enzymatic modification.

5.2 Introduction

Aging is a phenomenon that affects the extracellular matrices of tissues throughout the human body. While aging increases the risk for development of many diseases [1, 2], the mechanisms behind aging that influence disease progression are not fully understood. This is especially true in the case of aortic valve stenosis, where aging is a major risk factor associated with a 2-fold increase in risk for disease development with every 10 years of age [3, 4]. Throughout the body, aging has been associated with alterations in the extracellular matrix (ECM) of tissues [5], including changes in the content and distribution of ECM components such as collagen[6], proteoglycans (PGs) [5], and elastin [7]. Yet while ECM alteration is a common component in the aging tissue, the presentation of aging in the ECM varies with tissue type. In the cardiovascular system, for example, the arterial walls thicken with age due to an increase in collagen [8], while in the renal ECM, collagen is constant but increases in fibronectin are reported [6]. While age-related changes to ECM components appear to vary by tissue, factors that modify ECM structures such as advanced glycation end-products (AGEs) have been shown to play a role in aging of a variety of tissues [9, 10] and may influence the age-related progression of some diseases.

Like other tissues, the aortic valve is susceptible to changes in its ECM as a result of aging. However, until recently aortic valve disease was thought to be the result of normal aging of the valve. The result of this is that aging-focused studies of the aortic valve to included diseased valves in their investigations [11, 12]. As a result, many of the initial conclusions about aging of the aortic valve included changes in the valve ECM

that are now associated with disease, such as increased overall thickness of the valve and calcium deposition [11, 13, 14]. Recent investigations into aging of the aortic valve suggest changes in the content of major valve ECM components such as collagen and PGs occur with age, however the majority of these studies have been conducted in non-human models of the aortic valve [15, 16] or only investigate aging of the valve from development through adulthood [17, 18], before individuals reach an age at which there is elevated risk for CAVD.

As noted above, currently available studies of valve aging did not encompass the age range of increased CAVD risk, which occurs past the age of 65. Therefore, it was the aim of this study to investigate whether these ECM alterations continue into late adulthood, when the risk of diseases such as CAVD increases. Most previous studies into the ECM alterations that occur during aging of CAVD have been focused on bulk changes in ECM composition, with little investigation into the changes in ECM during aging that may occur in the nano- and microscale architecture of the valve. Therefore, this study also aimed to characterize collagen architecture at the fibrillar level, to better understand age-related changes that may occur in the micro-architecture of the valve and contribute to changes in the function of the valve. This analysis employed traditional histological techniques with second harmonic generation microscopy to gain a clear understanding of age-related alterations in the extracellular matrix of the aortic valve.

5.3 Methods and Materials

All reagents used were purchased from Sigma Aldrich (St. Louis, MO) unless otherwise indicated.

5.3.1 Tissue Acquisition

Aortic valve leaflets from individuals 21–80 years of age were collected from the University of Wisconsin Hospital and the William S. Middleton Veterans Memorial Hospital in Madison, WI. Healthy aortic heart valves were obtained within 24 hours post-mortem from individuals with no previous diagnosis of CAVD; this protocol was reviewed by the UW-Madison IRB and granted an exemption (#2012–0721) due to not qualifying as human subjects research as defined under 45 CFR 46.102(f). Tissues were embedded in paraffin and sectioned in 5 μm slices for histological staining or 13–15 μm slices for SHG imaging.

As only healthy tissues were used for the following investigations, histological analysis was used to confirm a healthy status of tissue specimens prior to further investigation. Specifically, the width of leaflet cross-sections that had undergone Movat's pentachrome staining was measured using ImageJ software at 40 different locations within the tissue interior (i.e., a minimum of 100 μm from the free and attached edges). Leaflets <700 μm thick were considered healthy and used for the following experiments.

5.3.2 Histological Staining

Deparaffinized tissue sections were stained with Movat's pentachrome for connective tissue (Poly Scientific R&D Corp., Bay Shore, NY) and mounted using Permount prior to being imaged using a Zeiss AX10 inverted microscope.

5.3.3 Quantification of Proteoglycans and Glycosaminoglycans

Prior to immunohistological staining and analysis of chondroitin sulfate (CS), biglycan, versican, and decorin, tissue sections were deparaffinized using xylene substitute followed by decreasing concentrations of ethanol. Antigen retrieval was performed by submersion of deparaffinized tissues in a citric acid solution (Vector Laboratories, Burlingame, CA) for 2 hours at 80°C. Following antigen retrieval, sections were incubated for 1 hour at room temperature in 0.03% hydrogen peroxide in methanol to quench endogenous peroxidase activity. Sections then underwent a 1 hour incubation in chondroitinase to remove GAGs that interfere with antibody binding to the targeted proteoglycan core prior to overnight blocking at 4°C using the blocking reagent from the Universal Vectastain Elite ABC system (Vector Laboratories). Following blocking, tissues were incubated for 1 hour at room temperature in the respective antibodies. Biglycan was detected using a rabbit polyclonal anti-biglycan antibody (bs-7552R, Bioss Antibodies, MA) while a rabbit polyclonal anti-versican antibody (bs-2533R, Bioss Antibodies) and rabbit polyclonal anti-decorin antibody (bs-1695R, Bioss Antibodies) were used to detect and quantify verican and decorin, respectively. A mouse monoclonal anti-chondroitin sulfate antibody (C8035) that does not react with dermatan

sulfate was used for CS quantification. All antibodies were diluted 1:100 for using in immunohistological staining.

Immunohistological staining of hyaluronic acid (HA) was conducted using a biotinylated HA-binding protein, produced in bovine nasal cartilage. Tissue sections were deparaffinized and prepared as previously discussed, followed by blocking in 1% bovine serum albumin (BSA) overnight at 4°C. Sections were incubated for 1 hour at room temperature in HA-binding protein and diluted to 5 mg/mL in 1% BSA, followed by three washes in 1x PBS. Tissue sections were incubated for 1 hour with a HRP-conjugated anti-biotin antibody prior to development using ImmPACT DAB Peroxidase (HRP) Substrate (Vector Laboratories). Following development, tissues were rinsed in 1xPBS and mounted in Clearmount mounting solution (Life Technologies). Imaging of tissues stained for HA and proteoglycans was completed using a Zeiss AX10 inverted microscope.

5.3.4 Quantification of Collagen via Dot Blot

A total of five tissue sections of 10 μm thickness were digested overnight at 55°C in a solution of >600mAU/mL proteinase K (Qiagen, Hilden, Germany), diluted 1:8 in diH_2O. The total protein content of tissue digest was determined using a Micro BCA Assay kit (Thermo Fisher Scientific, Waltham, MA). Digests were diluted to a concentration of 5 μg/μL total protein, and 1 μL of each tissue digest was loaded onto a PVDF membrane (Bio-Rad Laboratories, Hercules, CA) that had been soaked in methanol for one minute and rinsed in diH_2O for 5 minutes. Collagen quantification was completed using a

picrosirius red dot blot method described previously [19], utilizing rat tail collagen type I to create a standard curve from 0.1 to 0.8 µg/µL. PVDF membranes were imaged using a ChemiDoc™ MP (Bio-Rad) and analyzed using FIJI. Prior to intensity measurements, the FIJI Subtract Background command was used, and signals were measured using a circular selector of the same size for all standards and samples on the membrane.

5.3.5 COL1A1 and LOX Gene Expression via qRT-PCR

Expression of *COL1A1* and *LOX* was evaluated in a subset of available tissues through qRT-PCR. Isolation of RNA from tissues sections was completed using the RNeasy FFPE kit (Qiagen), which is specifically tailored for the isolation of RNA from formalin fixed and paraffin embedded (FFPE) tissues. Isolated RNA was checked for quantity and quality via a Nanodrop (Thermo Fisher Scientific) prior to cDNA synthesis using a High-Capacity cDNA Reverse Transcription Kit (Applied Biosystems, Carlsbad CA). Taqman Gene Expression Assays (Applied Biosystems) for *COL1A1* (Hs00164004_m1) and *LOX* (Hs00180_m1) were used for RT-PCR amplification. The ΔΔCt method was used to normalize to *GAPDH* (Hs02758991_g1) and determine relative expression of *COL1A1* and *LOX* genes in a young and old subset of tissue specimens.

5.3.6 Second Harmonic Generation Imaging

SHG imaging was conducted on tissue sections from the belly region of aortic valve leaflet specimens. Prior to imaging, tissue sections were deparaffinized in xylene substitute, followed by graded washes in ethanol. Washed tissues sections were mounted under coverslips, sealed with lacquer, and stored at 4°C until undergoing

imaging. SHG imaging of prepared tissue sections was completed within 2 weeks after deparaffinization to ensure integrity of the tissue structures. SHG imaging of collagen was completed using a previously defined system. Briefly, this system utilizes a mode-locked 890 nm laser and 40x water-immersion objective (working distance 3mm, 0.8NA) on an upright Olympus BX61 microscope (Olympus, Tokyo, Japan) to measure SHG at 445 nM (20 nm bandpass filter) under a 2x digital zoom. This system was controlled through an Olympus Fluoview300 scanning system.

5.3.7 Fiber Analysis

Three SHG z-stacks per tissue section were imaged from eight male and seven female specimens between the ages of 21 and 80 years of age. Throughout each z-stack, images were taken at an interval of 1 μm. Three serial images from the interior of each z-stack were analyzed together to negate signal changes due to tissue edge effects and to better characterize fibers angled out of a single plane. Fiber structure was analyzed using the open source software ctFIRE V1.3 Beta and CurveAlignV3.0 Beta2, both of which were developed by the Laboratory for Optical and Computational Instrumentation (LOCI) at the University of Wisconsin-Madison. Both ctFIRE and CurveAlign were run using MATLAB software (The MathWorks, Inc., Natick, MA) as the platform. SHG images in an 8-bit tiff format were imported into the program to undergo curvelet transform (CT) reconstruction using CurveLab 2.1.2 (April 2008) followed by creation of fiber overlays via the FIRE algorithm. Measurements from ctFIRE were imported to CurveAlign to undergo feature analysis, enabling final output of fiber features to undergo feature analysis through CurveAlign enabling final fiber features from selected

fibers to be output into an Excel file format (Microsoft, Redmond, WA) to undergo statistical analysis.

Analysis through ctFIRE followed by CurveAlign allowed for characterization of the length, width, curvature, density, and alignment of fibers within each SHG image. Total length refers to the full length of the fiber within the plane of view, tracing along any curving or crimping the fibers may display. The end-to-end fiber length measurement is the straight distance from one end of the fiber to the other end within the plane of view, without tracing along the length of the fiber. Curvature is a ratio of these two characteristics, thereby describing the degree of curving and/or crimping the fibers display. Fiber width is the average width as measured along the length of the fiber. Fiber density and alignment were measured in relation to the nearest 2, 4, 8, and 16 nearest neighboring fibers as well as in image regions of defined area: 11.25 μm x 11.25 μm, 22.5 μm x 22.5 μm, and 45 μm x 45 μm. Box density refers to the number of fibers within a specified area, while Distance to Nearest indicates the distance to the closest of a specified number of fibers. Alignment of Nearest and Box Alignment are calculated in relation to the nearest of a specified number of neighboring fibers and the alignment within a designated area, respectively; an alignment value of one indicates parallel alignment to the neighboring fibers, while a value of zero indicates that the fiber is perpendicular to the specified comparison set.

5.3.8 Detection of ECM Crosslinking Enzymes and End-Products

Prior to immunohistological staining for lysyl oxidase (LOX), procollagen-lysine,2-oxoglutarate 5-dioxygenase 1 (PLOD1), and advanced glycation end-products (AGEs), tissue sections were deparaffinized using xylene followed by decreasing concentrations of ethanol. Antigen retrieval was performed by submersion of deparaffinized tissues in a citric acid solution (Vector Laboratories, Burlingame, CA) for 2 hours at 80°C. Following antigen retrieval, sections were incubated for 1 hour at room temperature in 0.03% hydrogen peroxide in methanol to quench endogenous peroxidase activity. Sections were then blocked overnight at 4°C using the blocking reagent from the Universal Vectastain Elite ABC system (Vector Laboratories). LOX staining was conducted using a rabbit polyclonal anti-LOX antibody (1:100, ab31238, Abcam, Cambridge, MA), while PLOD1 was detected using a rabbit polyclonal anti-PLOD1 antibody that recognizes the N-terminus (aa73-102) of human PLOD1 (1:50, ab171140, Abcam), and AGEs were detected using a rabbit polyclonal anti-AGE antibody (1:500, ab23722, Abcam). The Universal Vectastain Elite ABC system (Vector Laboratories) was used as the secondary antibody and combined with ImmPACT DAB Peroxidase (HRP) Substrate (Vector Laboratories) to provide detection of protein expression via colorimetric development.

Quantification of LOX, PLOD1, and AGE expression was performed by capturing three images per tissue using an Olympus IX51 inverted microscope. Using FIJI, images were divided into the respective color channels. The channel for DAB was thresholded across all samples, and the total percent area of DAB positive staining was measured. This

measurement was normalized to total tissue area by measurement of complete area covered by tissue within each individual image.

5.3.9 Statistical Analysis

Statistical analysis of SHG fiber characteristics was completed in Prism 6 (Graphpad Software, Inc., La Jolla CA) using a one-way ANOVA followed by a Tukey post hoc test. All other comparisons between two groups were completed using two-tailed, unpaired t-tests assuming unequal variance. Differences were determined to be significant when $p<0.05$. For experiments using a subset of the available tissues specimens, a total of 10 individuals (N = 4 young, N = 6 old) were analyzed. For all other experiments, a total of 15 individuals (N = 8 male, N = 7 female) were analyzed.

5.4 Results

5.4.1 Valve Classification

Staining of acquired human valves with Movat's pentachrome revealed a trilaminar structure indicative of a healthy valve across age ranges (Figure 5.1). Collagen, noted by a yellow stain, identified the fibrosa, while blue stains and purple to black staining identify GAGs and elastin content in the spongiosa and ventricularis, respectively.

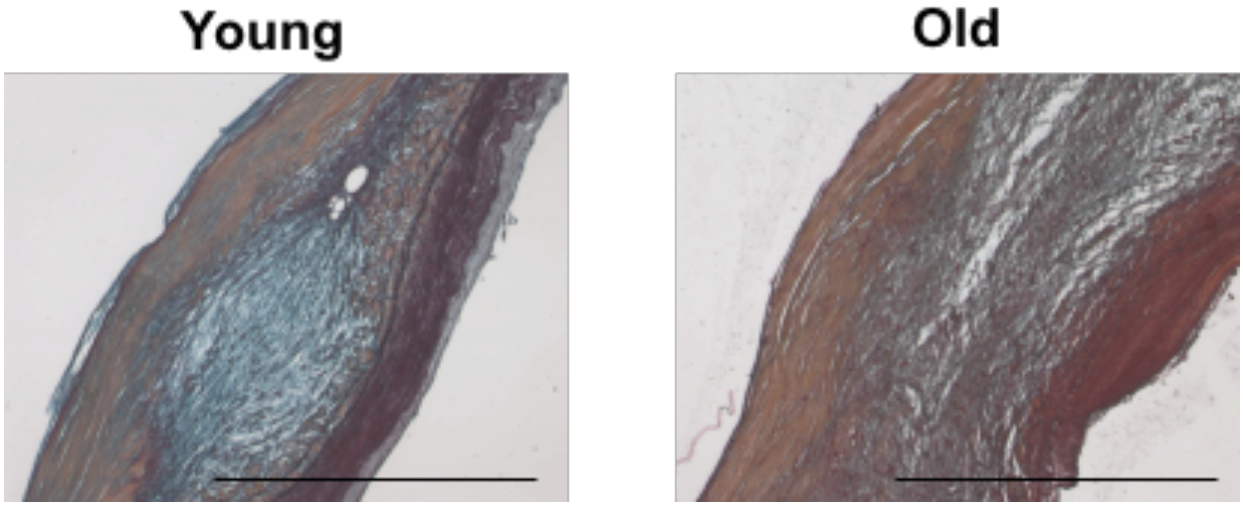

Figure 5.1 Image of Young (left, age 51) and Old (right, age 64) male human valve tissues stained with Movat's pentachrome. Scale bar = 0.50mm.

Due to a limited number of available tissue sections, not all investigations conducted in this study could be performed on the same set of human specimens. To account for differences across tissue sets, the average age was calculated between groups to ensure human specimens met the required criteria for the study. Measurement of the thickness of leaflets across groups was also conducted to both ensure leaflets were healthy, with no measureable thickening associated with sclerosis, and that there was no difference in thickness that could influence reported results. For the data presented in Figure 5.3 and Figures 5.7-9 the specimens listed in Table 5.1 were used. For Figures 5.4 and 5.10, Table 5.2 specimens were used. For generation of SHG analysis in Table 5.4 the specimens in Table 5.3 were used.

For immunohistological comparisons of “old” and “young” tissues and analysis of PG content, a subset of the available tissues was used (Table 5.1). Average age was statistically different ($p < 0.001$) between tissues classified as young, with an average age of 47 ± 4.4 years, and those classified as old, with an average age of 68 ± 4.0 years. Histological evaluation of leaflet cross section demonstrated that there was no difference in thickness between tissues classified as young and those classified as old ($p = 0.11$).

Table 5.1 Subset Of Tissues For Comparisons Of PGs, Collagen Content, LOX, And PLOD1 In Young Vs Old Tissues

Sex	Classified	Age (yrs)	Mean Age (yrs) ($p < 0.001$)	Tissue Section Thickness (μm)	Mean Thickness (μm) ($p = 0.11$)
Male	Y	42	47± 4.4	550 ± 190	460 ± 140
Male	Y	44		590 ± 370	
Female	Y	50		420 ± 89	
Male	Y	51		280 ± 130	
Male	O	64	68 ± 4.0	630 ± 250	570± 76
Male	O	65		450 ± 120	
Male	O	66		520 ± 140	
Female	O	66		630 ± 83	
Male	O	69		540 ± 260	
Male	O	75		630 ± 130	

Investigations into differences in aging accounting for the sex of the tissue were conducted using a set of eight male tissues, age 21 to 75 years old, and a set of seven female tissues, age 27 to 80 years old (Table 5.2). The average age for males (55 ± 17 years) was not significantly different from females (58 ± 18 years, $p = 0.8$). The average thickness of the valves was also not statistically significant between groups ($p = 0.8$)

Table 5.2 Tissue Specimen Information for Immunohistological Comparisons Incorporating Sex

Sex	Age Category	Age (yrs)	Mean Age (yrs) (p = 0.8)	Tissue Section Thickness (μm)	Mean Thickness (μm) (p = 0.8)
Male	Y	21	55 ± 17	210 ± 20	460 ± 150
Male	Y	42		550 ± 190	
Male	Y	52		430 ± 130	
Male	Y	53		550 ± 130	
Male	Y	59		280 ± 99	
Male	O	66		520 ± 140	
Male	O	69		540 ± 260	
Male	O	75		630 ± 130	
Female	Y	27	57 ± 18	-	440 ± 140
Female	Y	47		-	
Female	Y	50		420 ± 89	
Female	Y	51		260 ± 150	
Female	O	69		580 ± 120	
Female	O	73		500 ± 140	
Female	O	80		-	

Analysis of age-based differences in collagen microarchitecture through SHG microscopy was completed on a secondary subset of “old” and “young” tissues (Table 5.3). The average age was statistically different ($p < 0.001$) between tissues classified as young, with an average age of 51 ± 5.9 years, and those classified as old, with an average age of 67 ± 3.8 years. The average thickness of tissues classified as young and old was not significantly difference ($p = 0.19$), with young tissues having an average thickness of 400 ± 150 μm and old tissues having an average thickness of 500 ± 140 μm.

Table 5.3 Subset of Tissues Used for Young vs Old Comparisons via SHG Imaging

Sex	Classified	Age (yrs)	Mean Age (yrs) ($p < 0.001$)	Tissue Section Thickness (μm)	Mean Thickness (μm) ($p = 0.19$)
Male	Y	42	51 ± 5.9	550 ± 190	400 ± 150
Male	Y	44		590 ± 370	
Female	Y	51		260 ± 150	
Male	Y	51		280 ± 130	
Male	Y	52		430 ± 130	
Male	Y	53		550 ± 130	
Male	Y	58		260 ± 88	
Male	Y	59		280 ± 130	
Male	O	62	67 ± 3.8	480 ± 140	500 ± 140
Male	O	64		630 ± 250	
Male	O	65		450 ± 120	
Male	O	66		520 ± 140	
Female	O	66		630 ± 83	
Male	O	69		540 ± 260	
Female	O	69		580 ± 120	
Male	O	73		150 ± 250	
Female	O	73		500 ± 140	

5.4.2 Proteoglycan Content Remains Unchanged with Aging

Biglycan, decorin, and versican are the three most abundant proteoglycans found in the aortic valve [20, 21]. Expression of all three proteoglycans was observed in the fibrosa, with biglycan expression present in 40 percent of the total area of the fibrosa in the two youngest tissues (Figure 5.2A). However, this was not consistent with all tissues considered young, and no strong correlation was observed with age (R^2= 0.213, p = 0.250) Decorin and versican expression (Figure 5.2 B-C) was observed in over 20 percent of the total fibrosa area in the majority of tissues, regardless of age.

Overall expression of all three proteoglycans was not as strong in the spongiosa (Figure 5.3A-B), where biglycan and decorin were detected in less than 40 percent of the overall fibrosa. Versican, however, was observed throughout nearly 80 percent of the spongiosa (Figure 5.3C). While significant amounts of each of these proteoglycans were detected in the fibrosa, biglycan, decorin and versican expression in the spongiosa did

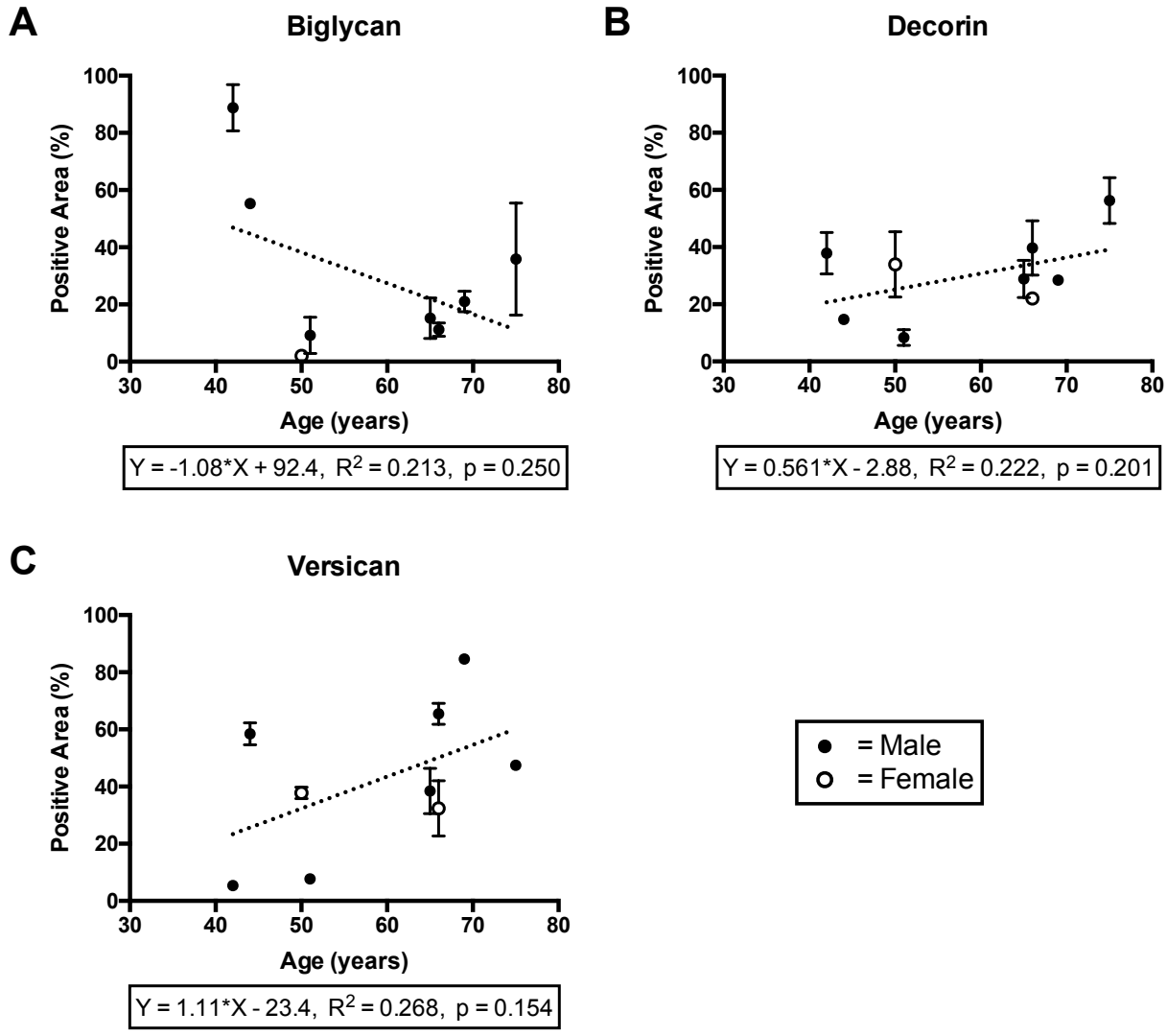

Figure 5.2 Immunohistochemical quantification of proteoglycans in the fibrosa. Quantification of the percentage of total tissue area positive for expression of biglycan (A), decorin (B), and versican (C) in the fibrosa of a subset of human valve tissues. No significant correlation was found between PGs and aging in the fibrosa.

not show a strong correlation with age.

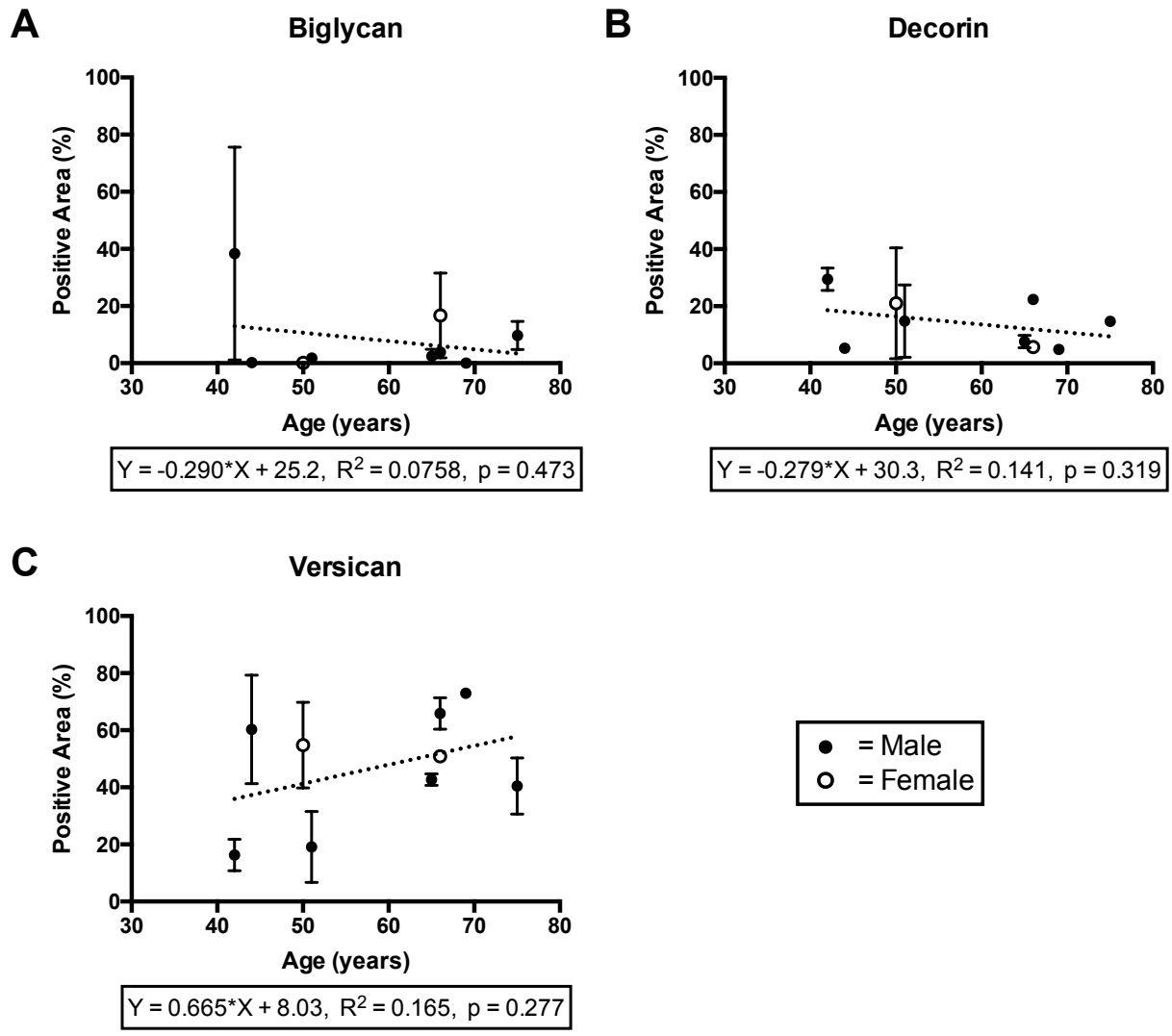

Figure 5.3 Immunohistochemical quantification of proteoglycans in the spongiosa. Quantification of the percentage of total tissue area positive for expression of biglycan (A), decorin (B), and versican (C) in the spongiosa of a subset of human valve tissues. No significant correlation was found between PGs and aging in the spongiosa.

5.4.3 Glycosaminoglycan Content Remains Unchanged with Aging

Biglycan, decorin, and versican are all proteoglycans formed through binding of their core proteins with chains of chondroitin sulfate (CS) or dermatan sulfate (DS). Other proteoglycans, such as aggrecan, are also composed of core proteins attached to chains of chondroitin sulfate. As the length of these CS chains can vary, the amount of CS in the aortic valve was investigated to construct a clear understanding of age-related changes in the extracellular matrix composition (Figure 5.4A). Expression of CS throughout the valve showed a linear decrease (Y = -0.25*X + 53), however this was not statistically significant. The CS content of the valve was also not significant upon separation of tissues into male and female subgroups (no shown). This indicates that CS is conserved with aging, independent of sex.

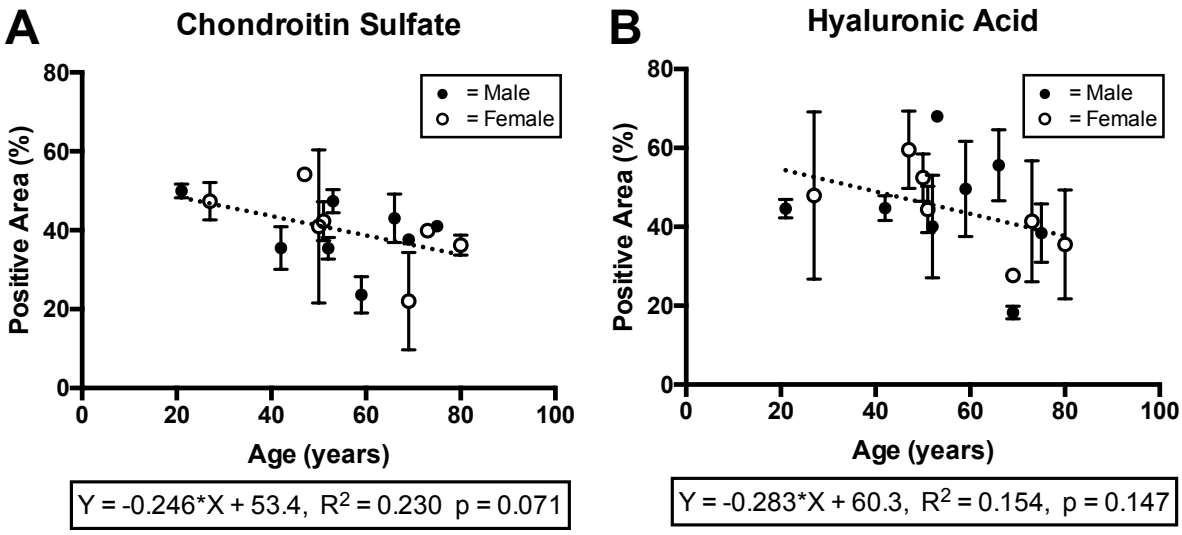

Figure 5.4 Immunohistochemical quantification of CS and HA throughout all layers of the aortic valve. Quantification of CS (A) and HA (B) throughout the trilaminar structure of a subset of human valve tissues. No significant correlation between CS or HA content was observed with increasing age.

Increases in HA have been observed in models of early-stage CAVD and in porcine models of aortic valve aging[20]. As a result, quantification of the percentage of HA in a subset of human valves was analyzed in relation to increasing age (Figure 5.4B). However, no significant change in the HA content of the valve was observed. HA content in the valve also did not show a sex-dependent change with age (data not shown).

5.4.4 Age-Related Changes in Collagen Architecture via SHG

Due to the prevalence of collagen in the aortic valve, collagen fiber architecture was characterized in old and young valves. SHG imaging of the fibrosa (Figure 5.5) and spongiosa (Figure 5.6) of valve leaflet sections were conducted to determine whether aging was associated with changes in the characteristics of individual collagen fibers and their organization relative to neighboring fibers. SHG exploits the ability of fibrillar collagen to generate a second harmonic wave (at 445 nm), allowing for investigating into detailed micro-level structural information without staining or chemical treatment.

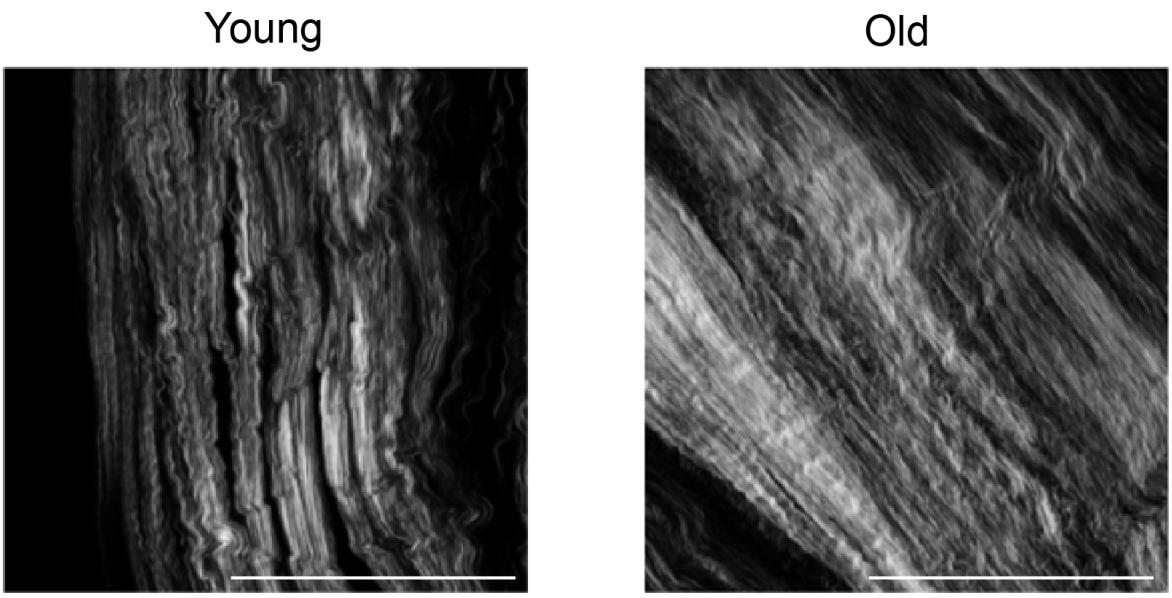

Figure 5.6 SHG images of the fibrosa of human specimens. Images of Young (left) and Old (right) fibrosa. Scale bar = 100 μm.

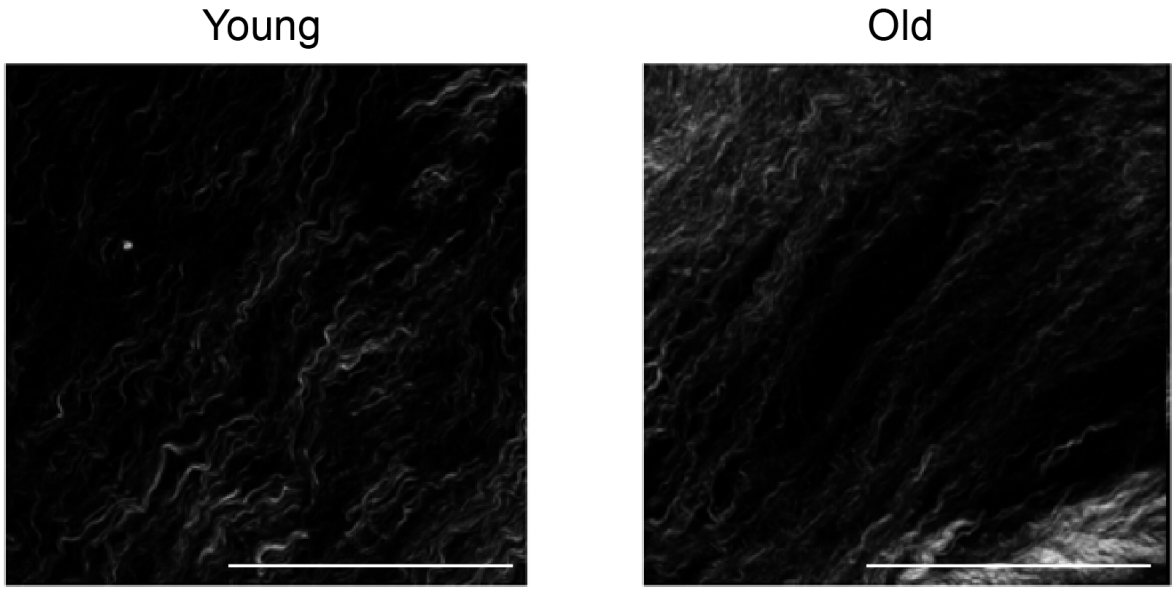

Figure 5.5 SHG images of the spongisa of human specimens. Images of Young (left) and Old (right) fibrosa. Scale bar = 100 μm.

In the fibrosa, most characteristics were consistent across the two age groups. However, collagen fiber width significantly decreased with age ($p < 0.001$) and fiber alignment increased ($p < 0.001$), suggesting that aging results in a fibrosa that is increasingly aligned with thinner fibers. These changes were not observed in the spongiosa, with fibers showing consistent width and alignment with aging. Collagen fiber density in the spongiosa was also consistent between young and old tissues, suggesting that the majority of age-related alterations in valve collagen structure occur in the fibrosa.

Table 5.4 Collagen fiber characteristics in the fibrosa and spongiosa of young vs. old aortic valve leaflets.

	FIBROSA		SPONGIOSA	
MEASUREMENT	YOUNG AVERAGE	OLD AVERAGE	YOUNG AVERAGE	OLD AVERAGE
FIBER DIMENSIONS				
Fiber Width (μm)	1.94 ± 0.0434	1.88 ± 0.0451[F]	1.68 ± 0.116	1.69 ± 0.0825
FIBER DENSITY				
Distance to Nearest 2	7.90 ± 0.294	7.76 ± 0.266	9.88 ± 1.28	10.5 ± 1.97
Distance to Nearest 4	10.3 ± 0.384	10.1 ± 0.306	13.0 ± 2.00	13.9 ± 2.96
Distance to Nearest 8	13.8 ± 0.513	13.6 ± 0.390	18.0 ± 3.25	19.7 ± 5.08
Distance to Nearest 16	19.3 ± 0.771	19.0 ± 0.550	25.8 ± 5.16	28.4 ± 6.62
Box Density 11.25 μm x 11.25 μm	1.62 ± 0.0452	1.66 ± 0.0607	1.46 ± 0.0767	1.46 ± 0.0642
Box Density 22.5 μm x 22.5 μm	4.20 ± 0.215	4.30 ± 0.182	3.41 ± 0.410	3.24 ± 0.381
Box Density 45 μm x 45 μm	14.2 ± 0.974	14.6 ± 0.694	10.5 ± 1.95	9.6 ± 1.82
FIBER ALIGNMENT				
Curvature	0.924 ± 0.00678	0.928 ± 0.00382	0.912 ± 0.00947	0.913 ± 0.00582
Alignment of Nearest 2	0.887 ± 0.028	0.913 ± 0.0125[F]	0.811 ± 0.0537	0.802 ± 0.0360
Alignment of Nearest 4	0.838 ± 0.468	0.870 ± 0.180	0.720 ± 0.0731	0.710 ± 0.0602
Alignment of Nearest 8	0.811 ± 0.0548	0.850 ± 0.0228	0.672 ± 0.0879	0.658 ± 0.0754
Alignment of Nearest 16	0.795 ± 0.0599	0.837 ± 0.0260	0.638 ± 0.0986	0.621 ± 0.084
Box Alignment 11.25 μm x 11.25 μm	0.932 ± 0.182	0.944 ± 0.0102	0.915 ± 0.0290	0.908 ± 0.0222
Box Alignment 22.5 μm x 22.5 μm	0.844 ± 0.0461	0.875 ± 0.020	0.766 ± 0.750	0.772 ± 0.0479
Box Alignment 45 μm x 45 μm	0.799 ±0.0583	0.839 ± 0.0260	0.672 ± 0.0978	0.665 ± 0.0755

[F]= p<0.05 vs young fibrosa
[S] = p<0.05 vs young spongiosa

5.4.5 Collagen Content in Aging

To investigate if overall collagen content influenced the age-related differences in architecture observed, collagen content in the aortic valve was analyzed by dot blot. While there was an apparent decrease in the amount of collagen in the valve, this was not significantly different (Figure 5.4A). To confirm the results observed at the protein level, expression of *COL1A1* was analyzed. A similar decrease was observed in the expression of *COL1A1*, however the decrease was less than 2-fold (Figure 5.4B). This suggests that overall collagen content is stable with increasing age. It also suggests that alterations in collagen architecture observed were not due to increased expression of *COL1A1.*

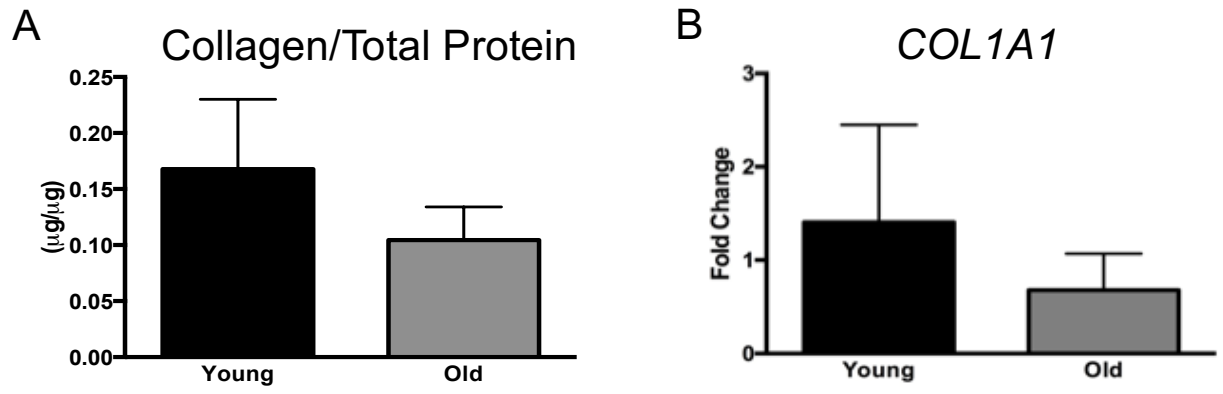

Figure 5.7 Collagen content and expression of *COL1A1*. Total collagen content of the human valve (A) and expression of *COL1A1* (B) in a subset of human tissues. No significant difference observed.

5.4.6 Changes in Collagen Crosslinking with Age

The consistent expression and content of collagen observed could not account for the architectural changes seen in the valve by SHG. Therefore, investigation into the expression of collagen crosslinkers as a potential cause of these changes in collagen architecture was conducted. LOX (Figure 5.8), active in calcific aortic valve disease [22], and PLOD1 (Figure 5.9), common in other cardiovascular pathologies [23], were both investigated. Expression of LOX and PLOD1 were detected in both young and old human valves (Figure 5.8A and 5.9A), however no significant difference was observed. In young valves, LOX and PLOD1 were both observed in about 40 percent of the tissue area (Figure 5.8B and 5.9B). While there was a slight drop in the average expression of PLOD1 to near 20 percent in old tissues, this was not significant.

Further investigation into the expression LOX was conducted at the gene expression level, with *LOX* not showing an age-related difference in expression (Figure 5.8C)

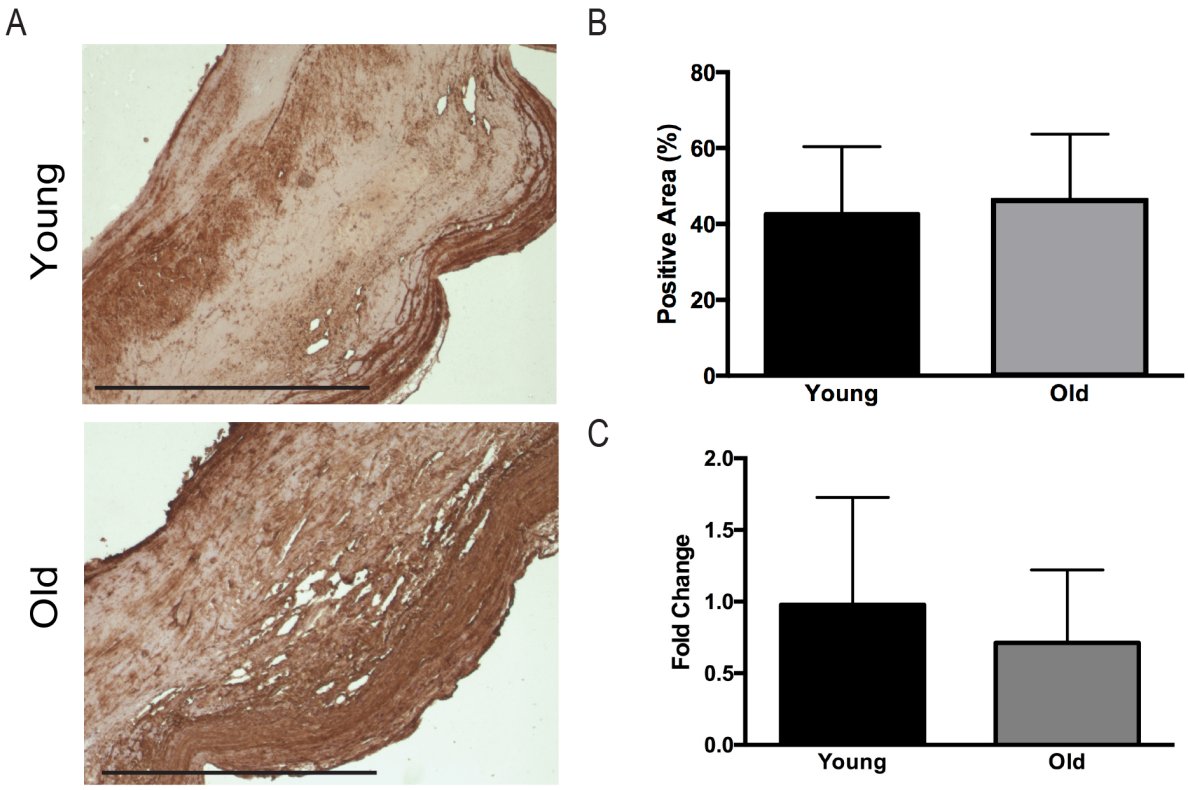

Figure 5.8 Immunohistochemical detection and quantification of LOX in young and old aortic valve leaflets. Images showing positive staining for LOX in both young and old human valves (A). Scale bar = 0.50 mm. Total percentage of the valve section that was positive for LOX was not significantly different between young and old tissues (B). Gene expression of LOX also did not vary as a result of age (C).

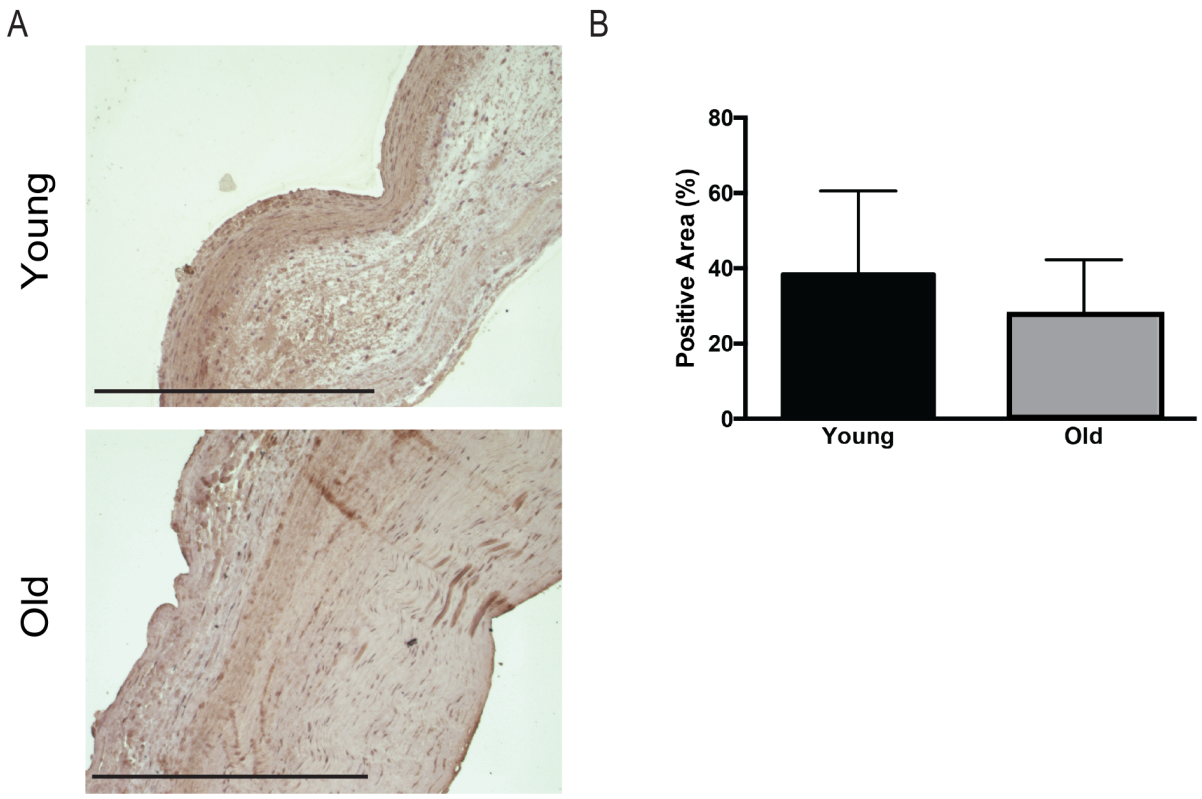

Figure 5.9 Immunohistochemical detection and quantification of PLOD1 in young and old valve leaflets. Images showing positive staining for PLOD1 in both young and old human valves (A). Scale bar = 0.50 mm. Total percentage of the valve section that was positive for PLOD1 was not significantly different between young and old tissues (B).

Advanced glycation end-products (AGEs) result from non-enzymatic crosslinking and have been implicated in many disease pathologies where aging is a risk factor [9, 24]. To determine if AGEs play a role in altering the collagen architecture of the aortic valve with aging, staining and quantification of AGEs was completed (Figure 5.10). Quantification of AGEs in a subset of valves showed a significant decrease in the percentage of tissue that was positive for AGEs as a result of age. Expression of AGEs was also significantly decreased with age in both male ($Y = -0.311*X + 60.1$, $R^2=0.60$, p

= 0.04) and female (Y = -0.35*X + 60.7, R^2=0.7, p = 0.02) subsets investigated. While both sexes showed decrease expression of AGEs with advancing age, females showed a slightly stronger correlation. While changes in collagen content cannot account for this decrease, it is also possible that the change in AGEs is due to increased collagen turnover in the valve.

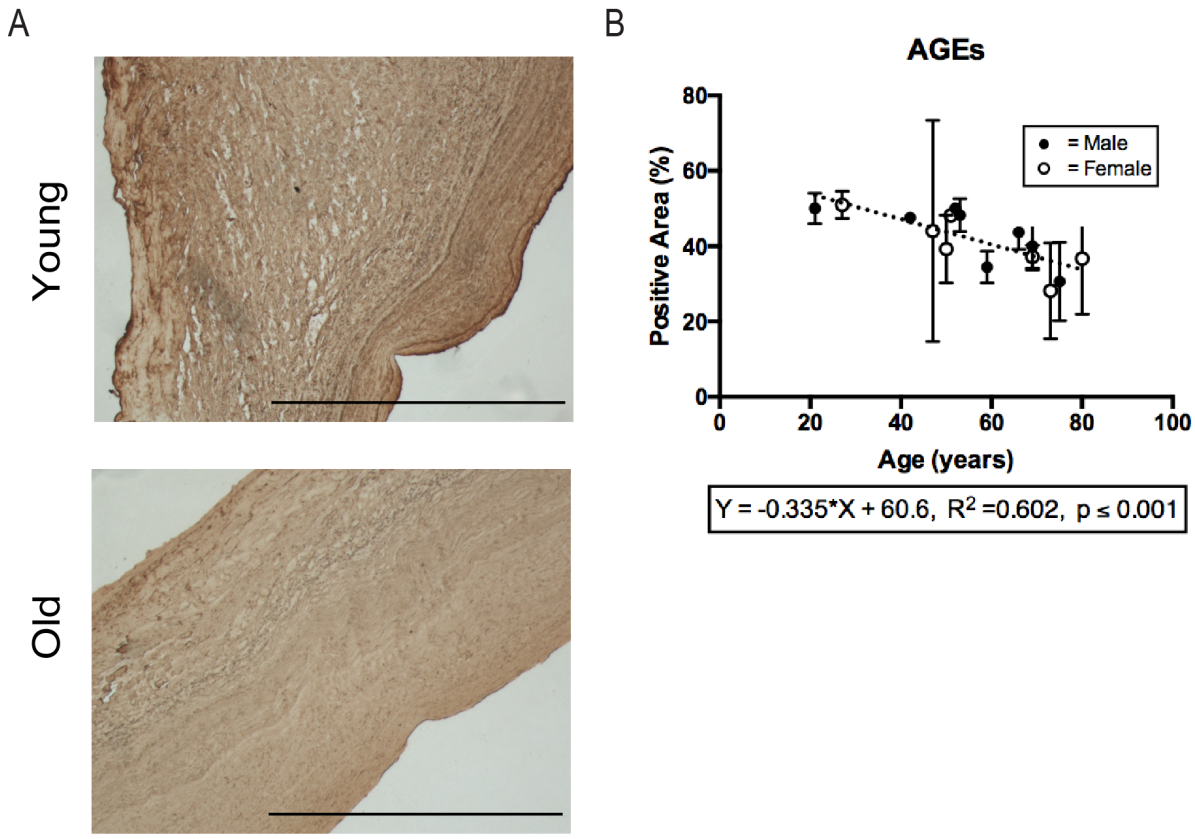

Figure 5.10 Expression of AGEs in Human Valves. Representative images of AGE expression in Young and Old (A) human tissues. Scale bar = 0.50mm. Quantification of the percent of total tissue area positive for AGEs (B). AGE expression was inversely correlated with increasing age (p < 0.001).

5.5 Discussion

Proteoglycans and collagen are two major components of the aortic valve that undergo changes in content and localization during development and disease [15, 21, 25, 26]. While previous studies have helped to characterize the expression of PGs and collagen during development and disease pathology, few studies have characterized the expression of these major ECM components during the adult aging process [17, 18], when risk of developing CAVD begins. This study aimed to characterize the ECM during this overlooked age range by analyzing tissues over the age of 65. Previous studies using porcine models have reported age-related changes in the proteoglycan content of the valve, specifically noting an increase in the content of the small leucine-rich proteoglycans (SLRPs) decorin and biglycan [25] However, using human valves, our investigation into the major proteoglycans, including SLRPS, revealed no changes in expression with aging in either the fibrosa or the spongiosa. Previous findings in porcine models have also indicated an increase in the content of HA with aging of the valve [20], which was not observed in our investigation. While this could illustrate a species-based difference in aging, it could also be due to the difficulties introduced by the heterogeneity of human specimens. Investigations by VanGeeman et al. utilizing human tissues revealed a decrease in the content of sulfated GAGs (sGAGs) with aging [18]. While our study did not specifically investigate differences in the content of sGAGs, our investigations into chondroitin sulfate (CS), a type of sGAG, provide a further insight into the reported decrease in sGAGs and suggest that CS is not the key sGAG that is responsible for the age-related decrease previously observed. It is therefore likely that

other classifications of sGAGs, such as heparan sulfate and keratan sulfate, are responsible for the decrease observed in total sGAG content.

Our investigation into collagen, a second major ECM component that has be shown to change during tissue aging, revealed no change in collagen content with age. While our findings do not support previous work which reported a decrease in collagen content with age[18], it is possible that the inconsistency between studies is due to a difference in the methods used to measure collagen. Our investigations into the organization of collagen fibers revealed changes in the collagen microarchitecture of the aortic valve with aging. Specifically, our findings suggest that during aging of the valve the collagen fibers in the fibrosa become thinner and more aligned while the collagen fibers in the spongiosa remain unchanged. While collagen fiber thickening and increased crosslinking has been noted in diseased valves [22], this finding suggests that aging of the valve in the absence of disease induces a different form of collagen remodeling. Previous findings from studies using human valves have noted an increase in the diameter of the aortic valve with age in response to changes in hemodynamic pressure [18], and changes in stress on the valve in the circumferential direction [17]. Our analysis of changes in the collagen architecture of the fibrosa, which is oriented circumferentially in the valve, suggest that these changes in the collagen fibers in the valve may be in response to the previously noted fluctuations in mechanical stresses.

As our investigations did not note any alteration in the total amount of collagen in the valve, the architectural changes reported in this chapter cannot be explained by a

change in collagen deposition alone. Previous investigations have noted increase in collagen maturation with age, as indicated by an increase in the collagen crosslink content. While our study did not show an age-related change in total expression of LOX and PLOD1 within the valve, it is possible that other crosslinking enzymes not addressed in this study could be expressed in an age-dependent manner resulting in the previously observed changes in collagen crosslink content. Along with enzymatic crosslinkers, content of non-enzymatic AGEs was investigated. While AGEs are reported to increase with age in other cardiovascular tissues [9, 27], a decrease we observed a decrease in the content of AGEs in the valve. It is possible that other factors such as changes in the ratios of types of collagen (I/III), due to increased deposition of collagen III and removal of collagen I via increased matrix metalloproteinases activity are occurring with aging, resulting in removal of AGEs as new collagen is deposited.

5.6 Conclusion

While this study revealed few age-related changes in the extracellular matrix, there are several variables that make investigations into aging a highly complex endeavor. One complicating factor faced by this study is the available samples of healthy human tissue specimens of a variety of ages. Healthy human aortic heart valves are limited, and while this study was fortunate enough to gain over twenty specimens across the age range of interest, the diversity of humans due to genetic, environmental, and dietary differences makes human specimens highly variable within a single group. This makes it difficult to gain a statistically significant difference in expression levels due to the high variability and low number of specimens. A secondary compounding issue in the investigation

into age-related ECM changes is that sex-dependent changes to the ECM have been reported. For example, studies into the myocardium revealed an increase in collagen III in female myocardium that is not observed in the male counterpart [28]. This study supported initial investigations into sex-based differences in aging of the aortic valve, however we were still limited in our ability to gather enough each sex to provide significant differences in the expression of extracellular matrix components. Considering male sex is the second highest risk factor for CAVD after age [29] and male VICs have been reported to express increased markers of ECM remodeling [30], future studies should differentiate the sex of patients to accurately characterize age-related changes in the valve.

5.7 References

1. Stenderup, K., *Aging is associated with decreased maximal life span and accelerated senescence of bone marrow stromal cells,.* Bone, 2003. **33**: p. 919-926.
2. Sinclair, D., et al., *The Intersection Between Aging and Cardiovascular Disease.* 2012. **02115**: p. 1097-1108.
3. Rajamannan, N.M., et al., *Calcific aortic valve disease: not simply a degenerative process: A review and agenda for research from the National Heart and Lung and Blood Institute Aortic Stenosis Working Group. Executive summary: Calcific aortic valve disease-2011 update.* Circulation, 2011. **124**: p. 1783-91.
4. Stewart, B.F., et al., *Clinical Factors Associated With Calcific Aortic Valve Disease.* 1997. **29**: p. 630-634.
5. Silver, F.H., et al., *Physiology of Aging Invited Review : Role of mechanophysiology in aging of ECM : effects of changes in mechanochemical transduction.* 2003. **08854**: p. 2134-2141.
6. Abrass, C.K., M.J. Adcox, and G.J. Raugi, *Aging-associated changes in renal extracellular matrix.* The American journal of pathology, 1995. **146**: p. 742-52.
7. Zarkovic, K., et al., *Elastin aging and lipid oxidation products in human aorta.* Redox Biology, 2015. **4**: p. 109-117.

8. Jacob, M.P., *Extracellular matrix remodeling and matrix metalloproteinases in the vascular wall during aging and in pathological conditions.* Biomedicine & pharmacotherapy = Biomédecine & pharmacothérapie, 2003. **57**: p. 195-202.
9. Brownlee, M., *Advanced protein glycosylation in diabetes and aging.* Annual review of medicine, 1995. **46**: p. 223-34.
10. Nenna, A., et al., *Targeting Advanced Glycation End Products in Cardiac Surgery : The Unexplored Alternative.* 2016. **5**: p. 10-11.
11. Waller, B.F., *The old-age heart: Normal aging changes which can produce or mimic cardiac disease.* Clinical Cardiology, 1988. **11**: p. 513-517.
12. Sell, S. and R.E. Scully, *Aging Changes in the Aorti and Mitral Valves.* Calcification of Cardiac Valves, 1964. **46**.
13. Li, C., S. Xu, and A.I. Gotlieb, *The progression of calcific aortic valve disease through injury, cell dysfunction, and disruptive biologic and physical force feedback loops.* Cardiovascular pathology : the official journal of the Society for Cardiovascular Pathology, 2013. **22**: p. 1-8.
14. O'Brien, K.D., *Pathogenesis of calcific aortic valve disease: a disease process comes of age (and a good deal more).* Arteriosclerosis, thrombosis, and vascular biology, 2006. **26**: p. 1721-8.
15. Stephens, E.H. and K.J. Grande-allen, *Porcine valve as a model for age-specific human heart valve disease : Analysis of collagen turnover throughout development and aging.* 2007. **205**: p. 2007.
16. Balaoing, L.R., et al., *Age-related changes in aortic valve hemostatic protein regulation.* Arteriosclerosis, Thrombosis, and Vascular Biology, 2014. **34**: p. 72-80.
17. Oomen, P.J.A., et al., *Age-dependent changes of stress and strain in the human heart valve and their relation with collagen remodeling.* Acta Biomaterialia, 2016. **29**: p. 161-169.
18. Van Geemen, D., et al., *Age-dependent changes in geometry, tissue composition and mechanical properties of fetal to adult cryopreserved human heart valves.* PLoS ONE, 2016. **11**.
19. Rodríguez-Rodríguez, P., et al., *A simple dot-blot-Sirius red-based assay for collagen quantification.* Analytical and Bioanalytical Chemistry, 2013. **405**: p. 6863-6871.
20. Stephens, E.H., C.-K. Chu, and K.J. Grande-Allen, *Valve proteoglycan content and glycosaminoglycan fine structure are unique to microstructure, mechanical load and age: Relevance to an age-specific tissue-engineered heart valve.* Acta biomaterialia, 2008. **4**: p. 1148-60.
21. Chen, J.-H. and C.a. Simmons, *Cell-matrix interactions in the pathobiology of calcific aortic valve disease: critical roles for matricellular, matricrine, and matrix mechanics cues.* Circulation research, 2011. **108**: p. 1510-24.
22. Hutson, H.N., et al., *Calcific Aortic Valve Disease Is Associated with Layer-Specific Alterations in Collagen Architecture.* Plos One, 2016. **11**: p. e0163858.
23. Wågsäter, D., et al., *Impaired collagen biosynthesis and cross-linking in aorta of patients with bicuspid aortic valve.* Journal of the American Heart Association, 2013. **2**: p. e000034.

24. Asif, M., et al., *An advanced glycation endproduct cross-link breaker can reverse age-related increases in myocardial stiffness.* Proceedings of the National Academy of Sciences of the United States of America, 2000. **97**: p. 2809-13.
25. Stephens, E.H., et al., *Age-related changes in material behavior of porcine mitral and aortic valves and correlation to matrix composition.* Tissue Engineering - Part A, 2010. **16**: p. 867-878.
26. Stephens, E.H., et al., *Differential proteoglycan and hyaluronan distribution in calcified aortic valves.* Cardiovascular Pathology, 2011. **20**: p. 334-342.
27. Ramasamy, R., et al., *Advanced glycation end products and RAGE: a common thread in aging, diabetes, neurodegeneration, and inflammation.* Glycobiology, 2005. **15**: p. 16R-28R.
28. Piro, M., et al., *Sex-Related Differences in Myocardial Remodeling.* JAC, 2010. **55**: p. 1057-1065.
29. Faggiano, P., et al., *Epidemiology and cardiovascular risk factors of aortic stenosis.* 2006. **10207**: p. 1-5.
30. McCoy, C.M., D.Q. Nicholas, and K.S. Masters, *Sex-related differences in gene expression by porcine aortic valvular interstitial cells.* PLoS ONE, 2012. **7**.

CHAPTER 6: SEX BIAS IN THE RESPONSE TO TGF-β1

6.1 Abstract

Aortic valve stenosis affects 1 in 4 people over the age of 65 in the U.S. Male sex is one of the major risk factors for the disease. While recent studies have begun to shed new light on the pathogenesis of aortic valve stenosis, the cause behind increased male risk remains largely unknown. This study aims to investigate how the sex of valvular interstitial cells (VICs) alters the response of quiescent VICs (qVICs) to TGF-β1, a known stimulus for myofibroblastic differentiation. In this chapter, qVICs from male and female pigs were treated with varying amounts of TGF-β1, and downstream alterations in VIC phenotype, ECM expression, and regulation of intracellular signaling were evaluated. The expression of hormone receptors and concentration of estradiol in media formulas were measured to determine the impact of estrogen sensitivity differences in modulating sex-dependent responses to TGF-β1. In these experiments, male qVICs exhibited increased markers of myofibroblast phenotypes compared to female qVICS following treatment with TGF-β1, including increased deposition of extracellular matrix proteins, increased proliferation, and expression of *ACTA2*. Males also exhibited higher levels of SMAD2/3 expression, a downstream signal transducer of TGF-β. Estradiol was present in the media, and estrogen receptor α, a potential modulator of SMAD2/3 expression, was expressed by both male and female VICs. These results indicated that while TGF-β1 is responsible for inducing activation of VICs, males and females have different levels of myofibroblast-like response to TGF-β, potentially mediated by differences in SMAD2/3 expression.

6.2 Introduction

Many cardiovascular diseases present in a sex-biased manner, with men and women being at different risks for diseases such as coronary heart disease [1]. Recent studies into different cardiovascular diseases suggest that determination of sex-related differences in risk of acquiring a cardiovascular disease is difficult due to the different way diseases initially present in males compared to females [2]. Differences in the initial symptoms of diseases may even support differences in disease pathogenesis, further compounding the difficulties in identifying pathology. Calcific aortic valve disease (CAVD) is a disease that presents with a sex bias, with males having a 2-fold increased risk of developing CAVD compared to women [3, 4]. Recent studies into the pathogenesis of CAVD suggest that, in addition to males being at higher risk for CAVD, males and females may have a different pathogenesis. A study by Aggarwal, et al. suggested that females presenting with a similar level of aortic sclerosis as males (as determined by guidelines for aortic sclerosis [5]) have a lower level of aortic calcification[6]. It was also determined that differences observed in calcification occurred due to a higher degree of fibrosis in females compared to males [2, 6]. These findings support the notion that CAVD pathogenesis may vary in a sex-dependent manner. Therefore, further studies into how sex alters CAVD initiation and progression are needed.

To further investigate how these sex-based differences present in CAVD, this study aimed to investigate sex-related differences at the cellular level. Previous studies have shown that cells isolated from male and female valve specimens retain sex-related

differences observed at the tissue level, with male cells exhibiting a higher level of osteogenic markers [7]. These sex-dependent differences in osteogenic markers support further cell-based in vitro studies aimed at understanding the impact of these sex-related differences on disease progression. These findings also support previous studies where males diagnosed with aortic valve stenosis have higher calcium scores than females as measured by computed tomography [6]. Together, these studies underscore the necessity of investigating CAVD pathogenesis in a sex-dependent manner to fully understand this disease and its mechanisms. These studies also support the creation of in vitro models of CAVD that account for sex-dependence, providing a more high-throughput way to investigate sex-related differences in disease progression than the use of animal models.

Transforming growth factor-beta 1 (TGF-β1) is a potential drug target for CAVD therapies. As a result, TGF-β1 is used in this study to explore how sex influences CAVD by the investigation of the sex-dependent response of quiescent VICs (qVICs) to TGF-β1 treatment [8, 9]. TGF-β1 has been demonstrated to increase VIC expression of myofibroblast characteristics such as alpha-smooth muscle actin (aSMA) expression, proliferation, and deposition of extracellular matrix proteins indicative of transdifferentiation of qVICs into activated VICs (aVICs) [8-11]. At high doses of TGF-β1, VICs have been shown to exhibit increased contractility, causing the formation of nodules and increased apoptosis [11]. This response to TGF-β1 leads to the development of dystrophic calcification within these nodules. TGF-β1 influences cellular behavior through interaction with its primary receptors, TGF-β receptor type I (TGFbR1)

and TGF-β receptor type II (TGFbR2). At the cell membrane, TGF-β binds to the extracellular matrix facing side of TGFbR1. TGFbR1 forms a heteromeric complex with TGFbR2, allowing for transphosphorylation of TGFbR1 by TGFbR2 and subsequent phosphorylation of SMADs by TGFbR1 within the cell [10]. A major pathway for downstream signaling of TGF-β includes phosphorylation of SMAD2/3 by the cytoplasmic domain of TGFbR1. Phosphorylated SMAD2/3 (pSMAD2/3) then binds with SMAD4 and translocates into the nucleus where it can promote gene transcription. Through this pathway TGF-β is able to promote phenotypic changes in VICs such as increases in the expression of extracellular matrix proteins such as collagen and fibronectin, increases in proliferation, and contractility associated with myofibroblastic transdifferentiation of VICs [10-14]. Therefore, this study looks at how male and female VICs differ both in their response to TGF-β1 and their sensitivity to the dose of TGF-β1, along with their expression of downstream SMADs.

6.3 Methods and Materials

All reagents used were purchased from Sigma Aldrich (St. Louis, MO) unless otherwise indicated.

6.3.1 VIC Isolation, Culture, and Treatment

Porcine hearts from male and female pigs were acquired from a local meat market (Hoesly's Meats, New Glarus, WI), and the aortic valve leaflets were removed to undergo VIC isolation as previously described. VICs were expanded on tissue culture polystyrene (TCPS) in low-glucose Dulbecco's Modified Eagle Medium (DMEM)

supplemented with 10% heat-inactivated fetal calf serum (FCS), 4 mM L-glutamine, and 150 U/mL penicillin/streptomycin. Once VICs reached 60-80% confluency, they were passaged onto dishes coated with 2 ug/cm^2 type-I bovine collagen (Advanced Biomatrix, Carlsbad, CA) and cultured in low-glucose DMEM supplemented with 2% FCS, 5.25 µg/mL insulin, 10 ng/mL FGF-2 (PeproTech, Rocky Hill, NJ), 4 mM L-glutamine, and 150 U/mL penicillin/streptomycin for 9 days to produce quiescent VICs (qVICs) as previously described. Cells were seeded at a density of 10,000 cells/cm^2 in low-glucose DMEM supplemented with 2% FCS, 4 mM L-glutamine, and 150 U/mL penicillin/streptomycin (Normal Media) for all experiments. Cell treatment with recombinant human transforming growth factor beta (TGF-β1) (Peprotech, Rocky Hill, NJ) was conducted 24 hours after seeding and refed with either 0 ng/mL, 0.1 ng/mL or 1 ng/mL TGF-β1 every 48 hours as needed.

Activated VICs (aVICs), a myofibroblast-like phenotype of VICs observed in valve repair and disease, were seeded in parallel with qVICS to compare the response of qVICs to treatment with TGF-β1, which has been shown to increase markers of myofibroblast differentiation. aVICs, which express high levels of myofibroblast markers such as increased ECM deposition and alpha-smooth muscle actin, were generated from the same population of cells isolated for differentiation into qVICs. These cells were passaged from the same dish of isolated VICs but were grown on uncoated TCPS in low-glucose DMEM supplemented with 10% FCS, 4 mM L-glutamine, and 150 U/mL penicillin/streptomycin without the addition of FGF-2 or insulin. These aVICs were seeded at the same density as qVICs and in normal media for all experiments.

6.3.2 Quantification of Proliferation

Cell proliferation was quantified using the Click-iT EdU Alexa Fluor 488 Imaging Kit (Invitrogen, Carlsbad, CA). Briefly, cells were treated with EdU for 12 hours followed by fixation with 10% neutral buffered formalin. After fixation, cells were permeabilized with 0.1% Triton X-100 in 1xPBS and treated with the Click-iT Alexa Fluor 488 reaction as per manufacturer instructions. Cells were counterstained with DAPI prior to fluorescent imaging using a Zeiss AX10 microscope (Jena, Germany). Fluorescent images were analyzed using ImageJ software (NIH) and percent proliferation was calculated by normalizing the VICs stained positively for EdU to the total number of cells determined by DAPI staining.

6.3.3 Quantification of Extracellular Matrix Deposition

Extracellular matrix deposition by VICs was quantified following 5 days of treatment with TGF-β1. Collagen I and fibronectin (FN) deposition were semi-quantitatively measured using immunocytochemical detection. Cells were fixed in 10% neutral buffered formalin followed by quenching of endogenous peroxidase activity with 0.3% hydrogen peroxide for one hour and overnight blocking at 4°C in 3% goat serum. Samples were then incubated for 2 hours at room temperature with a monoclonal rabbit anti-FN antibody (sc-9068, Santa Cruz Biotechnology, Dallas, TX, 1:1000 dilution) for FN quantification or a mouse monoclonal anti-collagen I antibody (ab6308, Abcam, Cambridge, MA, 1:1000 dilution) for collagen I quantification. Samples were washed with 1X PBS and then incubated for 40 min with a horseradish peroxidase linked goat anti-rabbit (65-6120,

Invitrogen, 1:1000 dilution) or anti-mouse (31430, ThermoFisher Scientific, Fitchburg, WI, 1;1000 dilution) secondary antibody to detect fibronectin or collagen I, respectively. After washing, samples were incubated in 1-Step Turbo-TMB ELISA substrate solution (ThermoFisher Scientific) for 25 minutes and stopped through the addition of 2N sulfuric acid (ThermoFisher Scientific). Color development was measured with a Tecan Infinite M1000 plate reader at 450nm with correction at 540nm. Background signal was determined by following the same procedure without incubating in primary antibody solution. Background absorbance was subtracted from these samples, and the corrected absorbance values were normalized to total cell number determined by DRAQ5 (Thermo Fisher) staining, which labels cell nuclei. Samples were stained for 20 min in DRAQ5 diluted 1:1000 in the absence of light. Samples were then rinsed once in 1X PBS before being read at 700nm using an Odyssey Infrared Imaging System (LiCor). Absorbance values are expressed as a fold-change compared to 0 ng/mL TGF-β treatment of female qVICs unless otherwise noted.

6.3.4 Quantification of VIC Phenotype and Extracellular Matrix via qRT-PCR

Quantitative reverse-transcription polymerase chain reaction (qRT-PCR) was used to evaluate markers of VIC phenotype (alpha-smooth muscle actin: *ACTA2*), expression of extracellular matrix proteins (collagen I: *COL1A1*), and expression of TGF-β receptor-1 (*TGFbRI*) following treatment with TGF-β1. Isolation of VIC RNA was conducted using the RNeasy Mini Kit (Qiagen, Hilden, Germany) per manufacturer instructions. Reverse transcription of RNA was conducted using a High Capacity cDNA Reverse Transcription kit (Applied Biosystems, Carlsbad, CA) and qRT-PCR was completed with TaqMan Gene Expression Assays (Applied Biosystems, Foster City, CA). Analysis was

conducted using the standard curve C_T method to allow for analysis across all conditions. Briefly, a set of standards from control samples were created for each gene and normalized to *GAPDH* expression. Data are expressed as fold-change compared to 0 ng/mL TGF-β treatment of female qVICs unless otherwise noted.

6.3.5 Quantification of Endogenous TGF-β1

Endogenous expression of TGF-β1 was measured in media from VICs cultured for 48 hours. A human TGF-β1 ELISA (R&D Systems) was used to quantify TGF-β1 concentration, and results were normalized to total protein content of each sample using the Micro BCA Assay (Pierce, Rockford, IL),

6.3.6 Intracellular TGF-β Pathway Signaling Quantification

Intracellular signaling by VICs was quantified following a 30-minute treatment with TGF-β. Total SMAD2/3 expression along with phosphorylation of SMAD2/3 and phosphorylation of p38MAPK was semi-quantitatively measured using ELISAs (Cell Signaling Technologies, Danvers, MA), following the manufacturer protocol. ELISAs were normalized to cell number through a quantification of double stranded DNA using a picogreen DNA assay (Thermo-Fisher, Waltham, MA).

6.3.7 Quantification of Endogenous Estradiol

Estradiol concentration in FCS and dextran-treated, charcoal-stripped FCS was determined via the Estradiol Parameter Assay Kit (R&D Systems). The values for

estradiol in FCS were not normalized to protein content since FCS is added to media by volume percentages.

6.3.8 Quantification of Receptor Expression via Western Blotting

Expression of estrogen receptor-α, androgen receptor, and TGF-β receptor type II were evaluated through western blotting. Cells were grown for 3 days prior to being lysed using a 2% sodium dodecyl sulfate lysis buffer, and cell number was quantified using the picogreen assay (Thermo-Fisher, Waltham, MA). Proteins were separated via gel electrophoresis on 4-12% Bis-Tris NuPage gels (Invitrogen). Following electrophoresis, proteins were transferred onto nitrocellulose membranes (LiCor). Membranes were blocked using Odyssey blocking buffer (LiCor) and probed with primary antibodies overnight at 4C with shaking. Estrogen receptor-α was detected using a polyclonal antibody produced in rabbit (ab75635, Abcam, diluted 1:500), androgen receptor was detected using a rabbit monoclonal antibody (ab133273, Abcam, diluted 1:500), and a rabbit polyclonal antibody was used to detect TGFbR2 (PA5-35076, Thermo Fisher, 1:1000). GAPDH and beta-tubulin were used as loading controls and detected using mouse monoclonal antibodies (Cell Signaling, diluted 1:1000). Following overnight incubation, membranes were washed in 1x PBS with 0.1% Tween-20 before being incubated while shaking for an hour at room temperature in IRDye 680 and 800 conjugated secondary antibodies diluted 1:10000. Membranes were washed again in 1x PBS with 0.1% Tween-20 before undergoing a final wash in 1x PBS to remove Tween-20 before imaging. Protein bands were imaged using the Odyssey Infrared Imaging

System (LiCor) at 700 nm and 800 nm. Protein was analyzed by normalizing the mean intensity of each band with the corresponding loading control prior to statistical analysis.

6.3.9 Statistics

Experiments were run with n=3 replicates. Data are expressed as mean ± standard deviation. Statistical analysis was conducted using GraphPad Prism software (GraphPad, LaJolla, CA). Statistical significance was determined through a one-way ANOVA and Tukey's posttest, with a P value less than or equal to 0.05 considered statistically significant.

6.4 Results

6.4.1 Sex-Related Phenotypic Responses of qVICs to TGF-β1 Treatment

As TGF-β has been shown to increase markers indicative of activated VICs, phenotypic markers such as proliferation and expression of *ACTA2*, the gene encoding for aSMA, were evaluated in both male and female qVICs at each level of TGF-β1 treatment. Female qVICs showed no change in proliferation across any treatment with TGF-β1 (Figure 6.1A). Male qVICs showed higher proliferation compared to females without TGF-β1 treatment (Figure 6.1A) along with increased proliferation at both the low dose of TGF-β1 and the high dose of TGF-β1. Cell area, an indicator of VIC activation, did not show any significant difference between males and females. Treatment with TGF-β1 did not alter cell area at either high or low dose. (Figure 6.1B). Analysis of *ACTA2,* however, showed an increase in both males and female upon treatment with TGF-β1

(Figure 6.1C). Female VICs only showed an increase in *ACTA2* at the highest level of TGF-β1 treatment while males showed increased *ACTA2* expression at the low dose of TGF-β1 (0.1 ng/mL) relative to no TGF-β1 treatment. This expression of *ACTA2* stayed constant even with increased TGF-β1 at the high dose (1 ng/mL). The consistent expression of *ACTA2* at a lower dose indicates males may have a lower threshold of TGFb1-induced activation compared to females.

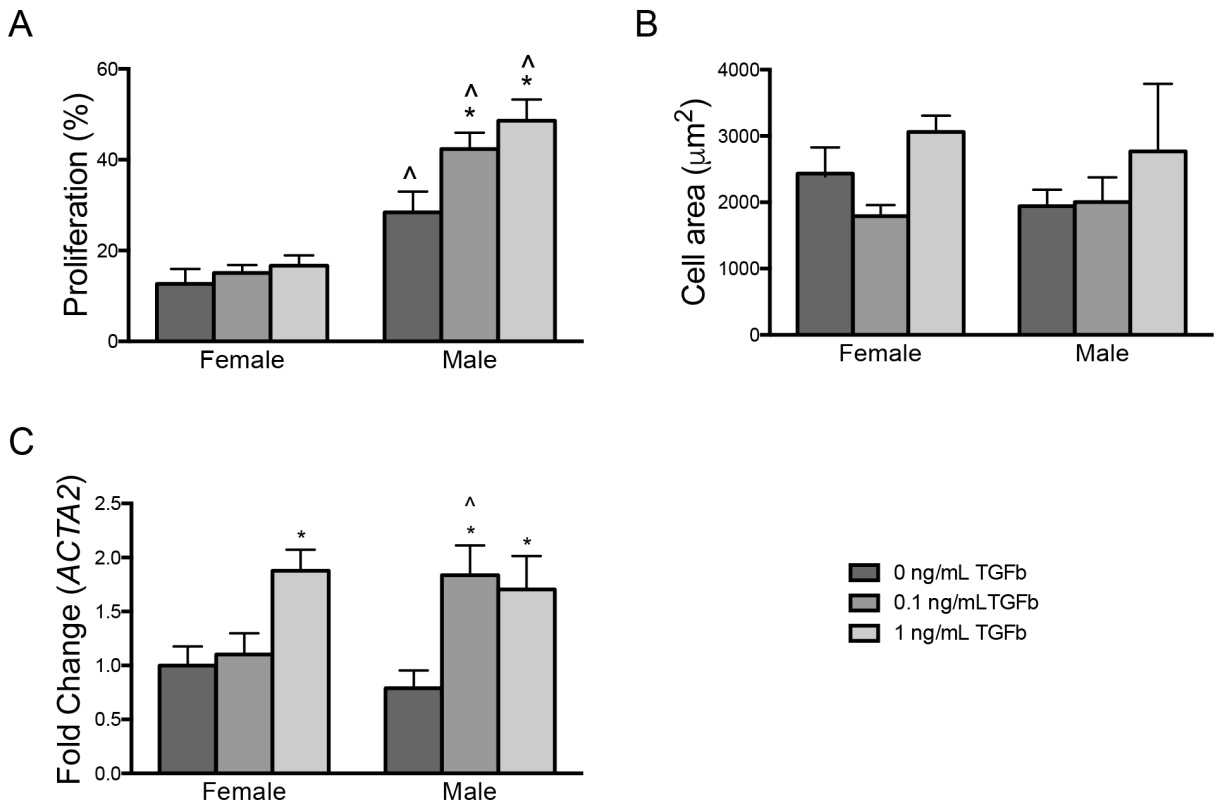

6.4.2 Sex-Related Differences in ECM Deposition

Activation of VICs is associated with extracellular matrix remodeling including deposition of ECM proteins such as collagen and fibronectin. Therefore, to evaluate the activation of qVICs following treatment with TGF-β1, the deposition of collagen I (Figure 6.2A) and

fibronectin (Figure 6.2B) was evaluated after 5 days. Female and male VICs both showed deposition of collagen and fibronectin in the absence of exogenous TGF-β1. Deposition of collagen I was increased in females treated with a high dose (1 ng/mL) of TGF-β1. Males however showed increased collagen I at both the low dose (0.1 ng/mL) and high dose (1 ng/mL) of TGF-β1, suggesting increased sensitivity to TGF-β1. Deposition of fibronectin by female VICs was constant across TGF-β1 treatments. Male VICs however, increased deposition of fibronectin at high doses of TGF-β1. Analysis of gene expression for *COL1A1* revealed a significant increase in expression in males compared to females across all TGF-β1 treatment conditions (Figure 6.2C). Expression

of *COL1A1* in males increased significantly at high (1 ng/mL) doses of TGF-β1 compared to untreated male qVICS. Females exhibited no change in *COL1A1* expression across TGF-β1 treatments, but aVICS exhibited a significant increase in *COL1A1* compared to all qVIC conditions, indicating the potential for further activation of females.

6.4.3 Stable Expression of TGF-b1 and TGF-β Receptors in VICs

Media levels of TGF-β1 were evaluated by ELISA to determine if VICs were exposed to different levels of TGF-β1 due to endogenous expression. Levels in both male and

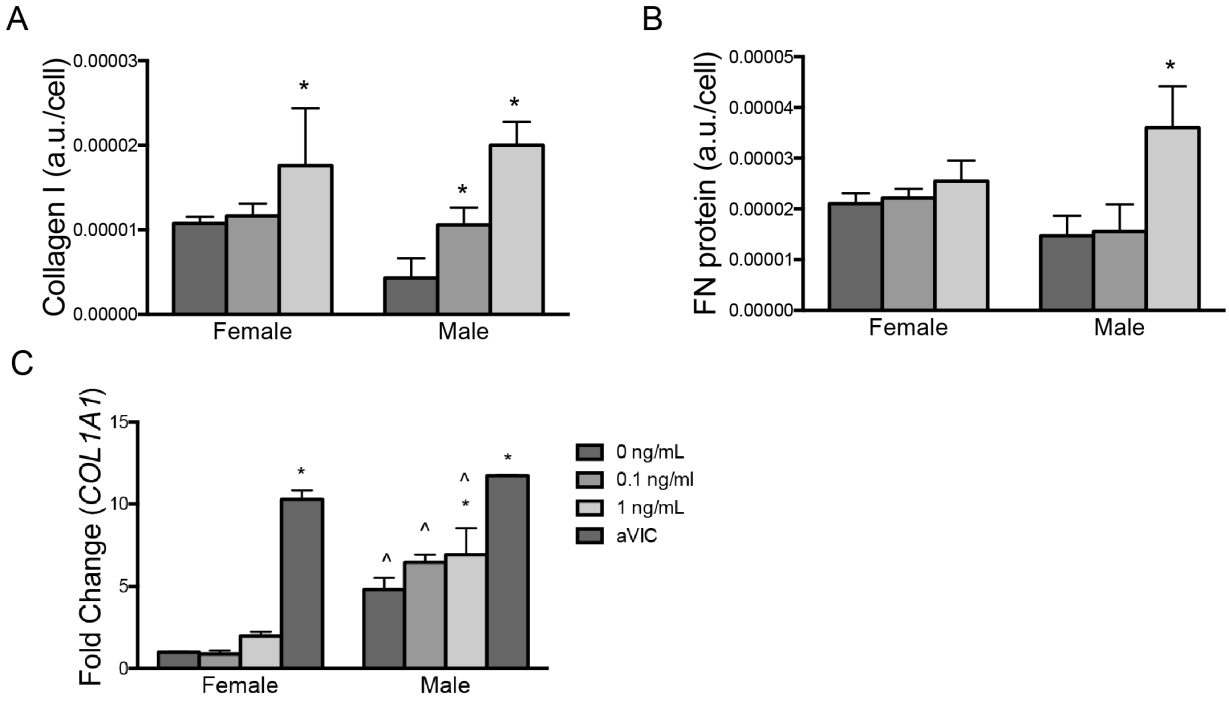

Figure 6.2 Sex dependent changes in ECM deposition. Expression of collagen I (A) and fibronectin (B). Gene expression of *COL1A1* (C) * = $p < 0.05$ compared to same sex without TGF-β1, ^ = $p < 0.05$ compared to females with same treatment condition. [Data shown in A and B were gathered by AM Porras, PhD and verified by HN Hutson]

female qVICs were below the detectable range, indicating that a negligible amount of TGF-β1 was being produced by the VICs themselves. To assess cellular recognition of exogenous TGF-β1, the relative expression of the two main receptors, TGFbR1 and TGFbR2 were evaluated. Protein expression of TGFbR2 was evaluated in untreated qVICs, qVICs treated with 1 ng/mL TGF-β1, and aVICs, which exhibit high levels of myofibrobastic markers (Figure 6.3). Expression of TGFbR2 was detectable in both males and females across all conditions (Figure 6.3A). However, no significant difference in expression of TGFbR2 was observed across sexes or TGFb treatment groups (Figure 6.3B). Gene expression of *TGFbR1* was evaluated through qRT-PCR due to non-specificity of TGFbR1 antibodies available for western blotting. Expression of *TGFbR1* was constant throughout all conditions in males (Figure 6.3C). Female aVICs, however, showed significantly higher expression of *TGFbR1* compared to untreated female qVICs. However, there were no significant differences between females and males.

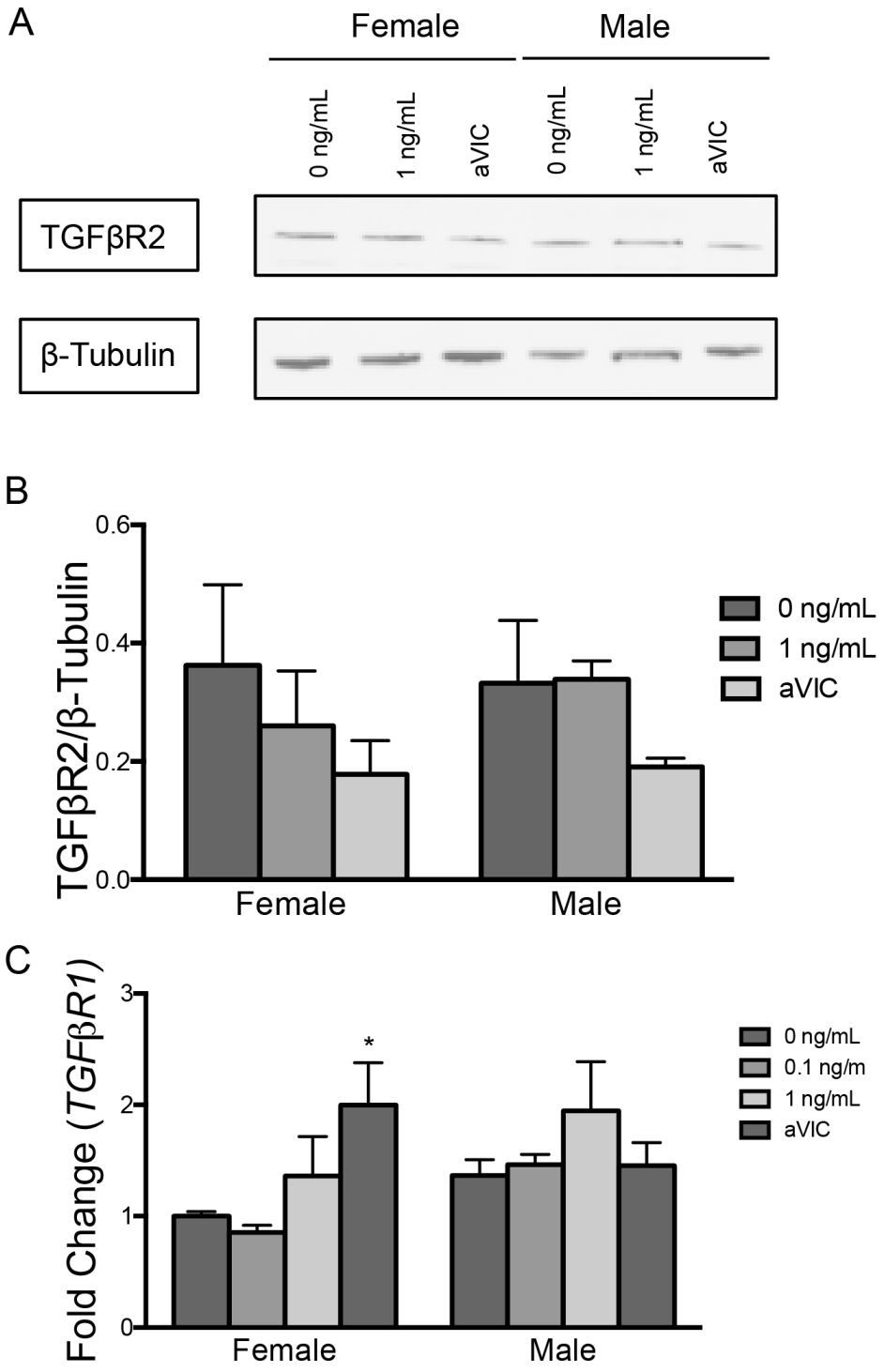

Figure 6.3 TGF-β1 receptor expression. Western blot showing expression of TGFbR2 (A) and quantification of blot (B). Gene expression of TGFbR1 (C). * = $p < 0.05$ compared to same sex without TGF-β1, ^ = $p < 0.05$ compared to females with same treatment condition.

6.4.4 Sex-Based Differences in Intracellular Signaling Following TGF-β1 Treatment

To understand the sex-related changes in phenotypic indicators and ECM deposition following TGF-β1 treatment, downstream signaling events within the TGF-β pathway were investigated. Analysis of pSMAD2/3 expression following 30-minute treatment with TGF-β1 revealed that while female and male expression of pSMAD2/3 in the absence of TGF-β1 was similar, males have an increased expression of pSMAD2/3 compared to females at both TGF-β1 concentrations (Figure 6.4A). Fold change in pSMAD2/3 over baseline expression was the same between males and females when normalized to initial concentration exhibited by qVICs without TGF-β1 treatment (Figure 6.4B). Analysis of pp33MAPk signaling, a secondary signaling pathway for TGF-β1, revealed no differences in activation between males and females following treatment (Figure 6.4C).

Analysis of total SMAD2/3 showed that across all treatment conditions males had almost twice as much total SMAD2/3 expression compared to females (Figure 6.4D). Both male and female VICs had no differences in total SMAD2/3 expression in response to any TGF-β1 treatments.

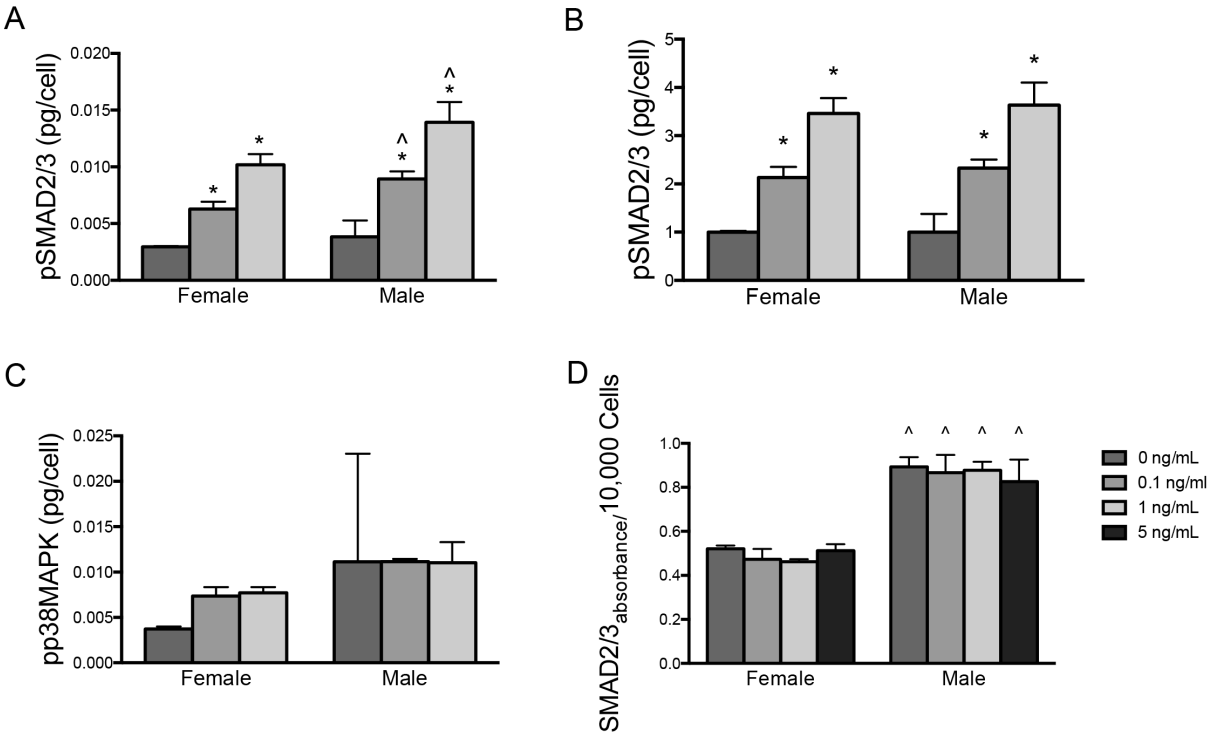

Figure 6.4 Sex-dependent expression of intracellular molecules. Expression of phosphorylated SMAD2/3 (A), Expression of phosphorylated SMAD2/3 normalized to 0 ng/mL TGF-β1 (B). Expression of phosphorylated p38MAPK (C) and total SMAD2/3 (D) following 30-minute treatment with TGF-β1. * = $p < 0.05$ compared to same sex without TGF-β1, ^ = $p < 0.05$ compared to females with same treatment condition.

6.4.5 Expression of Estrogen in Fetal Calf Serum

The content of estradiol, a major estrogen steroid, in the FCS stock used in our media was quantified due to the potential of estrogen signaling to alter SMAD2/3 expression [15, 16]. Dextran treated charcoal stripped FCS (CS-FCS), a FCS commonly used when conducting studies aimed at controlling the concentration of hormones in media, was tested as a potential option for future studies to investigate if sex differences occur in minimal concentration of estradiol (Figure 6.5). The FCS stock used in media had 117 ±

71.4 pg/mL estradiol, which was significantly more estradiol that the CS-FCS, which had 62.4 ± 8.45 pg/mL. This indicates that VICs were exposed to 2.34 ± 1.43 pg/mL estradiol during culturing. As estradiol levels in men and post-menopausal women typically ranges from 10 to 60 pg/mL; the concentration in VICs are exposed to is lower than that experienced in the body [17-19].

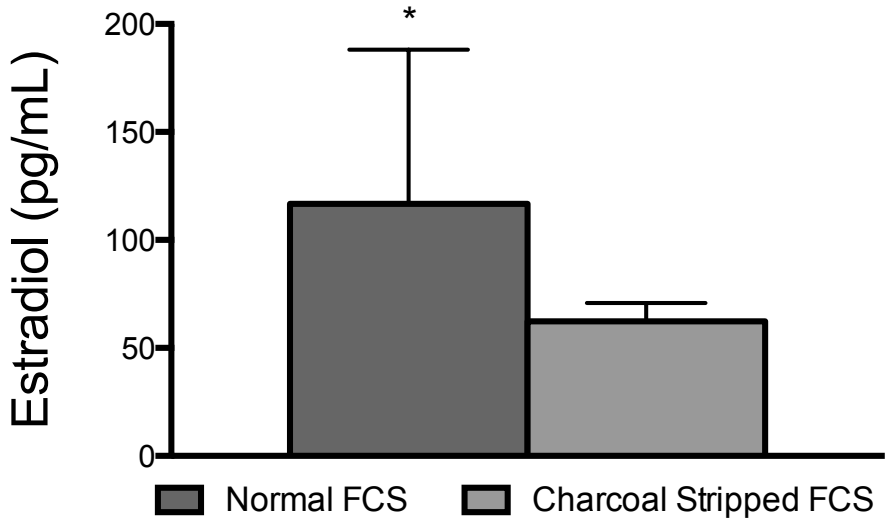

Figure 6.5 Estradiol content in FCS. * = $p < 0.05$ compared to CS-FCS

6.4.6 Expression of Hormone Receptors in VICs

While estradiol was present in the media, the ability of VICs to respond to this stimulus has not been demonstrated. Therefore, the expression of estrogen receptor-α (ERa) and androgen receptor (AR) were investigated. Both estrogen and androgen are classifications of hormones commonly implicated as factors for differences in males and females. The expression of estrogen receptor α (ERa) and androgen receptor (AR) were quantified through western blot (Figure 6.6A). Analysis of ERa showed an

increase in expression in female aVICs compared to qVICs. Meanwhile, no difference in expression of ERa was observed throughout male conditions (Figure 6.6B). No significant difference in ERa was measured between male and females across all conditions. Expression of AR (not shown) was not detectable via western blot.

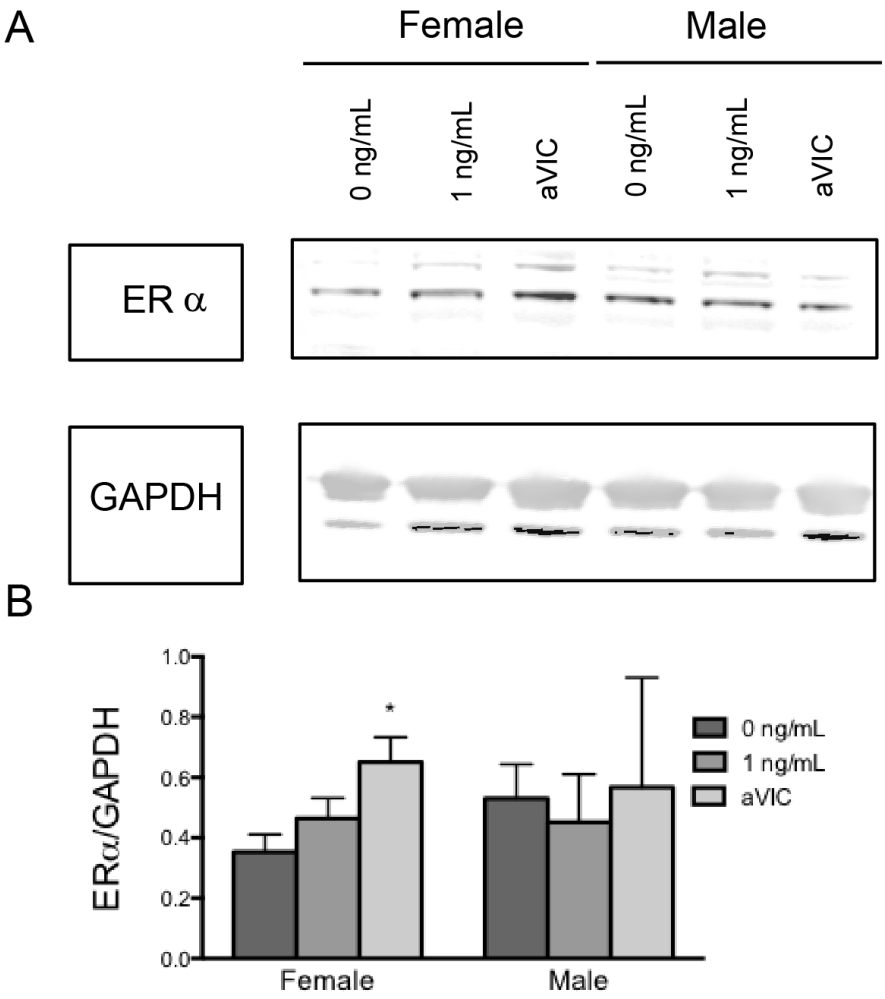

Figure 6.6 ERα expression. Western blot showing expression of ERα (A) and quantification (B). * = $p < 0.05$ compared to same sex without TGF-β1, ^ = $p < 0.05$ compared to females with same treatment condition.

6.5 Discussion

Previous studies have demonstrated the ability of TGF-β1 to induce phenotypic changes in many cell types, including VICs [10, 11, 20-22]. In VICs. TGF-β has been shown to promote myofibroblastic activation by increasing expression of aSMA, stimulating extracellular matrix deposition, and increasing VIC contractility [11, 15]. However, previous studies were not able to investigate the initiation of the transition from a quiescent to an activated phenotype. This is because, until recently [23, 24], the main *in vitro* models for investigating CAVD centered around the use of porcine VICs that were cultured in conditions that induce an activated VIC phenotype prior to experiment initiation. While these studies provide the basis for our current understanding of how stimulatory factors such as TGF-β1 alter VICs, they are limited in their ability to examine differentiation of VICs from their native, healthy state. Due to previous work characterizing the creation of qVICs *in vitro*, this study investigated the impact of TGF-β1 treatment on the initiation of VIC transition from quiescence to an activated phenotype. Also, previous investigations into the effect of TGF-β on VICs did not distinguish between different sexes during their investigations. Recent studies into the impact of sex on VIC response to osteogenic simulation have highlighted the sex-biased behavior of VICs *in vitro* [7]. Sex-related differences have also been reported in the gene expression in the aortic valve, with males exhibiting upregulation of a number of gene expression profiles associated with aortic valve disease compared to females [25]. Therefore, the information presented in this study provides insight into the role of TGF-β1 in earlier stages of VIC activation than have previously been investigated while accounting for sex-related differences in activation.

Despite the lack of significant differences in TGF-β1 receptor expression between males and females, male VICs presented higher sensitivity to TGF-β1 simulation. Males exhibited significantly higher proliferation compared to females and displayed dose-dependent responses to TGF-β1 simulation in their expression of *ACTA2.* These observations, along with the dose-dependent responses of males in deposition of collagen and fibronectin, suggest that males require a lower amount to TGF-β1 to undergo activation towards a myofibroblast phenotype. This is not to suggest that females do not undergo activation by TGF-β1, as demonstrated by their increase in fibronectin and 2-fold increase in *ACTA2* at a high dose of TGF-β1. However, it appears that females require a higher dose of TGF-β1 to significantly increase their expression of ECM proteins and *ACTA2* over their baseline expression. The differences observed in CAVD between sexes, with males having a higher risk compared to female, could be partially due to the increased sensitivity to TGF-β1 observed in males.

As endogenous expression of TGF-β1 by VICs was negligible, and males and females exhibited similar expression of TGF-β receptors, it was postulated that the differences observed in males and females were due to differences in downstream signaling in the TGF-β pathway. Analysis of phosphorylation of SMAD2/3, a major downstream pathway of TGF-β1 signaling, illustrated that both females and males exhibited a dose-dependent response. Overall levels of phosphorylated SMAD2/3 were greater in males compared to females only upon treatment of TGF-β1. As TGF-β signaling is being transmitted through similar levels of TGF-β receptors to cytoplasmic signaling

molecules, the increased expression of phosphorylated SMAD2/3 in males compared to females upon treatment suggests that the intracellular signaling response is higher in males compared to females. The significantly higher amount of total SMAD2/3 in males over females may be a factor in the ability of males to exhibit a higher signal through SMAD2/3 due to the increased availability of SMAD2/3 to phosphorylate. However, it is also possible that signaling through TGF-β receptors in females is activating a separate signaling pathway.

The significantly different expression of SMAD2/3 and phosphorylated SMAD2/3 observed between sexes could also indicate sex-dependent inhibition of this pathway in females. Previous studies have proposed that estrogen acts in a protective manner in the cardiovascular system by promoting inhibition or degradation of SMAD2/3 and SMAD4 [26]. The presence of a main form of estrogen, estradiol, in the FCS used for our experiments was determined to investigate the possibility of estrogen to impact our studies. Estradiol was indeed present in our FCS, and therefore in the media. As estrogen interacts with cells through two major receptors, estrogen receptor alpha (ERa) and estrogen receptor beta (ERb), differential expression of these receptors could impact cellular response to available estrogen. ERa has been proposed to be the major estrogen receptor involved in many cardiovascular pathologies, often in a protective manner [16, 27, 28]. Therefore, the expression of ERa was investigated. While ERa was present in both male and female VICs, there was no difference in expression between sexes. However, females did demonstrate an increase in the expression of ERa in the experimental control aVICs compared to untreated qVICs. This

supports the idea that females may increase expression of ERa due to higher activation levels of VICs. However, further investigation in needed fully understand the relationship between sex-based VIC activation and estrogen.

While this study provides novel insights into sex-based differences in VIC activation, many questions remain. Estrogen has been identified as a modulator of TGF-β1 signaling in many cell types. However, the role of estrogen in VIC behavior, especially as it pertains to sex differences in CAVD, is not fully understood. A study by Jiang, et al demonstrated the ability of estradiol to decrease the effects of TGF-β in myofibroblasts through modulation of SMAD signaling [26], suggesting that a similar mechanism may drive VICs that present a myofibroblast-like phenotype (aVICs). Other studies have indicated the modulate TGF-β signaling by estrogen occurs specifically through ERa-mediated degradation of SMAD2/3 [16]. While ERa has been a major focus of this paper and other investigations into the impact of estrogens on cardiovascular system, investigations into the role of ERb, which has been shown to inhibit cardiac fibrosis [28], are necessary to fully characterize the interaction between estrogen and VICs.

6.6 Conclusion

In this study, sex-related differences in VIC response to TGF-β were reported. Male VICs exhibited higher sensitivity to TGF-β1, expressing markers of myofibroblast activation such as ECM deposition and proliferation at lower doses of TGF-β1 compared to females. Male VICs also exhibited a significantly higher level of total SMAD2/3 compared to females across all conditions studied. The differences in total

SMAD2/3 between male and female VICs reported suggest degradation of SMAD2/3 via estrogen-related signaling as a potential mechanism driving sex-related differences in the CAVD initiation and progression. In order to fully understand the extent to which sex influences CAVD at the cellular level, further studies into the downstream TGF-β signaling pathway and the potential the role of estrogen in regulation of VIC behavior needs to be characterized

6.7 References

1. Lehmkuhl, V.R.-z.E. and M.O. Weickert, *Gender differences in the metabolic syndrome and their role for cardiovascular disease.* 2006. **147**: p. 136-147.
2. Simard, L., et al., *Sex-Related Discordance Between Aortic Valve Calcification and Hemodynamic Severity of Aortic Stenosis Is Valvular Fibrosis the Explanation ?* 2016.
3. Chen, J.-H. and C.a. Simmons, *Cell-matrix interactions in the pathobiology of calcific aortic valve disease: critical roles for matricellular, matricrine, and matrix mechanics cues.* Circulation research, 2011. **108**: p. 1510-24.
4. Sathyamurthy, I., et al., *Risk factor profile of calcific aortic stenosis.* Indian Heart Journal, 2016. **68**: p. 828-831.
5. Bonow, R.O., et al., *ACC/AHA 2006 Guidelines for the Management of Patients With Valvular Heart Disease: A Report of the American College of Cardiology/American Heart Association Task Force on Practice Guidelines (Writing Committee to Revise the 1998 Guidelines for the Manage.* Circulation, 2006. **114**: p. e84-e231.
6. Aggarwal, S.R., et al., *Sex Differences in Aortic Valve Calcification Measured by Multidetector Computed Tomography in Aortic Stenosis.* 2013: p. 40-48.
7. Masjedi, S., et al., *Sex-related differences in matrix remodeling and early osteogenic markers in aortic valvular interstitial cells.* Heart and Vessels, 2017. **32**: p. 217-228.
8. Stallons, M.V.G., et al., *Molecular Mechanisms of Heart Valve Development and Disease.* Etiology and Morphogenesis of Congenital Heart Disease, 2016: p. 145-151.
9. Wynn, T.a. and T.R. Ramalingam, *Mechanisms of fibrosis: therapeutic translation for fibrotic disease.* Nature Medicine, 2012. **18**: p. 1028-1040.
10. Ruiz-ortega, M., et al., *TGF- β signaling in vascular fibrosis.* 2018. **74**: p. 196-206.
11. Walker, G.a., et al., *Valvular myofibroblast activation by transforming growth factor-β: Implications for pathological extracellular matrix remodeling in heart valve disease.* Circulation Research, 2004. **95**: p. 253-260.

12. Grande-Allen, K.J., et al., *Glycosaminoglycan synthesis and structure as targets for the prevention of calcific aortic valve disease.* Cardiovascular research, 2007. **76**: p. 19-28.
13. Liu, A.C. and A.I. Gotlieb, *Transforming growth factor-beta regulates in vitro heart valve repair by activated valve interstitial cells.* The American journal of pathology, 2008. **173**: p. 1275-85.
14. Liu, A.C., V.R. Joag, and A.I. Gotlieb, *The emerging role of valve interstitial cell phenotypes in regulating heart valve pathobiology.* The American journal of pathology, 2007. **171**: p. 1407-18.
15. Conway, S.J., T. Doetschman, and M. Azhar, *The inter-relationship of periostin, TGF beta, and BMP in heart valve development and valvular heart diseases.* TheScientificWorldJournal, 2011. **11**: p. 1509-1524.
16. Ito, I., et al., *Estrogen Inhibits Transforming Growth Factor ␤ Signaling by.* 2010. **285**: p. 14747-14755.
17. GREENBLATT, R.B., M. OETTINGER, and C.S.S. BOHLER, *Estrogen-Androgen Levels in Aging Men and Women: Therapeutic Considerations.* Journal of the American Geriatrics Society, 1976. **24**: p. 173-178.
18. Jones, M.E., et al., *Changes in Estradiol and Testosterone Levels in Postmenopausal Women After Changes in Body Mass Index.* The Journal of Clinical Endocrinology & Metabolism, 2013. **98**: p. 2967-2974.
19. Jones, M.E., et al., *Reproducibility of estradiol and testosterone levels in postmenopausal women over 5 years: Results from the breakthrough generations study.* American Journal of Epidemiology, 2014. **179**: p. 1128-1133.
20. Park, S.O., et al., *ALK5- and TGFBR2-independent role of ALK1 in the pathogenesis of hereditary hemorrhagic telangiectasia type 2.* Blood, 2008. **111**: p. 633-642.
21. Peters, A.S., et al., *Cyclic mechanical strain induces TGFβ1-signalling in dermal fibroblasts embedded in a 3D collagen lattice.* Archives of Dermatological Research, 2015. **307**: p. 191-197.
22. Voloshenyuk, T.G., et al., *TNF-α increases cardiac fibroblast lysyl oxidase expression through TGF-β and PI3Kinase signaling pathways.* Biochemical and Biophysical Research Communications, 2011. **413**: p. 370-375.
23. Osman, L., et al., *Role of human valve interstitial cells in valve calcification and their response to atorvastatin.* Circulation, 2006. **114**: p. I547-52.
24. Porras, A.M., et al., *Robust Generation of Quiescent Porcine Valvular Interstitial Cell Cultures.* Journal of the American Heart Association, 2017. **6**: p. e005041.
25. McCoy, C.M., D.Q. Nicholas, and K.S. Masters, *Sex-related differences in gene expression by porcine aortic valvular interstitial cells.* PLoS ONE, 2012. **7**.
26. Jiang, H.S., et al., *Estradiol attenuates the TGF-β1-induced conversion of primary TAFs into myofibroblasts and inhibits collagen production and myofibroblast contraction by modulating the Smad and Rho/ROCK signaling pathways.* International Journal of Molecular Medicine, 2015. **36**: p. 801-807.
27. Heldring, N., et al., *Estrogen Receptors : How Do They Signal and What Are Their Targets.* Physiology Review, 2007. **87**: p. 905-931.

28. Pedram, A., et al., *Molecular and Cellular Endocrinology Estrogen receptor beta signals to inhibition of cardiac fi brosis.* Molecular and Cellular Endocrinology, 2016. **434**: p. 57-68.

CHAPTER 7: DEVELOPMENT OF AN *IN VITRO* MODEL OF THE AORTIC VALVE

7.1 Abstract

In vitro models are crucial tools for furthering our understanding of the pathology of numerous diseases and develop treatments. *In vitro* models are especially vital for investigations into the progression of calcific aortic valve disease (CAVD), where available human specimens are limited to end stages of the disease, when valve replacement occurs, or tissues acquired post-mortem. Despite the growing number of available models for CAVD, few existing models account for the interaction between valvular cell populations and the collagen fiber microarchitecture of the surrounding valve. The investigations detailed in this chapter aim to develop *in vitro* models for the study of architectural changes in collagen via the generation of 3D models of the collagen architecture native to human tissues. This chapter also explores age and disease related features of cultured valvular interstitial cells (VICs) such as expression of enzymatic crosslinkers and alpha smooth muscle actin (aSMA) to provide recommendations for matching VIC culturing techniques with the stages of CAVD they are intended to represent. Our findings suggest that cultures of quiescent VICs (qVICs) maintain their phenotype beyond a fourth passage, which was typically the end-point for use of VICs for *in vitro* studies. We also observed an increase in the expression of lysyl oxidase (LOX) and lysyl hydroxylase (PLOD1) by activated VICs (aVICs) with higher passaging. Glycation of methacrylated gelatin as a potential *in vitro* model of an aging ECM environment was reported along with successful fabrication of 3D scaffolds that

mimic the collagen microarchitecture of the human valve. These platforms provide new avenues of investigations into the interaction between VICs and their ECM environments.

7.2 Introduction

Calcific aortic valve disease (CAVD) is a highly prevalent condition in the United States, impacting the life of 1 out of 4 people over the age of 65 [1-3]. Yet, due to difficulties investigating the pathology of this disease in humans and issues with the ability of animal models to fully reproduce this disease[4, 5], the mechanisms which drive the initiation and development of CAVD remain unclear. Nevertheless, aspects of CAVD pathogenesis have been uncovered through the use of *in vitro* models [6-8]. Previous models using porcine derived aortic valve interstitial cells, VICs [6, 9-13], have demonstrated the capacity of *in vitro* VIC models to provide meaningful insights into the response of VIC populations to various stimuli native to healthy and diseased aortic valves [7, 8, 11, 14, 15]. Identification of extracellular matrix (ECM) dysfunction as a hallmark of CAVD has also led to *in vitro* investigations into the role of ECM components native to the healthy and diseased valve in directing VIC phenotype [7, 8, 16]. While available *in vitro* models of the aortic valve have yielded crucial data, many aspects of these models have not been characterized. For example, very little is known about the proliferation, doubling time, and aSMA expression of VICs after four passages. Furthermore, the majority of previous *in vitro* models of the ECM have been limited to adsorption of ECM proteins onto tissue culture polystyrene (TCPS) or hydrogels [17], which do not account for the 3D microarchitecture of the valve.

Therefore, in this chapter we aim to further characterize existing *in vitro* models of VICs to advance our understanding of their characteristics and generate new models of the ECM that account for the molecular and structural characteristics of the valve ECM.

A highly utilized *in vitro* model of VICs involves isolation of the cells from porcine aortic valves and culturing of them directly on TCPS in high glucose media [18]. This method produces VICs that displayed a highly myofibroblastic phenotype, classifying them as activate VICs (aVICs) [18-20]. While these models readily reflect the aVIC phenotype observed in aortic valves in response to pathological injury or disease, they were not able to produce the quiescent phenotype (qVICs) observed in healthy valves. Therefore, these models were not suited for investigations into early stages of CAVD, when transdifferentiation of qVICs to aVICs is thought to occur [14, 19]. Use of these VIC models is limited to only a handful of passages (typically four to six) for every batch of cells isolated from the porcine valve due to alterations in their doubling time and morphology. However, the nature of these alterations of VICs has not been fully investigated. Recently, a new model of VICs has been reported that allows for generation of a qVIC phenotype in culture through a decrease in glucose and supplementation of media with beta fibroblast growth factor (bFGF) and insulin [21, 22]. This model addresses the limitation of the previous aVIC model by allowing investigations into the response of qVICs to pathological stimuli, yet similarly the stability of this model over multiple passages has not been evaluated. The studies presented in this chapter work to address these limitations by evaluating aVICs and

qVICs past the point of typical use for markers of disease and phenotypic activation, respectively.

As ECM disarray is a hallmark for CAVD [23], *in vitro* models that accurately mimic the valve ECM are necessary for complete exploration of CAVD pathology. As stated previously, current ECM models are limited to adsorbed ECM proteins and hydrogel systems that, while effective, do not address molecular and architectural changes in the valve such as those reported in Chapter 3[24] and Chapter 5. We therefore explored generation of *in vitro* systems that mimic the collagen microarchitecture of the valve and address differences in the glycation of the ECM proteins that occur with aging, a major risk factor for CAVD. Our intention is to create models of the ECM that match the glycation level and architectural characteristics of human valves that are healthy, diseased, and at risk for CAVD. Our investigations focused on creation of a model of non-enzymatic glycosylation prevalent in the valve across different ages through the treatment of a mechanically tunable methacrylated gelatin (GelMA) system [25] with glycation promoting sugars (beta D-glucose). We separately assessed the ability of this GelMA system in combination with a previously defined 3D printing system [26-28] to be utilized to mimic the microarchitectural characteristics of the diseased (Chapter 3) and aged (Chapter 5) valve.

7.3 Methods and Materials

All reagents used were purchased from Sigma Aldrich (St. Louis, MO) unless otherwise indicated.

7.3.1 VIC Isolation and Culture for Evaluation of LOX and PLOD1 synthesis

Porcine hearts from male pigs were acquired from a local meat market (Hoesly's Meats, New Glarus, WI), and the aortic valve leaflets were removed to undergo isolation of vascular interstitial cell (VICs) as previously described. For studies utilizing only aVICs, VICs were expanded on tissue culture polystyrene in Media 199 supplemented with 10% fetal calf serum (FCS), 2 mM L-glutamine, and 150 U/mL penicillin/streptomycin. VICs were refed every 48 hours until reaching 60-80% confluence, at which point they were passaged or seeded for experiments. For analysis of LOX and PLOD1 expression VICs were seed at every passage, through passage 8 on TCPS at a density of 10,000 cells/cm^2 and cultured for 5 days before being fixed with 10% formalin.

7.3.2 VIC Isolation and Culture for Remaining Studies

Due to the recent development of a method for culturing quiescent VICs (qVICs), the majority of the studies were conducted using this new culturing method. For the remaining studies, male VICs were expanded on tissue culture polystyrene (TCPS) in low-glucose Dulbecco's Modified Eagle Medium (DMEM) supplemented with 10% heat-inactivated fetal calf serum (FCS), 4 mM L-glutamine, and 150 U/mL penicillin/streptomycin. Once VICs reached 60-80% confluency, they were passaged onto dishes coated with 2 ug/cm^2 type-I bovine collagen (Advanced Biomatrix, Carlsbad, CA) and cultured in low-glucose DMEM supplemented with 2% FCS, 5.25 µg/mL insulin, 10 ng/mL FGF-2 (PeproTech, Rocky Hill, NJ), 4 mM L-glutamine, and 150 U/mL penicillin/streptomycin for 9 days to produce quiescent VICs (qVICs) as

previously described. Cells were seeded in low-glucose DMEM supplemented with 2% FCS, 4 mM L-glutamine, and 150 U/mL penicillin/streptomycin (Normal Media) at a density of 10,000 cells/cm^2 for all experiments unless otherwise noted. Cells were refed every 48 hours for evaluation of alpha smooth muscle actin (aSMA) and *ACTA2.* For calculation of doubling time, cells were refed every 24 hours to eliminate changes in doubling of VICs due to media depletion.

Direct exposure of cells to advanced glycation end products (AGEs) was achieved through incorporation of AGE modified bovine serum albumin (AGE-BSA). Cell treatment with AGE-BSA was conducted 24 hours after seeding at a density of 50,000 cells/cm^2. AGE-BSA was added to media at a concentration of 200 μg/mL as references in previous studies [29, 30]. BSA (Thermo Fisher Scientific Waltham, MA) was used as a vehicle control to ensure any differences observed were due to AGEs. Following treatment, cells were evaluated for expression of aSMA.

Activated VICs (aVICs), a secondary VIC phenotype involved in active valve repair and disease development, were seeded in parallel with qVICS to establish their interaction with constructed GelMA models. These cells were passaged from the same dish of isolated VICs but were grown on uncoated TCPS in low-glucose DMEM supplemented with 10% FCS, 4 mM L-glutamine, and 150 U/mL penicillin/streptomycin without the addition of FGF-2 or insulin. These aVICs were seeded similarly to qVICs, at the same density and refed in the same manner using Normal Media for all experiments.

7.3.3 Evaluation of Increased Passaging on aVIC expression of Crosslinking Enzymes

LOX and PLOD1 expression were semi-quantitatively measured using immunocytochemical detection. Cells fixed in 10% neutral buffered formalin were treated with 0.3% hydrogen peroxide for one hour to quench any endogenous peroxidase activity before undergoing blocking in 3% goat serum overnight. Samples were then incubated with anti-PLOD1 or anti-LOX antibodies (described in Chapter 3 and 5) for 2 hours. Samples were washed with 1X PBS and then labeled with a horseradish peroxidase linked goat anti-rabbit secondary antibody (described in Chapter 3 and 5) for 40 min. After washing, samples were incubated in 1-Step Turbo-TMB ELISA substrate solution (ThermoFisher Scientific, Fitchburg, WI) for 5 minutes and stopped through the addition of 2N sulfuric acid (ThermoFisher Scientific Waltham, MA). Color development was measured with a Tecan Infinite M1000 plate reader. Background signal was determined by following the same procedure without incubating in primary antibody solution. Background absorbance was subtracted from the samples, and the corrected absorbance values were normalized to total cell number determined by staining of cell nuclei using DRAQ5.

7.3.4 Quantification of qVIC expression of ACTA2 Over Increased Passaging on via qRT-PCR

Quantitative reverse-transcription polymerase chain reaction (qRT-PCR) was used to evaluate the VIC phenotype marker alpha-smooth muscle actin (*ACTA2*). Isolation of VIC RNA was conducted using the RNeasy Mini Kit (Qiagen, Hilden, Germany) per

manufacturer instructions. Reverse transcription of RNA was conducted using a High Capacity cDNA Reverse Transcription kit (Applied Biosystems, Carlsbad, CA), and qRT-PCR was completed with TaqMan Gene Expression Assays (Applied Biosystems, Foster City, CA). Analysis was conducted using the $\Delta\Delta C_T$ method and normalized to *GAPDH* expression. Data are expressed as fold-change compared to passage 2 (P2).

7.3.5 Immunocytochemical Detection of aSMA expression in VICs

Detection of aSMA in VICs was completed via immunocytochemical techniques. VICs were fixed in 10% buffered formalin solution, followed by at 20 min incubation in 0.1% Triton X-100 to permeabilize cells. Cells were blocked in 3% goat serum for 1 hour at room temperature and then incubated with a monoclonal mouse primary anti-aSMA antibody (clone 1A4, 1:500 dilution) overnight at 4°C. Cells were then washed 4 times in 1x PBS before being incubated in a 1% goat serum solution with goat anti-mouse AlexaFluor 488 (Invitrogen, 1:1000) followed by 4 additional 1x PBS washes and counterstaining with DAPI (1:1000) for 20 min. Fluorescent images were taken using a Zeiss AX10 fluorescence microscope.

7.3.6 Synthesis of Methacrylated Gelatin

Porcine gelatin was methacrylated as previously described by Loessner et al[25]. Briefly, gelatin from porcine skin was dissolved in 1x PBS warmed to 50°C at 10% w/v and stirred until dissolved. Methacrylic anhydride (MA) was added at a rate of 200 μL/min to a final concentration of 5% v/v for creation of hydrogels and 10% v/v for 3-D fabrication. Methacrylation of gelatin continued overnight at 50°C under gentle stirring.

The methacrylated gelatin solution was then centrifuged at 3500xg for 5 minutes, and the collected supernatant was diluted 1:4 in 1x PBS prior to being placed in 12-14 kDa MWCO dialysis tubing (Thermo Fisher, Waltham, MA). The synthesized GelMA solution was dialyzed against a 10-fold excess (v/v) of 1x PBS for three days to remove any unreacted chemicals followed by dialysis against deionized water for two days to remove PBS. Dialyzed GelMA was sterile filtered and flash frozen in liquid nitrogen before undergoing lyophilization for a minimum of five days. GelMA was stored at -20°C until use.

7.3.7 Glycation of GelMA via Treatment with beta D-Glucose

GelMA was treated with 250 mM β D-Glucose in 1xPBS in an attempt to increase the level of glycation in the gelatin structure for investigations into the interactions between protein glycation and VICs. GelMA gels were also treated with 250 mM sucrose, a non-reducing sugar, as a control for the influence of sugar concentration on cell phenotype. GelMA hydrogels were generated through photopolymerization following addition of 0.05% w/v of the photoinitiator lithium arylphosphonate (LAP) [31] and exposure to 365 nm light for 10 min.

GelMA was treated both prior to crosslinking and after hydrogel formation (Figure 7.1) as previous studies into non-enzymatic glycation of collagen indicated a difference in final glycation of collagen based upon the initial state of collagen when exposed to sugars[32]. Following pre-treatment, GelMA was incubated at 37°C for 5 days to ensure GelMA stayed in solution during glycation. Following pre and post treatment, prepared

hydrogels were soaked in 1x PBS overnight to ensure consistent swelling and removal of excess sugars.

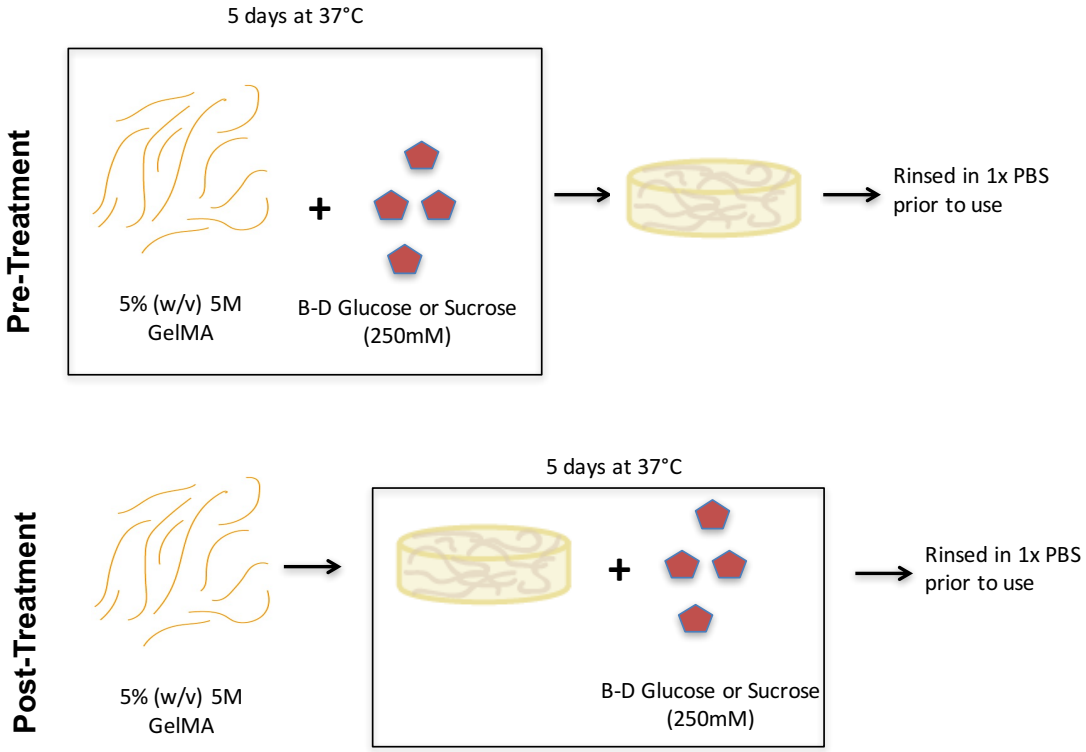

Figure 7.1 Schematic of treatment of GelMA to increase glycation.

7.3.8 Mechanical Evaluation of GelMA

The mechanical properties of GelMA, (pre- or post-treated with D-glucose or sucrose) were determine through dynamic mechanical analysis performed using an MTS Insight 5 instrument (MTS, Eden Prairie MN). GelMA was treated as described previously and disks 8 mm in diameter and 2 mm thick were tested at room temperature. Stress-strain curves were obtained at a frequency of 1 Hz and used to calculate the elastic modulus.

7.3.9 Evaluation of Glycation of Treated GelMA via ELISA

The concentration of AGEs in treated GelMA was conducted by digesting hydrogels in proteinase K followed by use of the OxiSelect™ Advanced Glycation End Product AGE Competitive ELISA kit (Cell Biolabs, Inc, San Diego, CA), per the manufacturer instructions. Concentration of AGEs reported were normalized to protein content using a Micro BCA Assay kit (Thermo Fisher Scientific, Waltham, MA)

7.3.10 Creation of 3-D Printed Model of Collagen Architecture

3-D GelMA scaffolds were fabricated using a previously defined 3D multiphoton excited fabrication system[26, 33]. A solution of 15% w/v of GelMA was created with the photoinitiator Rose Bengal (1 mM) and loaded into a SecureSeal™ hybridization chambers (GBL621505) on siliconized slides for fabrication. Fabrication was based on 8-bit 3D .bmp images files created from second harmonic generation microscopy images of human valves that were acquired during previous studies (Chapter 3). These

images were processes through ImageJ (NIH) using the Threshold and Tubeness functions to create distinct architecture during fabrication.

Following fabrication, the hybridization chamber was removed through a 15 min incubation in deionized water heated to 47°C. Following removal of the chamber, excess GelMA was removed by a second 15 min incubation in 47°C deionized water. The fabricated structure was photobleached for 45 min at 1W to inactivate excess Rose Bengal. Structures were sterilized by UV treatment for 1 hour prior to seeding of VICs.

7.3.11 Imaging of Live Cells on Fabricated Structure

VICs were seeded on prepared 3D fabricated structures to verify the ability of these structures to sustain cell viability. VICs were seeded at a density of 500,000 cells/cm^2 to ensure maximum interaction of VICs with the structure. Four hours after seeding, media was changed to remove any VICs that had failed to adhere. VICs were then cultured for 24 hours before being stained for viability using 2 μM calcein AM (Thermo Fisher Scientific). VICs were images 30 min after treatment with calcein AM using a Zeiss AX10 fluorescence microscope.

7.3.12 Statistics

Experiments were run with n = 3 replicates unless otherwise noted. Data are expressed as mean ± standard deviation. Statistical analysis was conducted using GraphPad Prism software (GraphPad, LaJolla, CA). Statistical significance was determined

through a one-way ANOVA and Tukey's posttest, with a P value less than or equal to 0.05 considered statistically significant.

7.4 Results

7.4.1 Maintenance of Phenotype Across High Passages of qVICs

Generation of quiescent VICs has recently been reported [21, 22]. However, it is unclear how long these cells maintain their quiescent phenotype upon extended culturing. To investigate the extended culturing potential of qVICs, expression of *ACTA2* and aSMA were quantified along with qVIC doubling time. Analysis of *ACTA2* (Figure 7.2A) and aSMA (Figure 7.2C), markers for qVIC transdifferentiation into myofibroblast-like activated VICs (aVICs), revealed a consistent expression through 9 passages. Doubling time of qVICs (Figure 7.2B) also showed no significant change with increased passaging. This suggests that the quiescent phenotype can be maintained *in vitro* for longer than previously characterized.

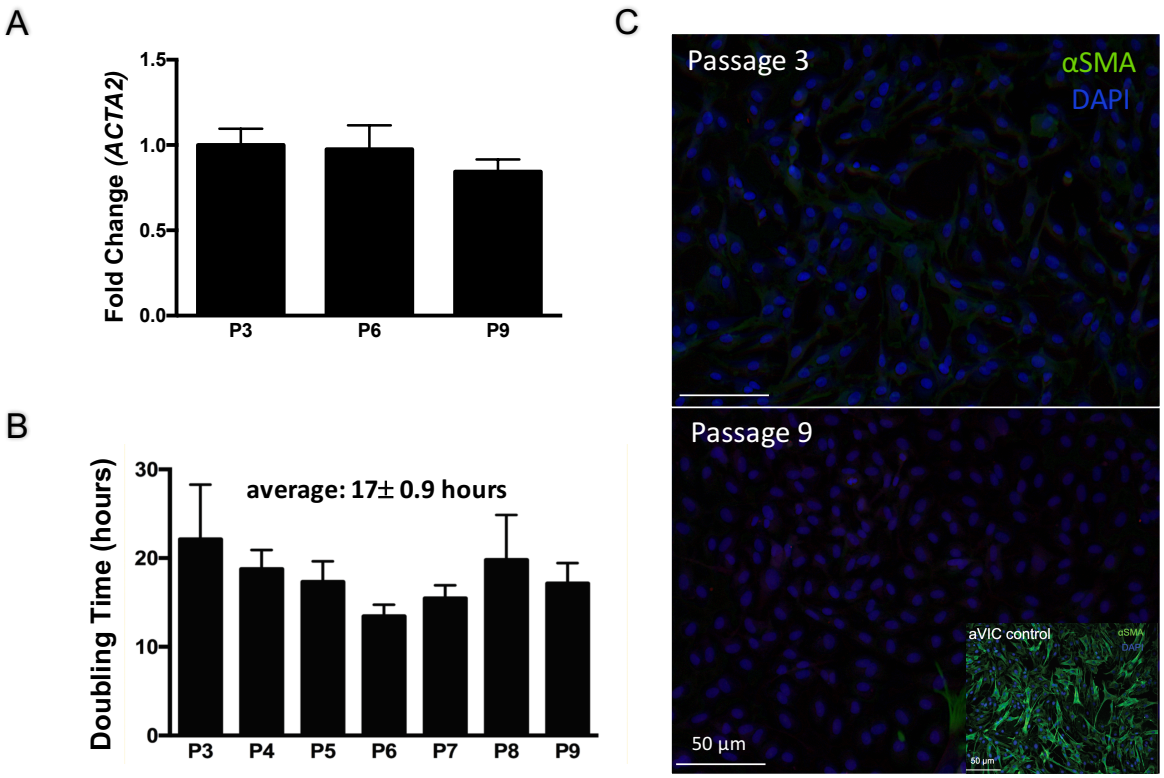

Figure 7.2 qVIC Phenotype Across High Passages Expression of *ACTA2* (A), doubling time (B) and expression of aSMA (C) in qVICs from passage 3 to passage 9. Scale bar = 50 µm.

7.4.2 Expression of Crosslinking Enzymes with High Passage of aVICs

Extracellular matrix disarray is a hallmark of CAVD that has been discussed in previous chapters [23]. Lysyl oxidase (LOX), an enzymatic crosslinker important in collagen maturation [34], has been shown to increase in localized areas of the aortic valve with disease [24]. In order to create an *in vitro* model to explore changes in the expression of crosslinking enzymes, the expression of LOX and PLOD1, a secondary enzyme involved in collagen crosslinking, in male aVICs was investigated. Male aVICs were cultured for a longer period of time than the typical passage 4 to investigate if increased passaging would result in an *in vitro* model of aVICs that exhibited CAVD-related changes in the expression of LOX. Male aVIC expression of both LOX and PLOD1

were measured at each passage (Figure 7.3) until passage 8 (P8). LOX and PLOD1 expression increased in late passages of VICs, with LOX expression significantly higher by passage 6 (Figure 7.3A) and aVICS showing a significant increase in expression of PLOD1 as early as passage 4 (Figure 7.3B).

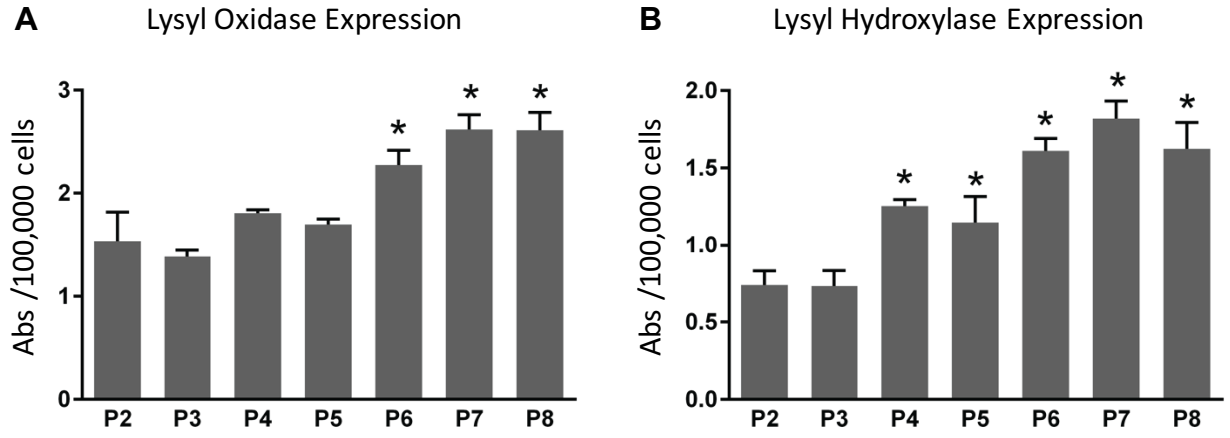

Figure 7.3 Expression of LOX and PLOD1 in High Passage aVICs Expression of LOX (A) and PLOD1 (B) in aVICs from passage 2 to passage 8. * = $p < 0.05$ compared to passage 2.

7.4.3 Direct Treatment of qVICs with AGEs

As discussed in Chapter 6, changes in the content of AGEs occurred with aging of the aortic valve in humans, a major risk factor for CAVD. To investigate the impact of different concentrations of AGEs on the phenotype of the qVIC population in healthy valves, we directly treated cells with AGE-BSA and imaged expression of aSMA. However, as shown in Figure 7.4, both AGE-BSA and the vehicle control of BSA only resulted in expression of aSMA. Therefore, we could not conclusively determine whether AGEs were responsible for the expression of aSMA observed in qVICS.

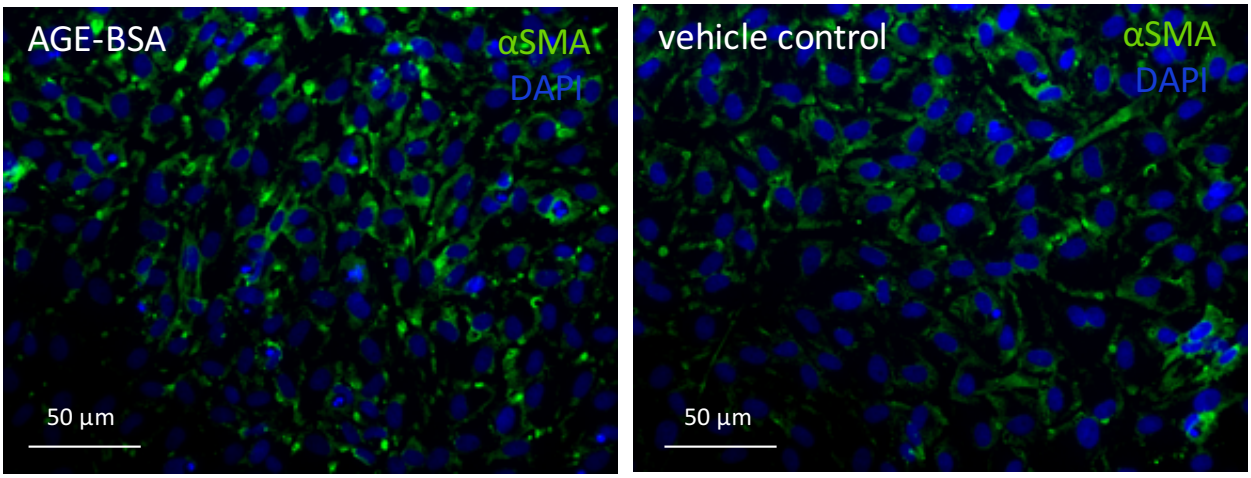

Figure 7.4 Expression of aSMA in qVICs following AGE-BSA treatment. qVICs treated with AGE-BSA (left) and BSA control (right) stained for aSMA (green) and counterstained with DAPI (blue). Scale bar = 50 µm.

7.4.4 AGE Content of GelMA Following Treatment with D-Glucose

As AGEs are typically a component of the ECM, investigations into AGE modifications to ECM components of the valve was investigated. GelMA was synthesized to act as a model for collagen in the valve ECM. As modifications to the structure of collagen can result in changes to its mechanical properties [35, 36], GelMA was used instead of collagen due to the ability to tune the mechanical properties. VICs have been shown to be sensitive to changes in the mechanical properties of their environment [11, 23], and using GelMA would allow for adjustment of scaffold mechanics through adjustments in the level of methacrylation to compensate for any changes resulting from glycation without changing the gelatin content. While post-treatment with D-glucose to GelMA hydrogels did not alter the content of AGEs in the hydrogel (Figure 7.5), pre-treatment of GelMA (before crosslinking) resulted in over twice the level of AGEs compared to

untreated GelMA. However, this investigation was only conducted on a single gel in each condition, so it cannot be determined if this change was statistically significant.

7.4.5 Mechanical Differences In GelMA Due To Non-Enzymatic Glycation

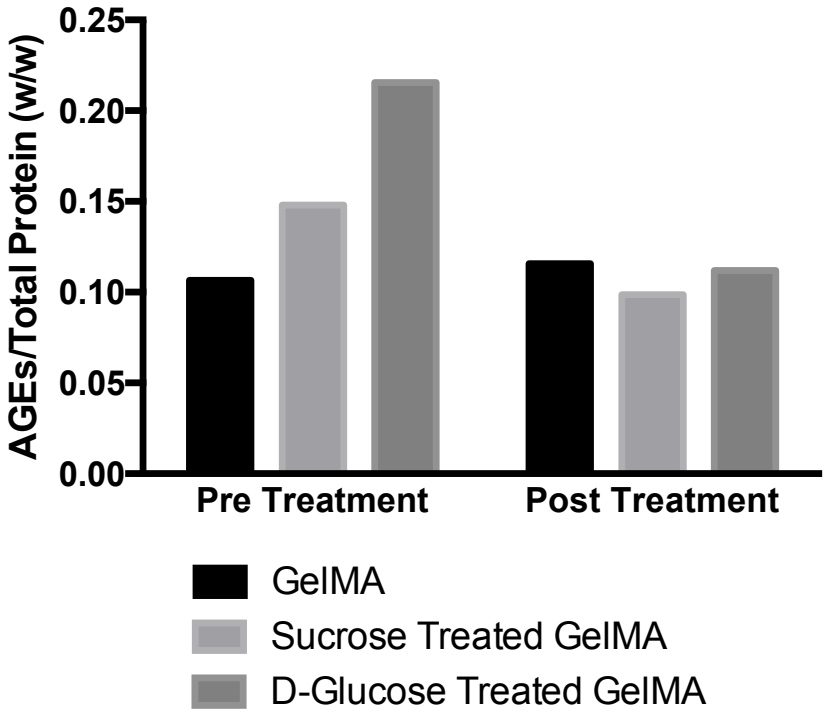

Figure 7.5 AGE content of treated GelMA * = $p < 0.05$, n = 1.

The mechanical properties of GelMA hydrogels treated with D-glucose were determined to ensure constant substrate stiffness across all conditions for future *in vitro* studies (Figure 7.6). Pre-treatment with D-glucose resulted in a significant decrease in stiffness compared to GelMA controls, while post-treatment did not. This could be the result of glycation levels reported in Figure 7.5 decreasing the efficiency of GelMA crosslinking. However, a decrease in the stiffness of untreated GelMA was observed between pre-

and post-treatments, suggesting the method of treatment may alter the mechanic of GelMA, irrespective of glycation level.

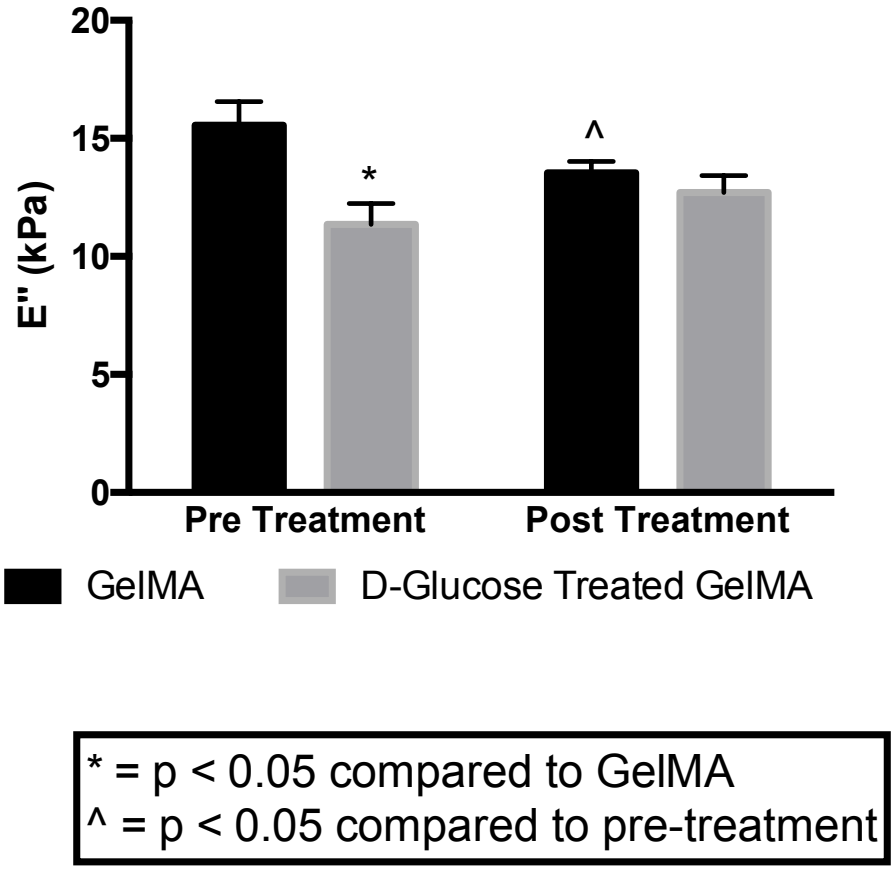

Figure 7.6 Mechanical Properties of treated GelMA * = p < 0.05, n = 3.

7.4.6 Fabrication Of 3D Scaffolds That Mimic Aortic Valve Collagen Architecture

While glycation of GelMA provides a method for altering the molecular structure of gelatin to which VICs is exposed, it does not offer a way to tailor the topographical characteristics of the biomaterial. To create a hydrogel system aimed at mimicking the architectural differences observed in the collagen structure in Chapter 3 and 5, 3D fabrication was attempted (Figure 7.7). SHG images obtained from previous investigations of diseased valve collagen structure (Figure 7.7A) were used as the input image files for creating 3D printing of GelMA (Figure7.7B). As shown in Figure 7.7C-D, this method was able to mimic the texture shown in Figure 7.7A and recreate a 3D structure based on SHG image z-stacks. This method was also able to successfully create models of a healthy human valve fibrosa (not shown).

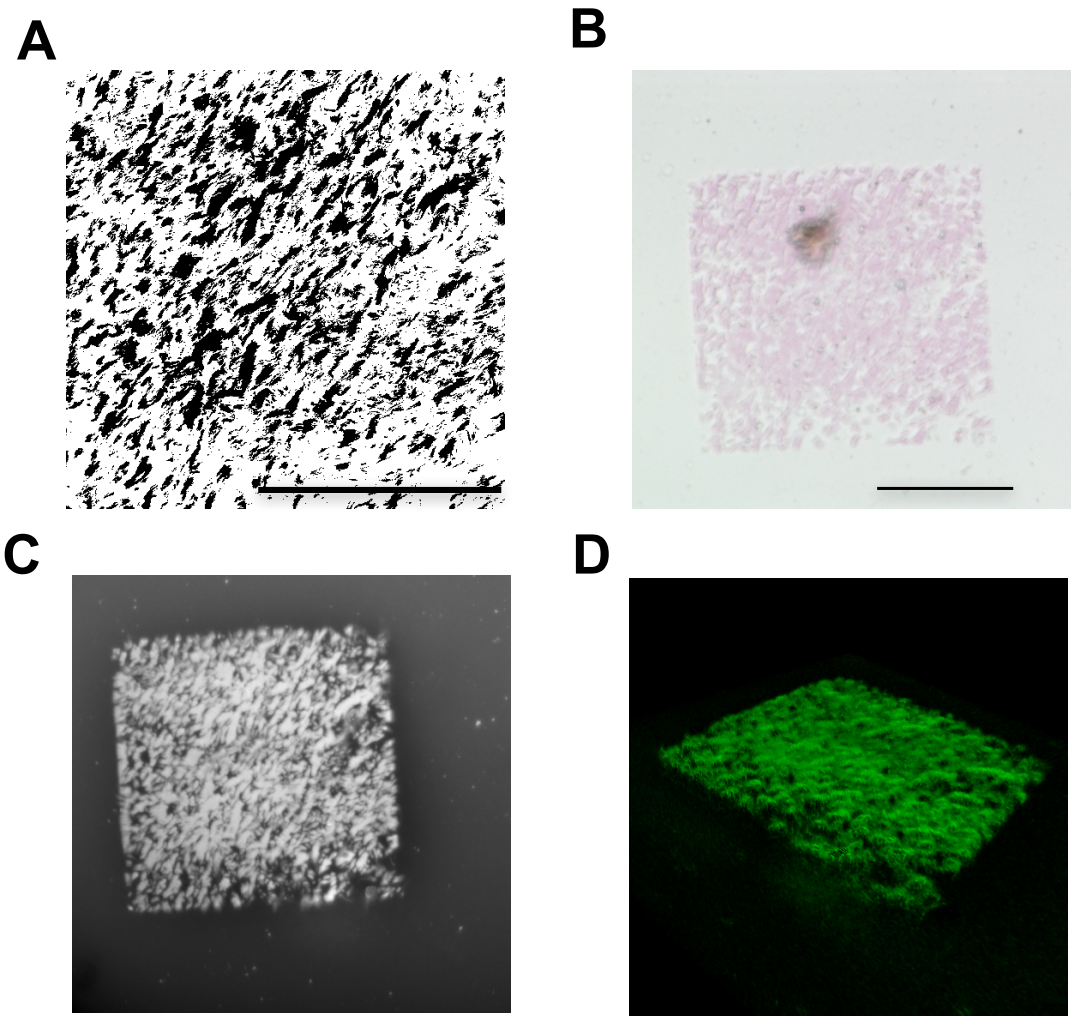

Figure 7.7 Fabrication of 3D scaffolds SHG input image of diseased valve architecture (A), Bright field image of fabricated structure (B). Z-projection (C) and view (D) of 3D scaffold. Scale bar = 100 μm.

7.4.7 Successful Culturing Of VICs On Fabricated Scaffolds

Following successful fabrication of GelMA scaffolds representing human valve collagen components, VICs were seeded onto these structures to ensure this method did not adversely affect VIC viability (Figure 7.8). Bright field images of structures of healthy (Figure 7.8A) and diseased (Figure 7.8B) valves were taken to observe VIC interaction and morphology. Calcein AM staining of VICs revealed cells seeded on these scaffolds

were viable. In places where VICs infiltrated the scaffolds (represented by arrows) changes in cell morphology were observed which were not present without the fabrication of structures (Figure 7.8C).

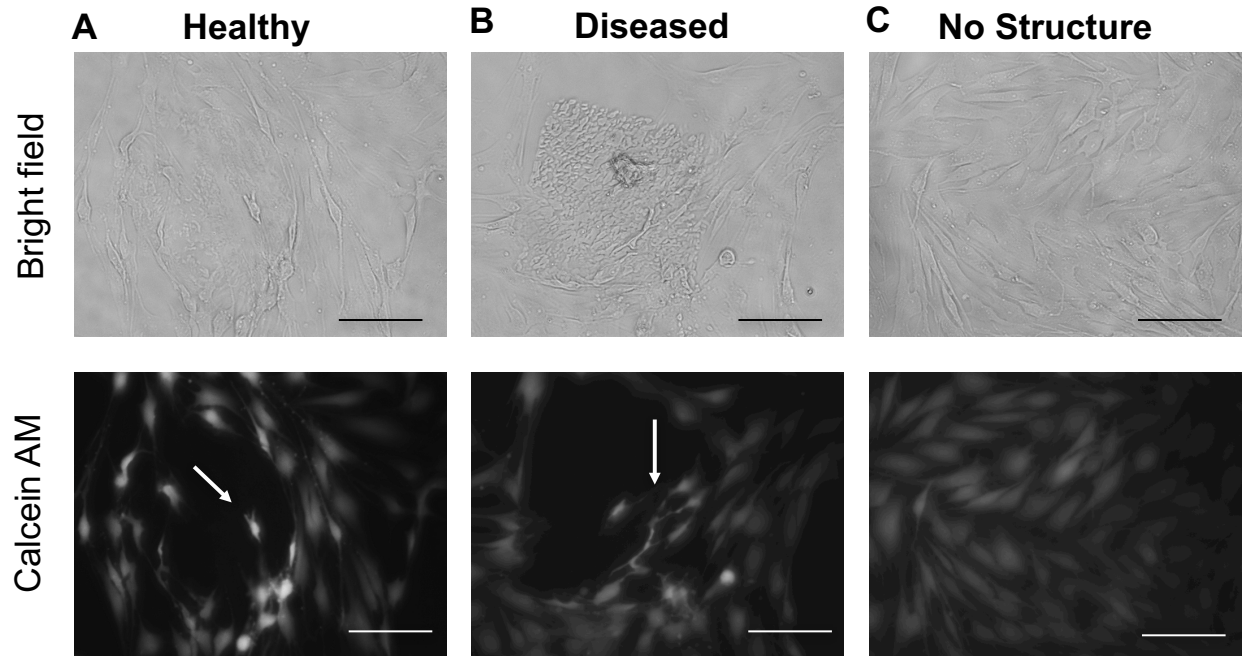

Figure 7.8 VIC interaction with 3D scaffolds Bright field and fluorescent images of VICs seeded on 3D scaffold of heathy (A) and diseased (B) valve architecture. Seeding in absence of 3D structure (C) shown for comparison. Scale bar = 100 μm.

7.4.8 VICs Interact with Large 3D Fabricated Structures

To verify that this fabrication method could be used to recreate large [AGAIN - WHAT DO YOU MEAN BY 'LARGE'??] structures of the aortic valve fibrosa, 3D scaffold superstructures composed of multiple adjacent scaffolds were fabricated and seeded with VICs. Figure 7.9 shows the ability of VICs to interact with these structures and penetrate the entire width.

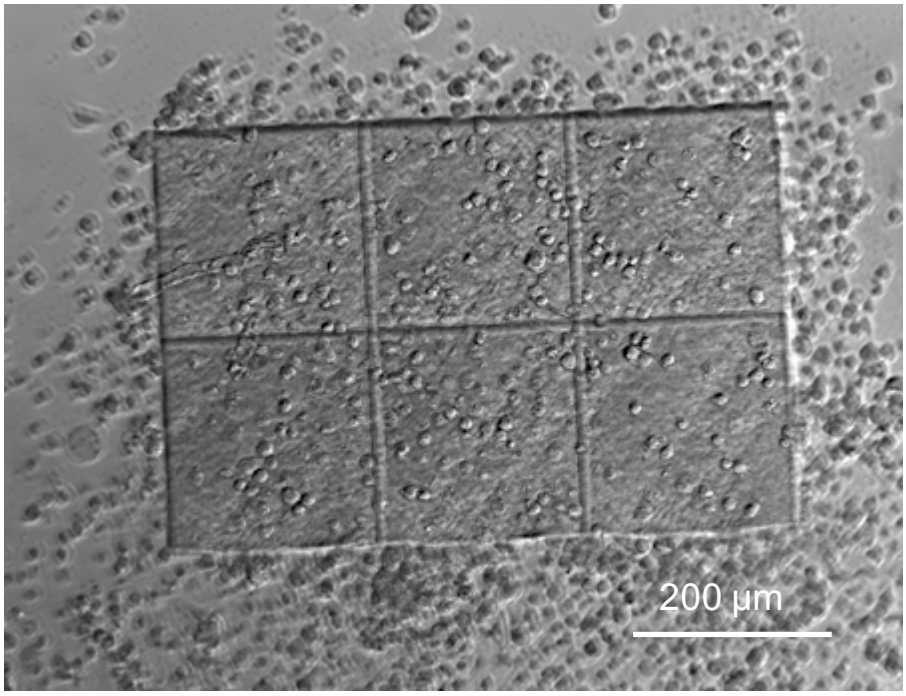

Figure 7.9 VICs seeded in 3D superstructure. Scale bar = 200 µm

7.5 Discussion

In vitro models of the aortic valve are essential for furthering our understanding of the progression of aortic valve disease (CAVD). Previous models aimed at understanding the relationship between the aortic valve interstitial cell population, VICs [9], and aspects of the ECM [7, 8] have demonstrated their capacity to provide meaningful insights into the pathogenesis of CAVD. However, many aspects of these models have not been characterized. For example, typical culturing of VICs for investigations into their role in CAVD is ended after four or six passages due to observed changes in their growth and behavior. However, these changes have not been characterized. This is true

for newly developed models of quiescent VICs (qVICs) as well [9, 22]. In this chapter, we explored aVICs and qVICs passaged past the point of standard use for changes in their expression of crosslinking enzymes and transdifferentiation, respectively. aVICs displayed an increase in LOX and PLOD1 with higher passaging. As LOX has been implicated as a factor in late stages of CAVD [24], higher passaged aVICs may provide a new model for investigations into the CAVD-related remodeling of collagen in the valve. While an increase in PLOD1 expression has not been observed in CAVD, this model could also provide new insights into the role of PLOD1 expression by aVICs in the aortic valve. However, further investigations into the characteristics of this model, including evaluation of the expression of myofibroblast markers and proliferative ability, need to be examined before this model can be recommended.

Assessment of the consequences of increased passaging on qVIC phenotype revealed that qVICs sustained a quiescent phenotype over extended passages. Markers of qVIC activation remained negligible through passage 9 and doubling time was consistent. This observation supports the use of qVICs for a longer period of time than previously examined and provides a distinction between the responses of aVICs and qVICs to extended passaging.

As accumulation of AGEs have been implicated in age-related changes in the ECM of a variety of tissues [37-40], and differences in AGE content in the valve was reported in Chapter 5, we investigated the response of VICs to AGEs. We initially investigated this interaction through direct treatment of VICs with AGE-BSA in an attempt to negate any

compounding factors such as changes in presentation and mechanical cues associated with cell responses to AGEs in an ECM environment. However, VIC response to the AGE delivery method (BSA) was to significant to directly assess the effect of AGEs. We therefore moved to a GelMA hydrogel system.

While glucose-based glycation of collagen has been reported [41], to our knowledge the ability to glycate methacrylated gelatin has not been investigated. GelMA was investigated due to the ability to modify its mechanical properties without altering the concentration of bioactive molecules presented to cells during culturing [25, 42]. Our preliminary investigations showed an increase in AGE content following pre-treatment of GelMA with glucose. However, an increase in AGE content was not observed in the post-treatment system. The difference in formation of AGEs could be due to a decrease in the ability of glucose to covalently bond with available gelatin proteins in GelMA once the photopolymerization has occurred due to a low diffusion of glucose into the structure. Differences in the mechanical properties of hydrogels following treatment support the idea that pre-treatment resulted in differential glycation compared to post-treatment. Increased AGE content in pre-treated GelMA resulted in a decrease in stiffness, which is in contrast to previous studies where increased glycation was associated with an increase the stiffness of collagen rich tissues [35, 43]. It is possible that the differences in glycation-induced mechanics of the gels were due to glycation impeding the photopolymerization of available methacryloyl groups in GelMA. Despite differences in mechanical properties between the untreated and pre-treated GelMA hydrogels, this system is still viable for comparison of VICs on GelMA with varying

levels of glycation as the mechanical contribution of GelMA can be altered by varying the level of methacrylation, allowing for comparison of mechanically similar hydrogels. As AGEs were successfully created in GelMA, this protocol for creating AGEs could be incorporated into the GelMA based systems for the fabrication of 3D scaffolds also discussed in this chapter.

Recent studies have indicated CAVD-related changes in the collagen architecture of the valve [24], which have yet to be evaluated for their role in regulation to VIC phenotypes. We utilized 3D fabrication, in combination with GelMA, to recreate the collagen architecture of healthy and diseased human valves as a platform for investigating the influence of these structures on VICs. As these structures were successfully created and VICs displayed viability upon seeding into these structures, this system can be readily used for future studies that explore VIC response to CAVD- and age-related changes in collagen architecture.

The studies described in this chapter, while many are still preliminary, offer a basis for the creation of many new *in vitro* models that incorporated newly defined aspects of the collagen structure in the valve. Together with new characterizations of previously defined VIC culturing methods, the findings in this chapter provide the foundation for future studies that match VICs of different phenotype and passage with the related collagen architecture and modification to create *in vitro* models of the aortic valve across different human ages and disease stages.

7.6 Conclusion

We demonstrated that newly defined culture models of qVICs maintain their quiescent phenotype longer than previously known. Extended passaging of aVICs also revealed increases in the expression of collagen crosslinking enzymes previously observed in diseased human valves. These studies provide the foundation for creation of *in vitro* culturing models of VICs that mimic different stages of aortic valve growth, age, and pathology. A hydrogel system for increasing the glycation of gelatin while retaining mechanical properties was also generated and evaluated for its potential use as a model targeted at investigating the interaction between age- or CAVD-related post-translational modifications to the ECM and VICs. The successful incorporation of VICs into scaffolds generated through previously described 3D fabrication techniques supported the use of these techniques in studying microarchitectural characteristics of the aortic valve.

7.7 References

1. Sathyamurthy, I., et al., *Risk factor profile of calcific aortic stenosis.* Indian Heart Journal, 2016. **68**: p. 828-831.
2. Rosenhek, R., et al., *Mild and moderate aortic stenosis. Natural history and risk stratification by echocardiography.* European heart journal, 2004. **25**: p. 199-205.
3. Akat, K., M. Borggrefe, and J.J. Kaden, *Aortic valve calcification: basic science to clinical practice.* Heart (British Cardiac Society), 2009. **95**: p. 616-623.
4. Porras, A.M., et al., *Development of Aortic Valve Disease in Familial Hypercholesterolemic Swine: Implications for Elucidating Disease Etiology.* Journal of the American Heart Association, 2015. **4**: p. e002254.
5. Sider, K.L., M.C. Blaser, and C.a. Simmons, *Animal models of calcific aortic valve disease.* International journal of inflammation, 2011. **2011**: p. 364310.
6. Walker, G.a., et al., *Valvular myofibroblast activation by transforming growth factor-β: Implications for pathological extracellular matrix remodeling in heart valve disease.* Circulation Research, 2004. **95**: p. 253-260.

7. Rodriguez, K.J. and K.S. Masters, *Regulation of valvular interstitial cell calcification by components of the extracellular matrix.* Journal of biomedical materials research. Part A, 2009. **90**: p. 1043-53.
8. Rodriguez, K.J., L.M. Piechura, and K.S. Masters, *Regulation of valvular interstitial cell phenotype and function by hyaluronic acid in 2-D and 3-D culture environments.* Matrix biology : journal of the International Society for Matrix Biology, 2011. **30**: p. 70-82.
9. Osman, L., et al., *Role of human valve interstitial cells in valve calcification and their response to atorvastatin.* Circulation, 2006. **114**: p. I547-52.
10. Yip, C.Y.Y., et al., *Inhibition of pathological differentiation of valvular interstitial cells by C-type natriuretic peptide.* Arteriosclerosis, thrombosis, and vascular biology, 2011. **31**: p. 1881-9.
11. Yip, C.Y.Y., et al., *Calcification by valve interstitial cells is regulated by the stiffness of the extracellular matrix.* Arteriosclerosis, thrombosis, and vascular biology, 2009. **29**: p. 936-42.
12. Gu, X. and K.S. Masters, *Role of the MAPK/ERK pathway in valvular interstitial cell calcification.* American journal of physiology. Heart and circulatory physiology, 2009. **296**: p. H1748-57.
13. Gu, X. and K.S. Masters, *Role of the Rho pathway in regulating valvular interstitial cell phenotype and nodule formation.* American journal of physiology. Heart and circulatory physiology, 2011. **300**: p. H448-58.
14. Yip, C.Y.Y. and C.a. Simmons, *The aortic valve microenvironment and its role in calcific aortic valve disease.* Cardiovascular pathology : the official journal of the Society for Cardiovascular Pathology, 2011. **20**: p. 177-82.
15. Rodriguez, K.J., et al., *Manipulation of valve composition to elucidate the role of collagen in aortic valve calcification.* BMC cardiovascular disorders, 2014. **14**: p. 29.
16. Gu, X. and K.S. Masters, *Regulation of valvular interstitial cell calcification by adhesive peptide sequences.* Journal of biomedical materials research. Part A, 2010. **93**: p. 1620-30.
17. Benton, J.a., B.D. Fairbanks, and K.S. Anseth, *Characterization of valvular interstitial cell function in three dimensional matrix metalloproteinase degradable PEG hydrogels.* Biomaterials, 2009. **30**: p. 6593-603.
18. Bowler, M.a. and W.D. Merryman, *In vitro models of aortic valve calcification: solidifying a system.* Cardiovascular pathology : the official journal of the Society for Cardiovascular Pathology, 2014: p. 1-10.
19. Chester, A.H. and P.M. Taylor, *Molecular and functional characteristics of heart-valve interstitial cells.* Philosophical transactions of the Royal Society of London. Series B, Biological sciences, 2007. **362**: p. 1437-1443.
20. Taylor, P.M., et al., *The cardiac valve interstitial cell.* The international journal of biochemistry & cell biology, 2003. **35**: p. 113-8.
21. Latif, N., et al., *Modulation of Human Valve Interstitial Cell Phenotype and Function Using a Fibroblast Growth Factor 2 Formulation.* 2015: p. 1-19.
22. Porras, A.M., et al., *Robust Generation of Quiescent Porcine Valvular Interstitial Cell Cultures.* Journal of the American Heart Association, 2017. **6**: p. e005041.

23. Chen, J.-H. and C.a. Simmons, *Cell-matrix interactions in the pathobiology of calcific aortic valve disease: critical roles for matricellular, matricrine, and matrix mechanics cues.* Circulation research, 2011. **108**: p. 1510-24.
24. Hutson, H.N., et al., *Calcific Aortic Valve Disease Is Associated with Layer-Specific Alterations in Collagen Architecture.* Plos One, 2016. **11**: p. e0163858.
25. Loessner, D., et al., *Functionalization, preparation and use of cell-laden gelatin methacryloyl-based hydrogels as modular tissue culture platforms.* Nature Protocols, 2016. **11**: p. 727-746.
26. Ajeti, V., et al., *Image-inspired 3D multiphoton excited fabrication of extracellular matrix structures by modulated raster scanning.* 2013. **21**: p. 25346-25355.
27. Basu, S., et al., *Multiphoton Excited Fabrication of Collagen Matrixes Cross-Linked by a Modified Benzophenone Dimer : Bioactivity and Enzymatic Degradation.* 2005: p. 1465-1474.
28. Pitts, J.D., et al., *New photoactivators for multiphoton excited three-dimensional submicron cross-linking of proteins: bovine serum albumin and type 1 collagen.* Photochemistry and photobiology, 2002. **76**: p. 135-144.
29. Ge, J., et al., *Advanced glycosylation end products might promote atherosclerosis through inducing the immune maturation of dendritic cells.* Arteriosclerosis, Thrombosis, and Vascular Biology, 2005. **25**: p. 2157-2163.
30. Isoda, K., et al., *AGE-BSA decreases ABCG1 expression and reduces macrophage cholesterol efflux to HDL.* Atherosclerosis, 2007. **192**: p. 298-304.
31. Fairbanks, B., et al., *Photoinitiated polymerisation of PEG-diacrylate with lithium phenyl-2,4,6-trimethylbenzoylphosphinate: polymerisation rate ans cytocompatibility.* Biomaterials, 2009. **30**: p. 6702-6707.
32. Mason, B.N., et al., *Tuning three-dimensional collagen matrix stiffness independently of collagen concentration modulates endothelial cell behavior.* Acta Biomaterialia, 2013. **9**: p. 4635-4644.
33. Sridhar, M., et al., *Construction of a laser scanning microscope for multiphoton excited optical fabrication Construction of a laser scanning microscope for multiphoton excited optical fabrication.* 2016. **3474**.
34. Aslam, T., et al., *Optical molecular imaging of lysyl oxidase activity – detection of active fibrogenesis in human lung tissue.* Chem. Sci., 2015. **6**: p. 4946-4953.
35. Reddy, G.K., L. Stehno-Bittel, and C.S. Enwemeka, *Glycation-induced matrix stability in the rabbit achilles tendon.* Archives of biochemistry and biophysics, 2002. **399**: p. 174-180.
36. Reiser, K.M., M. Amigable, and J.A. Last, *Nonenzymatic Glycation of Type I Collagen.* 1992. **4**.
37. Dworatzek, E., I. Baczko, and G. Kararigas, *Effects of aging on cardiac extracellular matrix in men and women.* Proteomics - Clinical Applications, 2016. **10**: p. 84-91.
38. Jacob, M.P., *Extracellular matrix remodeling and matrix metalloproteinases in the vascular wall during aging and in pathological conditions.* Biomedicine & pharmacotherapy = Biomédecine & pharmacothérapie, 2003. **57**: p. 195-202.
39. Jaisson, S. and P. Gillery, *Evaluation of Nonenzymatic Posttranslational Modification-Derived Products as Biomarkers of Molecular Aging of Proteins.* Clinical Chemistry, 2010. **56**: p. 1401-1412.

40. Silver, F.H., et al., *Physiology of Aging Invited Review : Role of mechanophysiology in aging of ECM : effects of changes in mechanochemical transduction.* 2003. **08854**: p. 2134-2141.
41. Francis-Sedlak, M.E., et al., *Characterization of type I collagen gels modified by glycation.* Biomaterials, 2009. **30**: p. 1851-1856.
42. Berger, A.J., et al., *Decoupling the effects of stiffness and fiber density on cellular behaviors via an interpenetrating network of gelatin-methacrylate and collagen.* Biomaterials, 2017. **141**: p. 125-135.
43. Reddy, G.K., *Cross-Linking in Collagen by Nonenzymatic Glycation Increases the Matrix Stiffness in Rabbit Achilles Tendon.* Experimental diabesity research, 2004. **5**: p. 143-153.

CHAPTER 8: CONCLUSIONS AND RECOMMENDATIONS

8.1 Conclusions

Despite the reported occurrence of calcific aortic valve disease (CAVD) in a quarter of the population over the age of 65, the initiation and progression of this disease is not fully understood [1, 2]. While the progression of CAVD remains elusive, aging and sex are reported to be major risk factors for the disease [3-5]. While numerous studies have been directed at discovering the mechanisms behind CAVD, very few have focused on the connection between CAVD and these two major risk factors. It is the aim of the work in this thesis to provide new insight into the connection between these risk factors and CAVD. Due to limitations in available models discussed previously, the majority of work in this thesis utilized human specimens. Advanced imaging techniques such as second harmonic generation microscopy have been utilized on human samples throughout the work discussed in the previous chapters to investigate disease and age-related changes the microarchitecture of the valve. These investigations were then utilized as the basis for development of new *in vitro* models of the microarchitecture of collagen, a major component of the valve ECM. Other work discussed previously relied on available *in vitro* models to investigate sex-related differences in valvular interstitial cells (VICs), major cell type involved in CAVD. Together, these studies work to uncover connections between CAVD and its major risk factors though methods novel in the field of CAVD investigations.

8.1.1 Characterization of Changes in Collagen with Disease and Age

While SHG has been utilized to investigate the pathology of a collection of conditions [6-9], it has not been used for investigations of CAVD prior to those conducted in previous chapters [10]. Application of this technique resulted in the characterization of changes in fibrillar collagen microarchitecture with CAVD and healthy valve aging. Changes in the collagen architecture in the valve were classified for two major layers of the aortic valve that undergo the majority of remodeling in CAVD; the spongiosa and fibrosa. Analysis using SHG revealed layer-specific changes in the structure of collagen with disease development including an increase in collagen fiber number, width, and density in the spongiosa. While ECM disarray has been reported previously as a hallmark for CAVD, this is the first time collagen changes associated with CAVD have been reported at the fiber level. In addition to investigations of diseased valves, the collagen fiber characteristic of healthy valves from humans over a larger age range were investigated for the first time. An increase in fiber alignment and decrease in fiber width were observed with increased age of human valve specimens. These observations led to inquiries into the role of post-translational modifiers of collagen including lysyl oxidase (LOX) and lysyl hydroxylase (PLOD1) in the diseased and aging valve and advanced glycation end products (AGEs) in the aging valve.

While changes in collagen content and crosslinking have been previously studied in the valve, the expression of post-translational modifiers of collagen have not been extensively explored. As discussed in Chapter 3, LOX was shown to increase in the fibrosa during disease, denoting a potential mechanism for changes in collagen fiber

width and architecture and therefore a potential target for therapeutic agents. AGEs, which increase during aging of other vascular tissues [11], were evaluated in the aging valve for the first time in Chapter 5. These studies revealed a decrease of AGEs with aging of the valve in healthy tissues, implying differences in the aging of healthy valves as compared to other tissues and providing a basis for *in vitro* investigations of how aging of the valve may influence CAVD progression.

8.1.2 Characterization of Changes in Collagen Architecture Due to Methods of Tissue Preservation

While human tissues are necessary for investigations into the progression of human diseases, they are often difficult to obtain and required long term storage when acquired [12]. However, methods for preserving tissues vary depending on intended use and discrepancies in techniques applied by different research groups. This can lead to differences in the efficiency of preservation of specific components of tissues, from quality of RNA to tissue morphology. As a number of the studies discussed throughout this thesis required SHG imaging of preserved tissue specimens, we evaluated ability of three common preservation methods, RNAlater™, flash freezing, and fixation in formalin, to preserved collagen architecture. To our knowledge, this is the first comparative evaluation of the ability of these three preservation techniques to conserve collagen fiber morphology. While tissues preserved using each method were able to generate SHG signals, preservation-based differences in collagen architecture including differences in fiber alignment in collagen sparse tissues were observed. This finding supports the construction of a regulated system for preservation of tissues and accurate

reporting of tissue preservation methods used by researchers to allow comparisons across studies performed by different laboratories.

8.1.3 Evaluation of Sex Differences in Quiescent VICs

Despite the sex-biased risk profile for CAVD, few *in vitro* studies have attempted to characterize sex differences in cultured VICs [4]. The studies presented in this thesis (Chapter 6) aimed to address this lapse in current knowledge of VIC culturing systems by evaluating sex-related differences in the response of qVICs to transforming growth factor beta (TGF-β1). As discussed in Chapter 6, TGF-β has been shown to increase markers indicative of a myofibroblast-like, activated VIC phenotype (aVICs) [13]. Our studies revealed sex-related differences in the expression of several indicators of VIC activation including an increase in deposition of ECM proteins, increased proliferation, and increased phosphorylation of SMAD2/3. Findings from this study suggest that male qVICs are more sensitive to TGF-β1 compared to females, resulting in males expressing increased markers of an aVIC phenotype. This is the first investigation of sex-differences in cultured quiescent VICs and our findings support sex-separation of VICs in future CAVD investigations.

8.1.4 Development of In Vitro Models that Mimic In Vivo *Valve Collagen Structures*

As mentioned earlier, while current *in vitro* models have provided meaningful insights into the behavior of VICs and their role in CAVD, no currently available models are able to mimic the complex collagen architecture found in the diseased and healthy human

aortic valve reported in this thesis. Also, current models of VICs have not been characterized more than a handful of passages after isolation from valves. Work presented in Chapter 7 attempted to address these current limitations of *in vitro* models through further analysis of VIC culturing systems and generation of methacrylated gelatin (GelMA) based scaffolds. Our findings show that extended passaging of aVICs express increased levels of LOX and PLOD1, where were both investigated in Chapter 3 and 5 for their role in collagen modification. Extended passaging of qVICs also revealed the ability of this *in vitro* cell model to maintain a quiescent phenotype longer than previously shown.

Studies conducted in Chapter 7 aimed to create hydrogel systems that allowed for modification of glycation content and scaffold structure to mimic the differences in valve collage reported in Chapter 3 and 5. Glycation of GelMA using D-glucose was investigated for the first time in this chapter, suggesting a new model for investigating the role of glycated ECM proteins in the valve as well as other tissues. Creation of 3D structures that mimicked the collagen architecture of human valves characterized in Chapter 3 and 5 were also reported, providing a new *in vitro* model for future investigations into collagen architecture-driven changes in VICs during aging and disease.

8.2 Recommendations for Future Work

8.2.1 Further Evaluation of Human Specimens with Advanced Imaging Modalities

As detailed previously, advanced imaging techniques have provided new insights into CAVD and age-related changes to the architecture of collagen in the valve. However,

other components of the aortic valve are shown to change in content and distribution during CAVD and age [14-16]. Elastin, a major component of the ventricularis layer of the valve, has be largely overlooked during investigations of CAVD progression despite its role in the mechanics of a healthy valve. It is possible that changes in the structure and content of elastin varies during both CAVD and valve aging. While previous investigations into elastin have been limited to histochemical techniques, currently available imaging techniques such as two-photon excited fluorescence (TPEF) allows for 3D imaging of elastin without exogenous staining by exploiting elastin autofluorescence [17]. This technique has the potential to expand the current understanding of the role of elastin in the valve.

8.2.2 Continue Investigations into Aging of the Aortic Valve

It is only in the recent years that investigations into the aging of healthy human valve has begun [15, 16]. However, even recent studies do not include valve specimens that encompass tissues from humans in the age range when the risk for development of CAVD occurs. While the studies discussed in Chapter 5 provide insight into aging of the human valve during this critical age range, much is still unknown about how the valve ages. The findings presented in this thesis also do not support the results of previous studies investigation aging in porcine model. This suggesting that current animal models may not be the ideal model of investigations into the connection between human valve aging and CAVD.

8.2.3 Reevaluate Valve Studies Based on Sex

As work presented in this thesis revealed sex-related differences at the cellular level in cultured qVICs in their response to TGF-β1, further investigations are necessary to define the extent of sex-differences in VICs. While sex is a major risk factor for CAVD, few studies into the pathology of CAVD have either directly investigated sex-based differences or reported the sex of the models used until very recently [18]. Therefore, reevaluation of the findings from previous studies incorporating the influence of sex could help identify the mechanisms behind the sex-biased presentation of CAVD.

8.2.4 Apply In Vitro *Methods to Investigate the Role of Risk Factors in CAVD*

New *in vitro* models of the valve were presented in Chapter 7 of this thesis. These models were developed to address the limitations of current models to reproduce the molecular and architectural characteristics of the human valve. As 3-D fabricated structures were able to mimic the architectural differences in healthy and diseased valves, incorporation of these structures with current VIC models would generate data on the impact of age–based or CAVD-driven changes in valve architecture on VIC phenotype.

While glycation of GelMA was investigated as a potential model for matching the glycation level observed the human valves with in vitro models, further validations are necessary prior to incorporation of this model. Glycation level should be verified through multiple means, such as ELISA, autofluorescence, and mass spectroscopy. Levels of glycation of collagen in human valve specimens should also be quantified to total collagen level for accurate representation in the developed *in vitro* model. Mechanics of

the hydrogels should also be further tuned to generate an untreated GelMA hydrogel with the same mechanical properties as the glycated model to ensure any differences exhibit by cells are due to differences in glycation and not differences in mechanical stimuli.

8.3 References

1. Go, A.S., et al., *Executive summary: Heart disease and stroke statistics-2013 update: A Report from the American Heart Association.* Circulation, 2013. **127**: p. 143-152.
2. Chen, J.-H. and C.a. Simmons, *Cell-matrix interactions in the pathobiology of calcific aortic valve disease: critical roles for matricellular, matricrine, and matrix mechanics cues.* Circulation research, 2011. **108**: p. 1510-24.
3. Rajamannan, N.M., et al., *Calcific aortic valve disease: not simply a degenerative process: A review and agenda for research from the National Heart and Lung and Blood Institute Aortic Stenosis Working Group. Executive summary: Calcific aortic valve disease-2011 update.* Circulation, 2011. **124**: p. 1783-91.
4. McCoy, C.M., D.Q. Nicholas, and K.S. Masters, *Sex-related differences in gene expression by porcine aortic valvular interstitial cells.* PLoS ONE, 2012. **7**.
5. Stewart, B.F., et al., *Clinical Factors Associated With Calcific Aortic Valve Disease.* 1997. **29**: p. 630-634.
6. Mostaço-Guidolin, L., N.L. Rosin, and T.L. Hackett, *Imaging collagen in scar tissue: Developments in second harmonic generation microscopy for biomedical applications.* International Journal of Molecular Sciences, 2017. **18**.
7. Peng, Q., et al., *Improving liver fibrosis diagnosis based on forward and backward second harmonic generation signals.* Applied Physics Letters, 2015. **106**: p. 083701.
8. Brown, E., et al., *Dynamic imaging of collagen and its modulation in tumors in vivo using second-harmonic generation.* Nature medicine, 2003. **9**: p. 796-800.
9. Drifka, C.R., et al., *Comparison of Picrosirius Red Staining With Second Harmonic Generation Imaging for the Quantification of Clinically Relevant Collagen Fiber Features in Histopathology Samples.* Journal of Histochemistry & Cytochemistry, 2016. **64**.
10. Hutson, H.N., et al., *Calcific Aortic Valve Disease Is Associated with Layer-Specific Alterations in Collagen Architecture.* Plos One, 2016. **11**: p. e0163858.
11. Brownlee, M., *Advanced protein glycosylation in diabetes and aging.* Annual review of medicine, 1995. **46**: p. 223-34.
12. Staff, S., et al., *Preservation of nucleic acids and tissue morphology in paraffin-embedded clinical samples: comparison of five molecular fixatives.* Journal of clinical pathology, 2013. **66**: p. 807-10.

13. Walker, G.a., et al., *Valvular myofibroblast activation by transforming growth factor-β: Implications for pathological extracellular matrix remodeling in heart valve disease.* Circulation Research, 2004. **95**: p. 253-260.
14. Fondard, O., et al., *Extracellular matrix remodelling in human aortic valve disease: the role of matrix metalloproteinases and their tissue inhibitors.* European heart journal, 2005. **26**: p. 1333-41.
15. Oomen, P.J.A., et al., *Age-dependent changes of stress and strain in the human heart valve and their relation with collagen remodeling.* Acta Biomaterialia, 2016. **29**: p. 161-169.
16. Van Geemen, D., et al., *Age-dependent changes in geometry, tissue composition and mechanical properties of fetal to adult cryopreserved human heart valves.* PLoS ONE, 2016. **11**.
17. Tilbury, K., et al., *Second harmonic generation microscopy analysis of extracellular matrix changes in human idiopathic pulmonary fibrosis.* Journal of biomedical optics, 2014. **19**: p. 086014.
18. Simard, L., et al., *Sex-Related Discordance Between Aortic Valve Calcification and Hemodynamic Severity of Aortic Stenosis Is Valvular Fibrosis the Explanation ?* 2016.